FIRST STREET FOUNDATION

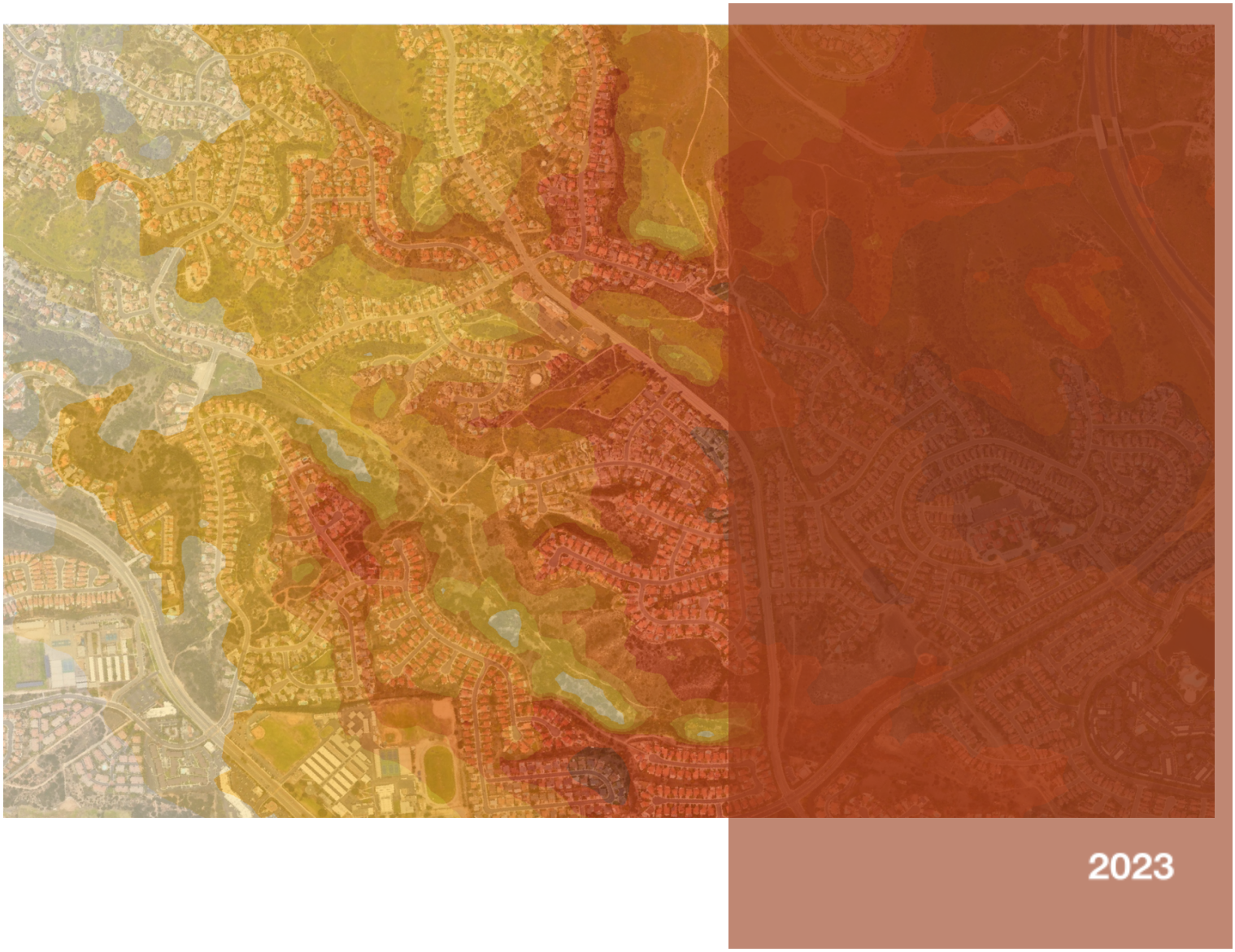

2023

First Street Foundation Wildfire Model

Technical Methodology

FIRST STREET FOUNDATION

First Street Foundation Wildfire Model (FSF-WFM) Technical Documentation

Latest Model Version: FSF-WFM Version 3.0

Published: 7/31/2023

FIRST STREET FOUNDATION

Table of Contents

FIRST STREET FOUNDATION

Terminology

BPS - Biophysical Settings
CBD - Canopy Bulk Density
CBH - Canopy Base Height
CC - Canopy Cover
CCSM4 - Community Climate System Model
CDF - Cumulative distribution function
CH - Canopy Height
CMIP5 - Coupled Model Intercomparison Project version 5
CMIP6 - Coupled Model Intercomparison Project version 6
CONUS - Contiguous United States
ECDF - Empirical CDF
ELMFIRE - Eulerian Level set Model for FIRE spread
ERC - Energy Release Component
FM40 - Scott and Burgan 40 Surface Fuels
FVC - Fuel Vegetation Cover
FVH - Fuel Vegetation Height
FVT - Fuel Vegetation Type
ICDF - Inverse cumulative distribution function
LFTFCT - LANDFIRE Total Fuel Change Tool
NFDRS - National Fire Danger Rating System
NCL - National Center for Atmospheric Research Command Language
PDF - Probability density function
PRISM - Parameter-elevation Regressions on Independent Slopes Model
RCP - Representative Concentration Pathway
RD - Rain Days
RH - Relative Humidity
RI - Recurrence Interval
RTMA - Real Time Mesoscale Analysis
SF - Scaling Factor
SSP - Shared Socioeconomic Pathway
WCRP - World Climate Research Programme
WUI - Wildland Urban Interface

FIRST STREET FOUNDATION

Executive Summary

The need for an understanding of the wildfire risk across the United States has been described by a number of stakeholders and researchers (Burke et al., 2021; Westerling et al., 2006; Vose et al., 2018). To address the need to accurately describe this risk at the community level and therefore allow for the formulation of appropriate disaster responses, the U.S. Federal Government supported the creation of the publicly-available Wildfire Risk to Communities (see WildfireRisk.org; Scott et al., 2020) which was published in April, 2020. Wildfire Risk to Communities conveys relative fire risk for communities following analysis at a 270m horizontal resolution and based on the US Forest Service's 2014 Landscape Fire and Resource Management Planning Tools (LANDFIRE, 2020) database which provides open data on the composition and state of fuels across the United States. Given the rapid increase in observed US wildfire occurrence (Smith, 2022), the resultant losses of $8.5 billion from 2012-2016 and $79.8 billion from 2018-2021 (NOAA, 2022), and the impacts of climate change on wildfires (Abatzgalou and Williams, 2016), there is a need to evaluate the probable changes in wildfire exposure in order to provide US residents a more informed understanding of their current and future risk.

Following the open science approach taken by the nonprofit First Street Foundation for climate-adjusted flood risk (Armal et al. 2020; Bates et al. 2021; Kearns et al. 2020), a new analysis was undertaken to estimate the annual wildfire exposure at a property-by-property scale across the United States. The technical documentation for the methodology used by the First Street Foundation Wildfire Model (hereafter, FSF-WFM) to compute estimates of the 30-year, climate-adjusted aggregate wildfire hazard for the contiguous United States at 30 meter horizontal resolution is presented.

The FSF-WFM integrates several existing methods from the wildfire science community and implements computationally efficient and scalable modeling techniques to allow for new high-resolution, hazard generation across the contiguous United States (CONUS). Using U.S. Federal Government open data as a foundation, additional data were added from a variety of sources which facilitate both a high resolution (30m horizontal) and future-facing (for today and for 30 years ahead) product allowing individuals, communities, businesses, and governments to better understand and prepare for their wildfire risk. Burn probability, flame length, and ember spread for the current years and 30 years into the future are computed from Monte Carlo simulations of wildfire behavior, utilizing augmented LANDFIRE fuels estimates updated with best-available ancillary disturbance information. FSF-WFM utilizes ELMFIRE, an open-source, Rothermel-based wildfire behavior model (Lautenburger, 2013), and multiple US Federal Government open data sources to drive the simulations. The LANDFIRE non-burnable fuels classes within the Wildland Urban Interface (WUI) are replaced with fuel estimates from machine-learning models trained on data from selected historical fires to allow the propagation of wildfire through the WUI in the model. Historical wildfire ignition locations and NOAA's hourly time series of surface weather at 2.5km resolution are used to drive ELMFIRE to produce wildfire hazards representative of the current and

+30 year conditions at 30m horizontal resolution, with the future weather conditions scaled to the WCRP's CMIP6 SSP245 climate model ensemble projections (Eyring et al, 2016). As simplifying assumptions, both winds and vegetation were kept unchanged between the current and future simulations, and thus climate change's impact on the future fuel conditions is the main contributor to the changes observed in the +30 year results. Calibration of the present-year Monte Carlo simulation results utilizes a statistical match on a CONUS pyrome-by-pyrome (Short et al, 2020) basis against historical fire perimeters and sizes, and an adjustment of fire spread rates and burn lengths accounting for geographically variable suppression. Validation against historical fire ignition locations and sizes applies a spatial smoothing to reduce the consequence of clusters of small historical fires.

The compound wildfire risk product resulting from this model has been named "Fire Factor" as part of a wider "Risk Factor" information platform provided by the First Street Foundation for free, public use under noncommercial license terms (see riskfactor.com). The latest Fire Factor results show that non-zero wildfire exposure is estimated for 72.7 million out of 143.9 million properties across CONUS. Climate change impacts add another 15% properties to this non-zero exposure class over the next 30 years. Much of this change in wildfire exposure is observed in forested areas east of the Mississippi River. "Major" aggregate wildfire exposure of greater than 6% over the 30 year analysis period from 2023-2053 is estimated for 15.4 million properties. The FSF-WFM represents a notable contribution to the ability to produce property-specific, climate-adjusted wildfire risk assessments in the US.

FIRST STREET FOUNDATION

Methodology

The methodology for estimating the wildfire hazard exposure today and 30 years into the future, and assigning 30-year aggregate scores for properties and buildings in the U.S. follows an open science approach (Gentemann et al., 2021), allowing for a complete understanding and enabling independent validation and verification of the results. The usefulness of the information products are enhanced through the independence from any proprietary methods and through heavy dependence on open data from government and public record sources.

The method involves the following steps:

- Estimate the fuels that support wildfires across the US at 30m horizontal resolution by updating the v2.0 LANDFIRE dataset (2014) with disturbances over the 2011-current year period. and the conversion of fuels within the WUI from non-burnable to burnable classes.
- Assemble a weather data time series that can be used to drive a fire behavior model under a wide representative range of different weather conditions, and approximated in the future as influenced by a changing climate.
- Use the likely ignition locations for current and future wildfire simulations, based on historical ignition data, and include a random element to capture possible ignitions in areas impacted by climate change. Ignitions are precluded from within the WUI, assuming active suppression in those areas.
- Apply a fire incidence and behavior model across the landscape of the contiguous United States in a Monte Carlo simulation to build probabilistic estimates of wildfire hazards in terms of burn probability, fire intensity (mean and maximum flame length), and spread of embers. Geographically-variable fire suppression effects are incorporated into the model.
- Calibrate the burn probabilities for each pyrome by comparing the simulated number of fires and their sizes to the historical record.
- Assign a wildfire exposure score (1-10) for each property in the U.S. based on the parcel's burn probability and its exposure to ember cast. Also estimate the average annual loss for buildings on each property using a combination of a specific vulnerability assessment for each building and damage functions that were developed by the international engineering firm Arup.
- Distribute the resulting climate-adjusted, property-resolution data freely to the public for noncommercial use, deliver in bulk to public agencies for societal benefit, and create reports on the national, state, and local levels that summarize the results and raises awareness of the current and future risk of wildfire.

FIRST STREET FOUNDATION

2.0 Documentation and Versioning

This document will be maintained to reflect the latest version of the FSF-WFM and the Fire Factor outputs. The FSF-WFM will be run annually with updates to fuels and disturbances for the current year, and if any input data are changed or methodological improvements have been made, those changes will be reflected in this document.

2.1 Data Sources

The wildfire risk product is based on a number of data sources (Table 1. Data Sources), including a number of U.S. Federal government open datasets that are provided to encourage research efforts in the field. These data have been augmented by other data collected from state, local, and commercial sources that bring the collection up to date (to May 2021).

Table 1. Data Sources

Name	Subject	Source	Dates or Version	Notes
LANDFIRE	Fuels	LandFire.gov	V2.0.0; Aug 11, 2021	Open
LandSat-8	Fuels	https://developers.google.com/earth-engine/datasets/catalog/landsat-8	9/1/2021 – 11/1/2021	Open
USGS NED	Topography			Open
USDA Forest Service's Fire Occurrence Database (FOD)	Ignition Locations	https://doi.org/10.2737/RDS-2013-0009.6	6th Edition;	Open
MTBS, NIFC	Historical fires			Open
NOAA RTMA	2.5km Surface Weather, 2011-2020	https://mtarchive.geol.iastate.edu/ and https://www.ncei.noaa.gov/has/HAS.FileApp	December 31, 2021	Missing hourly precipitation values were replaced with hourly estimates derived

Name	Subject	Source	Dates or Version	Notes
		Router?datasetname=9950_01&subqueryby=STATION&applname=&outdest=FILE		from daily precipitation totals from PRISM
NASA NEX-GDDP	Climate	NASA NEX-GDDP Portal for CMIP6		Creative Commons 0 (CC0) license; CMIP6 SSP245
Future Weather	Weather estimates for +30 year simulation. Derived from NASA NEX-GDDP and NOAA RTMA time series			Wind Held Constant. Air temp, relative humidity, and precipitation are scaled using NASA NEX-GDDP.
Future Fuels	Fuels for +30 years fire simulation	Assumed to be same as current year (static)	NA	Fuels held constant between current year and +30y - assumes no net growth of forests over 30 years
Property Boundaries and characteristics	Descriptive information about properties	Lightbox	2023	Aggregated from public records; Commercial but available
Building footprints	Building locations on properties	MapBox	2023	Aggregated from satellite imagery and public records; Commercial but available
Building Density	Derived from Building footprint information	FSF		Used for Urban, WUI and Wildlands designations

2.2 Fuels

The wildfire hazard estimate is most heavily dependent upon estimates of the type, quantity, age, and condition of the combustible fuels across the US. We use version 2.0.0 (2016 vintage) of the canonical U.S. Forest Service (USFS) LANDFIRE fuels dataset (LANDFIRE, 2020) at 30m horizontal resolution, which we have then updated through the inclusion of disturbances from 2016 to December 2020 using the processes described below.

2.2.1 Disturbance

Our objective was to produce a comprehensive CONUS-wide disturbance raster layer comprising fuels treatments and wildfire disturbances current through December 2020, which were then used to update the 2016 LANDFIRE v2.0.0 surface and canopy fuels. The disturbance layer is designed to be congruent with the LANDFIRE disturbance code schema, which consists of thematic three-digit code values corresponding to disturbance type, severity, and time since disturbance, respectively (see a complete description at https://landfire.gov/DataDictionary/Fuel_Ruleset_Database_Data_Dictionary_2019.pdf).

All known treatments and harvests were compiled for national, state, and regional levels as well as wildfire burn severity data from the Monitoring Trends in Burn Severity (MTBS) database (1984-2019 at time of analysis) and the National Interagency Fire Committee (NIFC; 2020 only). For FSF-WFM, we used all nationally-available datasets. Not all statewide datasets are included, but western states with the highest fire risk (e.g. California, Oregon, Arizona, Washington, Idaho, Colorado and New Mexico) were prioritized to ensure their inclusion. The datasets included in the disturbance raster are listed in Table 2, Treatment Disturbance Inputs.

Table 2. Treatment Disturbance Inputs accessed in October 2022

Dataset Name	Source Data Link
Hazardous Fuels Treatments - Fire - USFS	https://apps.fs.usda.gov/arcx/rest/services/EDW/EDW_HazardousFuelsTreatments_01/MapServer/3
Hazardous Fuels Treatments - Other - USFS	https://apps.fs.usda.gov/arcx/rest/services/EDW/EDW_HazardousFuelsTreatments_01/MapServer/4
Hazardous Fuels Treatments - Mechanical - USFS	https://apps.fs.usda.gov/arcx/rest/services/EDW/EDW_HazardousFuelsTreatments_01/MapServer/5
Hazardous Fuels Treatments - All Other Values - USFS	https://apps.fs.usda.gov/arcx/rest/services/EDW/EDW_HazardousFuelsTreatments_01/MapServer/7

Timber Harvest - USFS	https://apps.fs.usda.gov/arcx/rest/services/EDW/EDW_TimberHarvest_01/MapServer/8
CALMAPPER Treatment Projects	https://egis.fire.ca.gov/arcgis/rest/services/CalMapper/CalMAPPER_Public/FeatureServer/2
CALFIRE Priority Treatment Projects	https://services1.arcgis.com/jUJYIo9tSA7EHvfZ/ArcGIS/rest/services/PriorityProjects2019/FeatureServer/0
CALFIRE Timber Harvest	https://services1.arcgis.com/jUJYIo9tSA7EHvfZ/ArcGIS/rest/services/CAL_FIRE_Timber_Harvesting_Plans_All_WGS84/FeatureServer/0
CALFIRE Fire Perimeters - Prescribed Fire	https://egis.fire.ca.gov/arcgis/rest/services/FRAP/FirePerimeters_FS/FeatureServer/1
CALFIRE Forest Health CCI Awarded Projects 2017-18	https://services1.arcgis.com/jUJYIo9tSA7EHvfZ/ArcGIS/rest/services/Forest_Health_CCI_Awards_2017_2018/FeatureServer/0
Treatment areas - National Park Service	https://mapservices.nps.gov/arcgis/rest/services/WildlandFire/WildlandFire/FeatureServer/5
Treatment areas - ID - BLM	https://navigator.blm.gov/api/share/e5fb96b234d32c5a
Treatment areas & Harvest - OR Dept Forestry	https://gisapps.odf.oregon.gov/data/FernsNoapsPolygons.Zip
Treatment areas - CA - BLM	https://navigator.blm.gov/api/share/a446b6874c2a37fc
Treatment areas - NM - BLM	https://gis.blm.gov/nmarcgis/rest/services/Range/BLM_NM_Vegetation_Treatments/MapServer/0
Harvest - WA Dept Natural Resources	https://gis.dnr.wa.gov/site2/rest/services/Public_Forest_Practices/WADNR_PUBLIC_FP_FPA/MapServer/6/

Disturbances from wildfires across CONUS were incorporated by using the MTBS burn severity dataset, augmented with perimeter data from NIFC if the MTBS dataset was not yet available. To ensure that fire severity was consistent between the MTBS and NIFC datasets, a custom burn severity tool was built in Google Earth Engine (EE) to calculate burn severity within fire perimeters. The tool creates one pre-fire and post-fire image composite for each fire perimeter provided after filtering the satellite image catalog with a predefined time window and masking out clouds. After computing the the Relative Difference Normalized Burn Ratio (RdNBR) index from pre-fire and post-fire image composites, the Miller's threshold (Miller and Thode, 2007) is applied to the RdNBR image creating a burn severity classification matching the MTBS classification that ranges from 0-6, though for practical reasons we employ the range from 1-5 in this study. We used a time window of 90 days after the fire discovery date, using the previous calendar year and the actual

year for the pre-fire and post-fire image composites respectively. We applied a size threshold of >500 acres to the NIFC perimeter data to maintain consistency with the minimum fire size of the fires included in the MTBS dataset. Then all 2020 NIFC fire perimeters greater than 500 acres were run through the burn severity calculator and the resulting CONUS-wide burn severity raster was reclassified to the five-class severity classification scheme used for MTBS burn severity.

For fuel treatments (including harvest, fuel mitigation treatments, and prescribed fire), there are no uniform naming conventions for forest management practices across the U.S. and the quality of data entry varies considerably among the full collection of datasets. Therefore, to ensure that every feature in our full data catalog is assigned a standardized disturbance class, we compiled all unique treatment names given in the attributes of every treatment dataset into a document that was reviewed by forestry field experts to ensure that each treatment type was appropriately characterized. Each unique name in the document was assigned a LANDFIRE disturbance type, resulting in a lookup table of unique treatment descriptions and their LANDFIRE disturbance type equivalents.

The resulting treatment and wildfire disturbance rasters were then assigned the appropriate three digit LANDFIRE disturbance code. The three-digit disturbance code includes one digit each for disturbance type, severity, and time since disturbance. The disturbance types most frequently found in our dataset were fire (Disturbance Type 1), Mechanical Add (Disturbance Type 2, when fuels are mechanically mowed or chipped and transitioned to surface fuels), and Mechanical Remove (Disturbance Type 3, when fuels are removed via cutting, felling, burning, or harvest). We assigned a disturbance type “other” (Disturbance Type 8) to chemical treatments and grazing. We excluded treatments or activities included in the datasets that would not have impacted fuels (including but not limited to seeding, habitat restoration, and invasive species removal).

Table 3. Occurrence of Disturbance Types

Disturbance Type	Disturbance Type (%)
Fire	92.8%
Mechanical add	0.2%
Mechanical reduce	5.8%
Other	1.2%

Table 4. Disturbance Type Codes

Disturbance type description	Disturbance type code
Fire	1

Mechanical + (add) loading (no fuel removed from site)	2
Mechanical - (removal) loading (fuel removed from site)	3
Windthrow	4
Insects-Disease	5
Other	8
Disturbance pre-2011	77
No disturbance (eg. restoration, invasive spp removal, etc)	88
NA (eg. wildfire, unknown)	99

Regarding severity, treatment disturbances such as hand thinning, piling, prescribed fire, and other treatments where canopy cover is not altered are assigned a disturbance value of 1 (low severity). Treatments such as mechanical thinning and harvest are assigned a disturbance value of 2 (medium severity). Clear cuts were assigned a disturbance value of 3 (high severity). For the wildfire disturbances, we followed the MTBS conventions where fire severity class 2 was low severity, 3 was medium severity, and 4 was high severity. Classes 1 (unburned/unchanged) and 5 (increased greenness) were considered undisturbed.

Table 5. Occurrence of Disturbance Severities

Disturbance Type	Disturbance Severity (%)
Low	**65.0%**
Medium	20.2%
High	14.8%

Table 6. Disturbance Severity Codes

Severity type description	Severity type code
Low	1
Medium	2
High	3

The time since disturbance code was determined based on the year of treatment and the LANDFIRE zone. Time since disturbance was categorized as 1 (<1 year; e.g. for an effective year of 2021, disturbances that occurred in 2020), 2 (1-5 years; e.g. for an effective year of 2021, disturbances that occurred in 2015-2019), and 3 (6-10 years; e.g. for an effective year of 2021, disturbances that occurred in 2011-2014). For disturbances that occurred in the LANDFIRE Southeast Super Zone (Zones 46, 55, 56, 58, and 99) the time since disturbance categories are 1 (<1 year; for an effective year of 2021, disturbances that occurred in 2020), 2 (1-3 years; for an effective year of 2021, disturbances that occurred in 2017-2019), and 3 (4-10 years; for an effective year of 2021, disturbances that occurred in 2011-2016).

The treatment and wildfire layers were mosaicked together into a single disturbance layer using a priority ranking ruleset informed by LANDFIRE analysts (T Smail, 2021, personal communication) to ensure the most fuels-relevant disturbance value is assigned in cases of spatial overlap of multiple disturbances. As with the LANDFIRE Total Fuels Change Tool (LFTFCT) methodology, we do not account for potential compounding effects that multiple disturbances may have on fuels within the update time-period. However, in most cases the most severe disturbance is presumed to take precedence in the fuel changes that drive fire behavior outcomes.

Fuel treatments reported at all scales of forest management are often not fully treated in the delineated areas submitted to the public databases. This can lead to unrealistic updates to fuels by fire analysts and in turn inaccurate fire behavior in resulting products. While the most accurate validation approach is undoubtedly ground-based with local experts, at CONUS scale this is most practically accomplished with remote sensing. The Hansen Global Forest Change dataset provides a ‘loss year’ band representing the year(s) when there was detectable canopy loss during the period 2000 - 2020 at 30m/pixel scale. We leveraged this band to create a forest loss 2011-2020 image mask and applied it to our final disturbance layer to remove false positives of moderate and high severity harvest (Hansen et al., 2013).

2.2.2 Fuels

We generated four canopy fuel layers with an effective year of present year+1 (i.e. using last year’s end fuel state for the next fire year) for use as inputs into the fire models: canopy cover (CC), canopy height (CH), canopy base height (CBH), canopy bulk density (CBD), and the Scott and Burgan 40-class surface fuel model layer surface fuel layer (FM40). We used LANDFIRE v2.0.0 (2016 vintage) as the base and only transitioned fuels in areas that were disturbed between 2011 and 2020. The process of creating updated canopy and surface fuel layers in Earth Engine begins with generating several initial layers representing lookup rulesets in the LANDFIRE Total Fuel Change Tool (LFTFCT) database. First, canopy cover and height midpoint layers are derived from

the LANDFIRE Fuel Vegetation Cover (FVC) and Fuel Vegetation Height (FVH) rasters based on the LFTFCT lookup table values. Next, using the new disturbance layer, a Canopy Guide layer is generated by using the LFTFCT master lookup table applied to unique combinations of the disturbance code, LANDFIRE Biophysical Settings (BPS), FVC, FVH, and FVC. The four canopy fuel layers are then generated pixel-wise using a regression equation:

$$Canopy\ Fuel = C_X + H_y + b \quad (1)$$

where C is the canopy cover midpoint, H is the canopy height midpoint, x and y are scale factors, and b is an intercept value derived from a lookup of unique disturbance code and Fuel Vegetation Type (FVT) value combinations from the LFTFCT lookup table. For canopy cover and canopy height regressions, the cover and height midpoint values are derived from the initial FVC and FVH midpoint layers described above, while for canopy base height and canopy bulk density, the midpoint values are derived from the canopy cover and height layers generated in the step described above. Additionally, canopy bulk density uses a ruleset to create two stand height coefficients from the canopy height midpoint value for pixels with a Pinyon Juniper FVT code, following the rules described in Reeves et al. (2009). Each canopy fuel regression output is post-processed to ensure values are within their valid value range, scaled properly, and binned, if necessary, to defined midpoint values. Finally, the Canopy Guide layer is applied to each layer using rulesets based on canopy cover thresholds.

The surface fuels portion of the fuelscape, FM40, is generated in the same way as the canopy guide, using the LFTFCT master lookup table applied to unique combinations of the disturbance code, BPS, FVC, FVH, and FVC. Products derived from this workflow include an Earth Engine library of datasets including the full archive of necessary LANDFIRE fuel and vegetation datasets for the workflow (including all available versions), the derived fire severity layer, the canopy cover and canopy height midpoint layers, and the disturbance layer. The last year's fuel profile used to estimate the next fire-year's wildfire probability includes the collection of the five fuel layers (FM40, CC, CH, CBH, CBD).

2.2.3 WUI surface fuel updates

Of particular interest to the Fire Factor information product is the ability to estimate the wildfire risk to properties, homes, and business within the Wildland Urban Interface (WUI) across the U.S. Typically, pixels that encompass homes and other buildings are classified as nonburnable fuels within LANDFIRE. The objective of the WUI surface fuel update was to convert non-burnable developed pixels to a burnable surface fuel model in order to allow fire to spread into built

environments that are known to burn under fire weather conditions. The first step of developing the WUI fuel model was to derive a current map of WUI areas as defined by USDA-USDI (Glickman & Babbitt, 2001). WUI areas are defined by two factors: building density and distance from wildland vegetation (Martinuzzi et al., 2015). We used the 2016 National Land Cover Dataset (NLCD) Existing Vegetation Cover layer to identify areas of wildland vegetation and Mapbox building footprints data (see Table 1. Data Sources). We derived a raster of the three WUI classifications using Google Earth Engine (see Figure 2. Workflow to create a new CONUS-wide WUI raster layer).

The WUI influence zone, WUI intermix, and WUI interface were defined as:

- Influence zone is >75% land coverage of wildland vegetation within 1 miles of a residence.
- Intermix is >1 residence per 40 acres and groups of residences larger than 50 acres with >50% land coverage of wildland vegetation.
- Interface is defined as >1 residence per 40 acres and groups of residences larger than 50 acres with <50% land coverage of wildland vegetation, and within 1 miles of wildland vegetation.

Figure 1. Updating LANDFIRE fuel layers in Google Earth Engine (EE).

The modifications of the LANDFIRE v2.0.0 fuels (LF) include use of Disturbance data (FVC Fuel Vegetation Cover; FVH - Fuel Vegetation Height; FVT - Fuel Vegetation Type; BPS - Biophysical Settings) to modify surface (FM40) and canopy fuel classes (Canopy Cover CC; Canopy Height CH; Canopy Base Height CGH; Canopy Bulk Density CBD), and the replacement of non-burnable fuel classes in the WUI with fuel classes that were found to approximate observed fire behavior in past WUI fires.

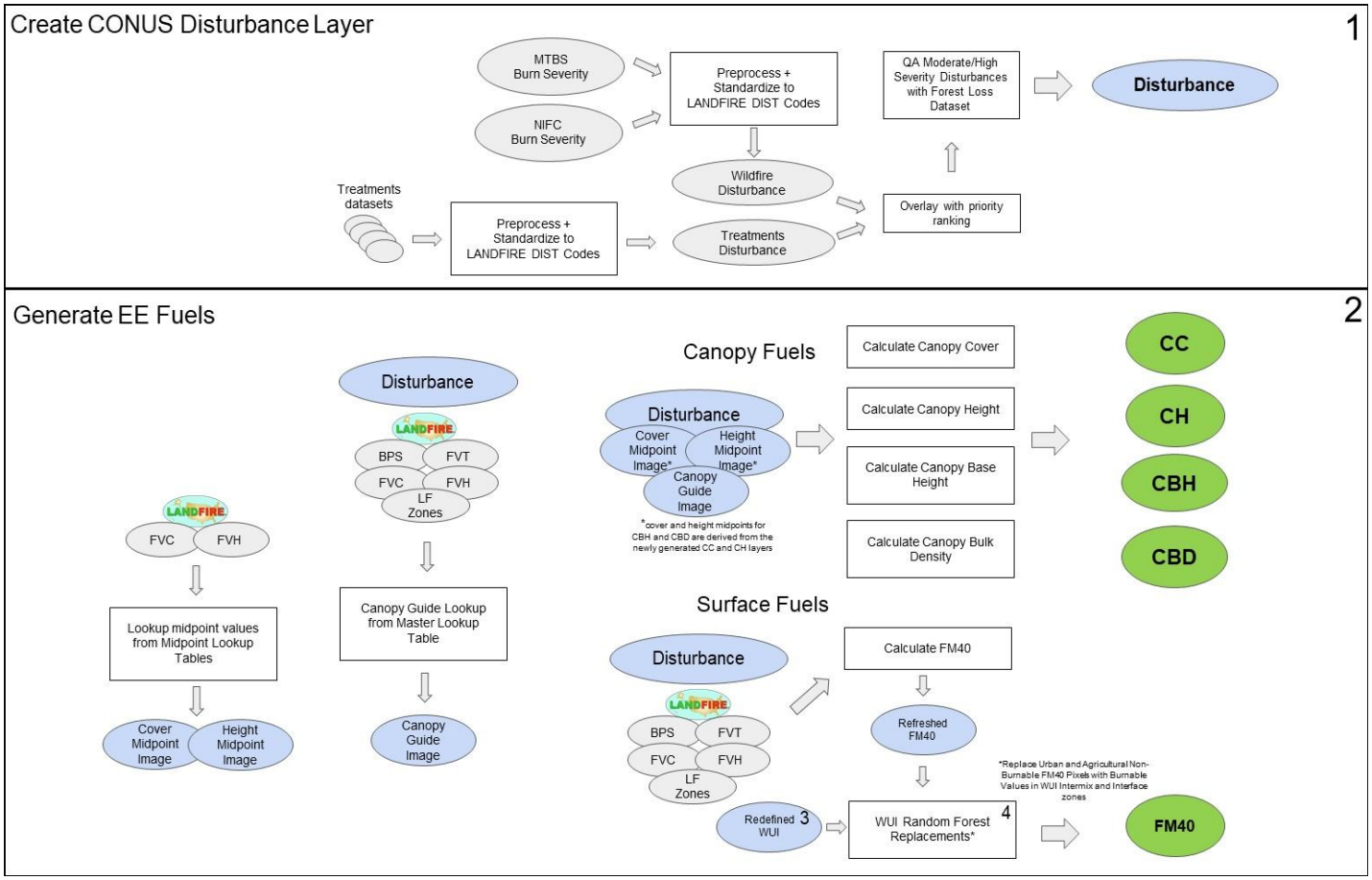

This figure represents steps 1 & 2 in the fuels methodology, Steps 3 & 4 are included in Figure 2 and 3.

Because the WUI influence zone is heavily influenced by wildland vegetation cover, much of this area is already classified with burnable FM40 values. Therefore, we were concerned that model-based FM40 conversions within the influence zone could potentially introduce more bias in the fire behavior than it would correct for the relatively small non-burnable areas in this zone. To convert non-burnable pixels in the WUI intermix and interface, we used a pixel-based random forest approach trained from 549 historical fire perimeters that burned into the WUI in CA, TX, AR, LA, TN, AL, NC, SC, GA, and FL from 2014-2019. The 549 fires used in the Random Forest met the following qualifications: they must have overlapped the WUI intermix or interface areas and they must have had verified SIT209 reports with the number of residences destroyed and associated IRWINID (https://forestsandrangelands.gov/WFIT/applications/IRWIN/index.shtml) which could be matched to MTBS.

Figure 2. Workflow to create a new CONUS-wide Wildland Urban Interface raster layer used in the WUI Random Forest update.

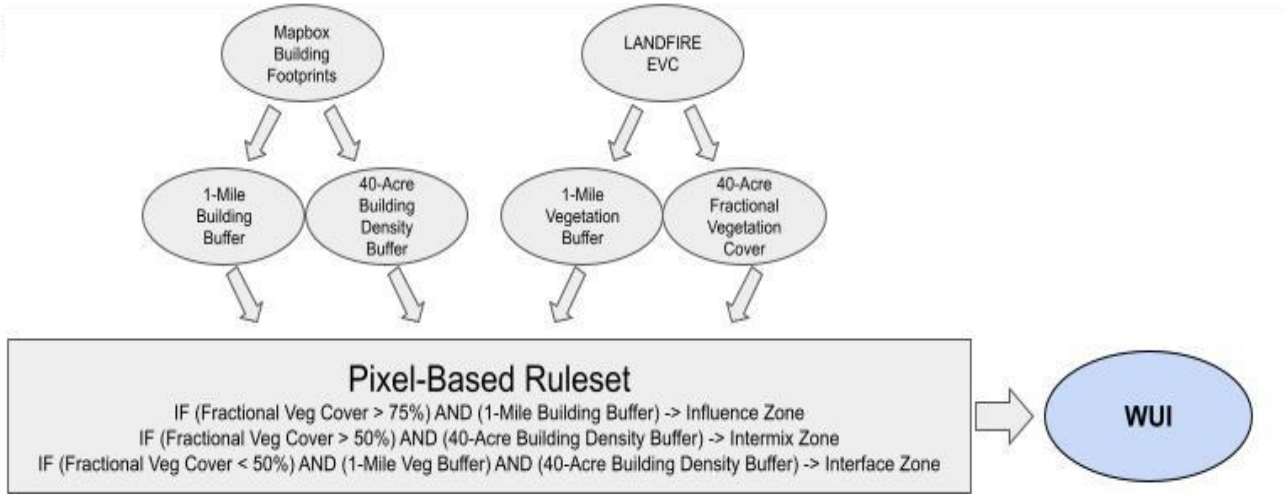

There were 2,481 fires which met that criteria from 2013-2020. The 549 fires were not a random sample but were specifically picked from the most destructive fires in the dataset and with the goal of obtaining a representative geography. All incidents which had any residences destroyed (about half of the fires) were used, and about half had no residences destroyed. The model used predictor variables that encompassed the fire's topography, vegetation, and the weather prior to and following the fire's occurrence (Figure 3. Random forest model development). We used the 2021 FM40 dataset derived in the fuels workflow described above as the response variable.

The training and testing sample areas were composed of pixels in the WUI intermix and interface that were within (or within 1km of) MTBS fire perimeters from our disturbance dataset (2011-2020), in order to capture areas that both burned and unburned elements of the fire area. For each fire, we manually matched it with the fire incidence records reported in federal interagency SIT/209 forms so that we could also derive a total buildings destroyed metric per fire (total_dest). Other predictor variables included vegetation products from LANDFIRE v2.0.0 (FVT, FVC, FVH), Landsat bands and spectral indices derived from 4-month composites encompassing each training fire's ignition date (coastal, blue, green, red, nir, ndvi (normalized difference vegetation index), swir1, swir2, mndwi (modified normalized difference water index), bai (burn area index), gridMET weather data derived from 1-month composites encompassing each training fire's fire ignition date (tmin (temperature minimum), tmax (temperature maximum), fm1000 (1000 hour fuel moisture), vs (wind velocity at 10 meters), ERC (energy release component), bi (burn index), topography variables from USGS (slope, elevation, aspect), building density per 1 km^2 (bldg_density), and MTBS fire severity (SEVERITY) (Figure 4. WUI FM40 variable importance fig). The model was trained only on burnable FM40 values. After training and validation, we constrained our model inference areas to those pixels that contained 2021 FM40 urban/developed (91) and Agricultural (93) class values and were in the WUI intermix and interface (Figure 3. Random forest model training and classification).

The independent validation dataset showed 72% accuracy upon comparison. Overall, the vegetation, topographic, and weather variables had higher importance than the fire-related or building density-related variables in the model (Figure 4. WUI FM40 random forest importance values). In general, non-burnable WUI intermix and interface pixels were frequently replaced with grass or grass-shrub fuel types (FM40 classes 101 and 121, and occasionally 103 in the Southeast and 183 in the Mid-atlantic). The predicted pixels were replaced in the FM40 fuel layer to create the final current-year FM40 with the surface fuel model updated for both disturbances and WUI areas.

Figure 3. Random forest model training and classification to replace non-burnable FM40 classes with burnable classes in the newly defined WUI.

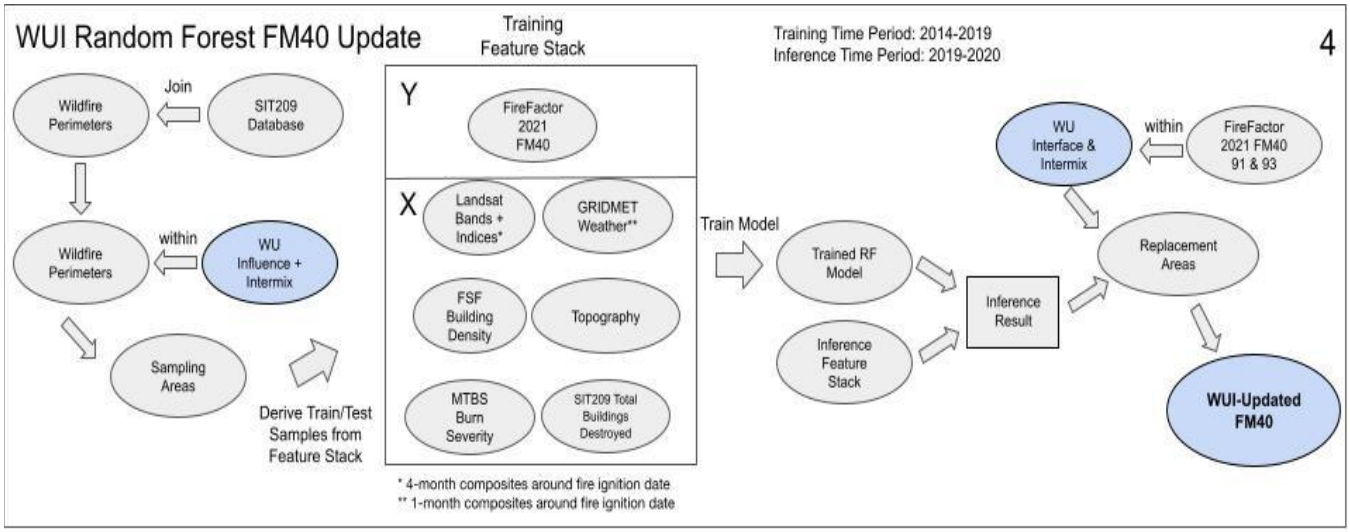

2.2.4 Irrigated lands

We updated irrigated lands (eg. municipal parks, golf courses, and irrigated agricultural areas) to be non-burnable if they were classified by a burnable fuel type. The irrigated landscape fire behavior fuel model update was completed in Google Earth Engine using LandSat-8 imagery from 9/1/2021 – 11/1/2021, the SIG WUI raster, and the SIG-updated LandFire Scott & Burgan 40 fire behavior fuel models dataset. Pixels obscured by clouds and cloud shadows were excluded from the LandSat-8 imagery and a mean composite image was created, from which NDVI and NDMI were calculated. A mask was created of the pixels where NDVI was ≥0.25 and NDMI was ≥0.10 to identify potentially irrigated pixels. This NDVI-NDMI mask was then trimmed using the SIG WUI raster to only include potentially irrigated pixels in WUI and urban areas. From the SIG-updated LandFire 40 FBFM dataset, a mask was created to include only pixels of grass and grass-shrub fire behavior fuel models which was further masked to only include areas of these fuel models ≥0.5 acres in size. The final mask was created by extracting where the masked SIG-updated LandFire 40 FBFM raster and the NDVI-NDMI-WUI raster overlapped, these areas were then updated to fire behavior fuel model “93 – Non-burnable agriculture”. In summary, areas deemed “irrigated” and updated to FBFM 93 were areas in WUI and urban areas with Fall 2021 NDVI values ≥0.25 and NDMI values ≥0.10 that were previously labeled as a grass or grass-shrub FBFM and were ≥0.5 acres in size.

2.2.5 Vegetation changes

Changes in the composition and volume of vegetation due to climate change's impacts have been discussed in papers such as (Morin et al., 2018) and their importance to estimates of wildfire probability and sensitivity to uncertainties in those estimated changes has been discussed (e.g. Syphard et al., 2018). While research continues on ways of estimating the vegetation and fuel changes anticipated across CONUS in a changing climate, we have elected to hold the fuels constant between the present year and +30y simulations for the purposes of this study. Differences in wildfire risk will then be functions of future weather and resulting fuel conditions alone, which simplifies our ability to interpret results.

Figure 4. WUI FM40 random forest importance values (variables described in text)

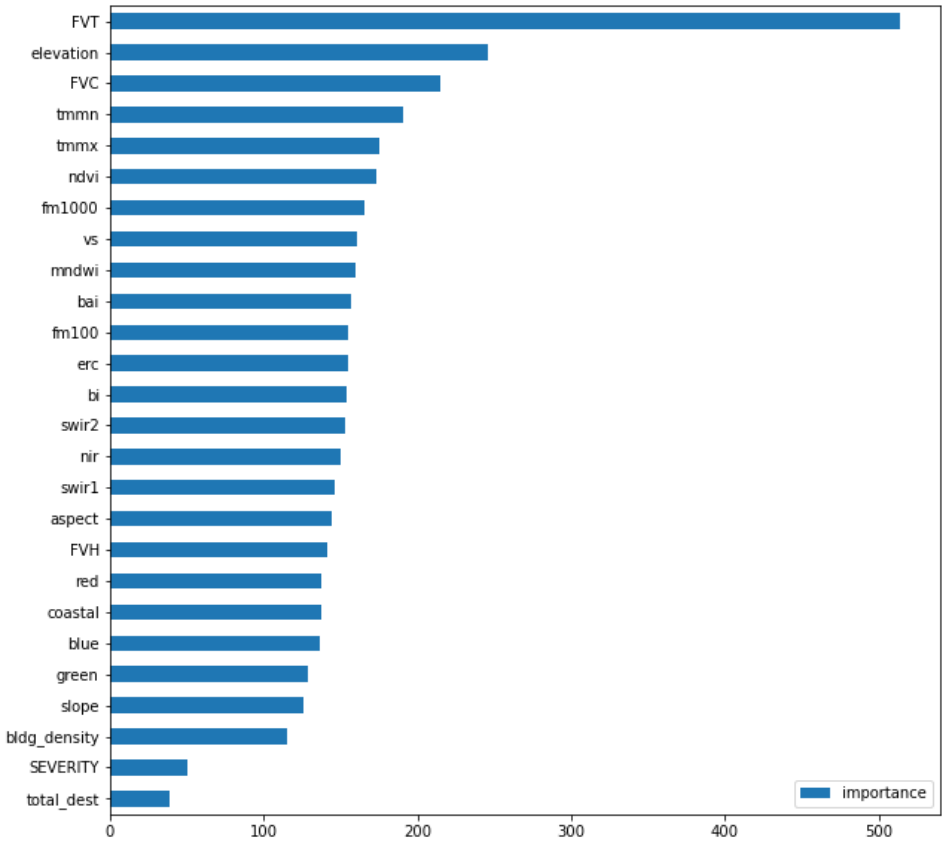

2.2.6 Assumptions and Limitations

The methods described above produce an estimate of the fuels across the US from the previous year, not including any predicted changes in the built environment. Limitations of the approach described include the dependence on the accurate reporting of disturbances. The reporting of disturbances is sometimes based on planning data instead of actual disturbances. Local governments and forest management services also have large variability in reporting structures and conventions, potentially leading to differences across political boundaries. Additionally, there is great variability concerning the reporting of disturbances on private lands; this may be a greater source of uncertainty in the eastern US than the west. Remote-sensed data may be utilized in future versions to delineate and quantify the disturbances in those areas to a higher degree of precision. Relatedly, the way that disturbances are integrated here does not account for the impact of compounding disturbances within the considered 10 year period and prioritizes those disturbances which more heavily impact fuels. Finally, all disturbances are still operating within the LANDFIRE environment, where fuel layers are meant to result in realistic fire behaviors more so than to reflect fuel conditions on the ground (e.g. fuel model versus actual fuel loads).

As noted above, the fuel types and state in +30y for CONUS ideally should be estimated to allow a 30-year, climate-adjusted aggregate risk estimate that comprises the Fire Factor information product. However, we have chosen to omit the contribution of net forest growth and possible changes of composition from V1 of our wildfire risk estimates. Therefore, the fuel type and composition are held static from present year to +30y and will focus entirely on the impact of climate change on the fuels condition.

Another assumption related to the ignition locations is that any wildfire originating within the WUI would be heavily suppressed by local firefighting resources. We have assumed that no wildfire ignitions are successful within the WUI.

2.3 Fire Weather and Climate Adjustment

The weather that contributes to the growth and distribution of wildfire can be separated into two distinct drivers: 1) the weather before the onset of wildfire impacts fuel conditions by making those fuels drier or wetter, and 2) the 'fire weather' from the time of ignition that can increase intensity and which drives wildfire across the landscape. To represent a wide range of possible weather-driven fire conditions across the landscape within the simulations employed here, at least a decade of high spatial and hourly resolution weather data is used. The National Oceanic and Atmospheric Administration's (NOAA's) Real-Time Mesoscale Analysis (RTMA; https://www.nco.ncep.noaa.gov/pmb/products/rtma/) surface weather data reanalysis from 2011-2020, augmented when necessary by RTMA data from Iowa State (https://mtarchive.geol.iastate.edu/) and precipitation data from Oregon State's PRISM (Parameter-elevation Regressions on Independent Slopes Model; https://www.prism.oregonstate.edu), was selected. These data represent the present year weather conditions at 2.5km horizontal resolution by utilizing assimilation and interpolation of conventional and remotely sensed data to provide a realistic and useful representation of the surface weather that drives wildfire behavior. Ten years was chosen to represent a large range of possible weather conditions with which to drive the fire behavior model in Monte Carlo simulations for both current and future years.

2.3.1 Current Year Fire Weather Source Data

The primary inputs needed to drive the fire spread model are fuels, topography, and weather. Since the methodology for developing fuel and topography inputs is described elsewhere in this methodology, this section describes only the methodology through which "historical" or current year weather inputs were assembled. "Future" (+30y) inputs are also addressed in the next section.

Wind speed and direction, relative humidity, and temperature inputs were assembled from the RTMA dataset which provides hourly estimates of sensible surface weather variables on a 2.5 km grid for the Continental U.S. Relative humidity was calculated from air temperature and dewpoint temperature in the RTMA time series, and wind speed and direction were calculated from the individual *u* and *v* wind components. Wind speed (ws, mph), wind direction (wd, °), relative humidity (rh, %), temperature (tmpf, °F), and precipitation (precip, mm) were merged from the three RTMA time series. By merging the data in this way, the amount of missing data was reduced from ~4% to about 0.02% to 0.03%, except for precipitation which was missing approximately 3.9% of its hourly frames because the Iowa State RTMA archive does not include precipitation. As a fix to this, missing hourly precipitation data was linked to pseudo-hourly PRISM precipitation data. For the ~0.02% to 0.03% of quantities/timesteps that are missing from both the NCEI and Iowa State RTMA archives, the quantity's previous timestep was used. Yearly, stacked multiband GeoTiffs for

each quantity were created, with each band in these stacked GeoTiffs corresponding to a particular hour of the year, *i.e.* band 1 is 00:00 UTC on January 1, band 2 is 01:00 UTC on January 1, and so on.

Next, the ELMFIRE repository[1] command line tool *nfdrs2016lfm* was used to calculate the live herbaceous and live woody fuel moisture content from those GeoTIFFs based on the Growing Season Index concept (Jolly et al., 2005) introduced into the National Fire Danger Rating System in its 2016 update. Stacked daily VRTs were then calculated, and used to calculate hourly frames of dead fuel moisture by size class (1-hr, 10-hr, 100-hr, and 1000-hr) and ERC(G) using standard NFDRS procedures (Bradshaw et al., 1983). Solar heating is not included in this calculation because RTMA does not include solar radiation, but future work may use the RTMA quantity total cloud cover to estimate downward shortwave solar fluxes (Holtslag, 1983) and their influence on dead fuel moisture content. Hourly dead-fuel moisture and ERC(G) GeoTIFFs were then created in a manner analogous to the native quantities described previously.

ERC(G) breakpoints (*i.e.*, the ERC(G) values corresponding to integer percentiles from 0 to 100) were completed for later use in converting raw ERC(G) values to ERC percentile values. Those breakpoints are then used to convert the raw ERC(G) values (Btu/ft^2) ERC(G) percentiles. All quantities are then resampled and split into 48 km by 48 km tiles at 600 m resolution to prepare them for use in the fire simulations.

2.3.2 Future Weather Time Series Estimation

Mid-century fire weather inputs were generated by statistically adjusting 2011-2020 RTMA temperature, relative humidity, and precipitation by computing distribution changes between present and 30 years into the future ensemble regional model output. Temporal ranges for the “historical” and future “plus 30 years” (+30y) calibration data were defined as 2011-2020 and +26y to +35y (e.g. 2048-2057 for a target year of 2022) ensemble means, respectively. To represent conditions likely typical of the +30y weather, we scale the 2011-2020 RTMA time series to estimate +30y conditions. To do this, we used CMIP6 SSP245 ensemble results as downscaled within NASA’s Earth Exchange Global Daily Downscaled Projections (NEX-GDDP-CMIP6; Thrasher et al. 2021 and Thrasher et al. 2022) data to represent the expected climate conditions 30 years into the future across CONUS. NEX-GDDP-CMIP6 is a bias-adjusted, downscaled version of CMIP6 model outputs (Eyring et al. 2016) available on a daily 0.25 degree grid over CONUS. The CMIP6 SSP245 results were chosen as the basis for Fire Factor as that scenario is a relatively middle-of-the-road carbon emissions and socioeconomic impacts scenario. (We have also computed an “upper bound” scenario for wildfire risk using the more extreme SSP585, which follows the same methodology and is available to data subscribers and research partners that are interested in examining an extreme upper limit of future wildfire risk.)

[1] https://elmfire.io/getting_started.html#clone-elmfire-github-repository

While wind is an essential fire weather variable, it was excluded from statistical adjustment. While the scientific literature does not support a statistically robust climate change signal (e.g., Torralba et al., 2017), we recognize that accurate winds are crucial to the accurate prediction of wildfire behavior, and because studies have shown that large scale winds are unlikely to change with climate change at magnitudes larger than the expected local variability over periods of 30 years (Finney et al., 2011; Abatzoglou & Brown, 2012), we have chosen to keep the 2011-2020 RTMA winds unchanged for the creation of the +30y wind time series instead of attempting to scale them using NEX-GDDP modeled results. Downscaled climate model results have difficulty achieving sufficient spatial fidelity in the wind fields to support fire models (Finney et al., 2011; Westerling et al., 2011; Abatzoglou & Brown, 2012) and high resolution future winds generated by an atmospheric model (e.g. WRF) driven by CMIP6 boundary conditions would require extensive verification and validation to establish a level of confidence necessary to use them for our wildfire behavior simulations. Since the goal is not to recreate any particular fire event, but to use the weather time series to support a range of weather conditions suitable for Monte Carlo simulations, we concluded that holding the winds unchanged from the 2011-2020 time series for the +30y simulation would be a reasonable simplification, and allow us to focus on the appropriate scaling of the other weather variables.

The NASA NEX-GDDP downscaled CMIP6 SSP245 outputs at daily resolution were used to scale the 2011-2020 RTMA hourly time series of air temperature, relative humidity, and precipitation only by computing bias adjustments between the “historical” and “forecast +30y” conditions. Statistical bias adjustment was performed independently at each geographic grid point. In order to facilitate this, the 0.25 degree rectilinear NEX-GDDP data first had to be interpolated to the 2.5-km curvilinear RTMA grid. The National Center for Atmospheric Research Command Language’s (NCL’s) regridding package from the Earth System Modeling Framework (Righi et al., 2020) was used for this purpose. We used bilinear interpolation for temperature and relative humidity, and conservative regridding for precipitation since it does not represent a smoothly varying field.

The biases were then distributed at each gridpoint throughout the day via application of a gamma distribution to maintain the diurnal signal in precipitation and humidity while allowing for the overall scaling to be representative of the climate change impacts on these variables. Extreme high or low values (e.g. humidity with negative values, or large values greater than 100%) resulting from the application of the biases to the time series were adjusted to correspond with expected daily lows and highs to allow for consistent statistics while preserving the general climate variability. Air temperature adjustments at the hourly resolution were likewise adjusted with a simpler gaussian distribution that bias-corrected the daily average values of the 2011-2020 RTMA time series to be consistent with statistics of the future +30y NEX-GDDP values.

The result for the projected “+30y” weather time series is a 10 year duration, hourly resolution representation of 30-year future weather conditions at 2.5km horizontal resolution that are characterized by 1.7-2.8 deg C (3-5 deg F) warmer temperatures across CONUS, with much more modest fluctuations in precipitation and humidity (~-3.5% to 2.0% change in mean RH), while the

wind is the exact same hourly wind field as represented in the “historical” time series. This allows the impact of higher air temperatures from climate change on fuel conditions in +30y to be isolated and evaluated, since winds and fuels are both held constant from historical to +30y. The greatest deficiency of this approach is that it is not possible to evaluate the climate impacts of geographically coherent but temporally variable events such as more severe or longer droughts, or greater incidences or intensities of atmospheric rivers or hurricanes. For example, the amount of zero-precipitation days will be unchanged between the present-year and +30y weather conditions - the drought frequency will be the same in both time series. As such, these climate impacts are limited largely to the effects on fuels caused by higher air temperatures and so should be considered a conservative underestimate of the possible magnitude of the effects on wildfire probability especially in areas with increasing drought severity or frequency; a future version of the Fire Factor model may use a different approach to describe future weather conditions to address these issues.

2.3.3 Technical Description

The adjustment of historical weather observations towards a future climate was performed using code originating from the bias_correction Python3 package (https://github.com/pankajkarman/bias_correction). Bias correction techniques like those employed here are used to correct modeled projections by adjusting them with statistical scaling factors derived between historical model output and observations; put another way, they are used to downscale climate change projections to station locations (e.g., Fang et al., 2015, Luo et al., 2018). Likewise, we use them here to adjust RTMA output with respect to scaling factors computed between present-year and +30y NEX-GDDP-CMIP6 output. We summarize the techniques here.

RTMA precipitation projections were obtained via *gamma distribution mapping,* a technique developed by (Switanek, et al., 2017). Gamma distribution mapping is unlike other bias correction methods because it accounts for the frequency of rain days and the likelihood of events.

After summing hourly RTMA precipitation into daily accumulations to match the temporal resolution of the NEX-GDDP-CMIP6 data, this procedure goes as follows:

1. Define rain days (RDs) as those which feature non-zero precipitation accumulations for each distribution. Then compute the expected number of projected 2050 RTMA rain days (RD_P):

$$RD_P = RD_{RTMA} \times \frac{RD_{NEX-GDDP-F}}{RD_{NEX-GDDP-H}} \quad (2)$$

where RD_{RTMA}, $RD_{NEX\text{-}GDDP\text{-}F}$, and $RD_{NEX\text{-}GDDP\text{-}H}$ are the number of rain days in RTMA, +30y NEX-GDDP-CMIP6, and present-year NEX-GDDP-CMIP6 data, respectively. In the event NEX-GDDP-CMIP6 +30y has fewer RDs than present-year NEX-GDDP-CMIP6, this results in a reduced number of precipitating days (and, in turn, hours) in the nudged RTMA distribution. Note that projected RTMA RDs can never increase above original RTMA RDs, an important limitation in this approach.

2. Fit gamma probability density functions (PDFs) to each of the modeled rain-day distributions. Cumulative distribution functions (CDFs) and their inverses (ICDFs) are found from these PDFs.

3. Calculate the relative scaling (SF_R) between the fitted RTMA and 2020 NEX-GDDP distributions at all CDF values corresponding to the precipitation events of the RTMA time series:

$$SF_R = \frac{ICDF_{RTMA}\left(CDF_{RTMA}\right)}{ICDF_{NEX-GDDP-H}\left(CDF_{RTMA}\right)} \quad (3)$$

where SF_R is an array of relative scaling factors, $ICDF_{RTMA}$ and $ICDF_{NEX\text{-}GDDP\text{-}H}$ are the ICDFs for the fitted 2020 RTMA and NEX-GDDP distributions, respectively, and CDF_{RTMA} is the estimated CDF for RTMA precipitation values. As an example, say the largest value in the RTMA time series is equal to 40 mm and corresponds to a CDF value of 0.997 (in other words, $ICDF_{RTMA}(0.997)$ will yield 40 mm), but $ICDF_{NEX\text{-}GDDP\text{-}H}(0.997)$ yields only 6 mm (we discuss these systematic magnitude discrepancies in *Assumptions and Limitations*). The most extreme nudged value will have a relative scaling factor of 6.67 (40/6).

4. Calculate recurrence intervals (RIs) from the three fitted CDFs, then find the adjusted RI for 2020 RTMA:

$$RI_{SC} = max\left(1, \frac{RI_{NEX-GDDP-F} \times RI_{RTMA}}{RI_{NEX-GDDP-H}}\right) \quad (4)$$

where $RI_{NEX\text{-}GDDP\text{-}F}$, RI_{RTMA}, and $RI_{NEX\text{-}GDDP\text{-}H}$ correspond to the RIs for the RTMA and 2050 and 2020 NEX-GDDP data, respectively. The value is always greater than or equal to 1 to ensure that the subsequent step yields values between 0 and 1. This step adjusts the RI of 2050 NEX-GDDP events by differences in the extremity of 2020 RTMA and NEX-GDDP events. For example, if the RI for the most extreme 2020 RTMA value is shorter than that of the most extreme 2020 NEX-GDDP value, then the RI for the most extreme 2050

NEX-GDDP value will be shortened accordingly. RI_{SC} is then used to find the corresponding scaled CDF values with:

$$CDF_{SC} = 1 - \frac{1}{RI_{SC}} \quad (5)$$

where CDF_{SC} reflects the scaling of the change in NEX-GDDP event likelihoods between 2050 and 2020 with respect to RTMA likelihoods.

5. The initial array of projected RTMA values is:

$$RTMA_I = ICDF_{NEX-GDDP-F}\left(CDF_{SC}\right) \times SF_R \quad (6)$$

where $ICDF_{NEX\text{-}GDDP\text{-}F}$ is the ICDF for the 2050 NEX-GDDP- data. In the event that (1) adjusted the RDs for the projected time series, $RTMA_I$ is linearly interpolated along the adjusted length of RD_P.

6. The array of projected values is then placed back into the RTMA time series at the corresponding locations. For example, if the largest annual RTMA value occurred on April 21st, then the largest projected RTMA value will be placed on that same day.

7. Last, the ratio between the projected and original RTMA values for each day is applied to the hourly RTMA precipitation time series.

Figure 5. Example showing results of temperature nudging from a subset in Iowa. The overall rightward shift for the NEX-GDDP data (grayscale) leads to a commensurate rightward *shift in the RTMA data (colors).*

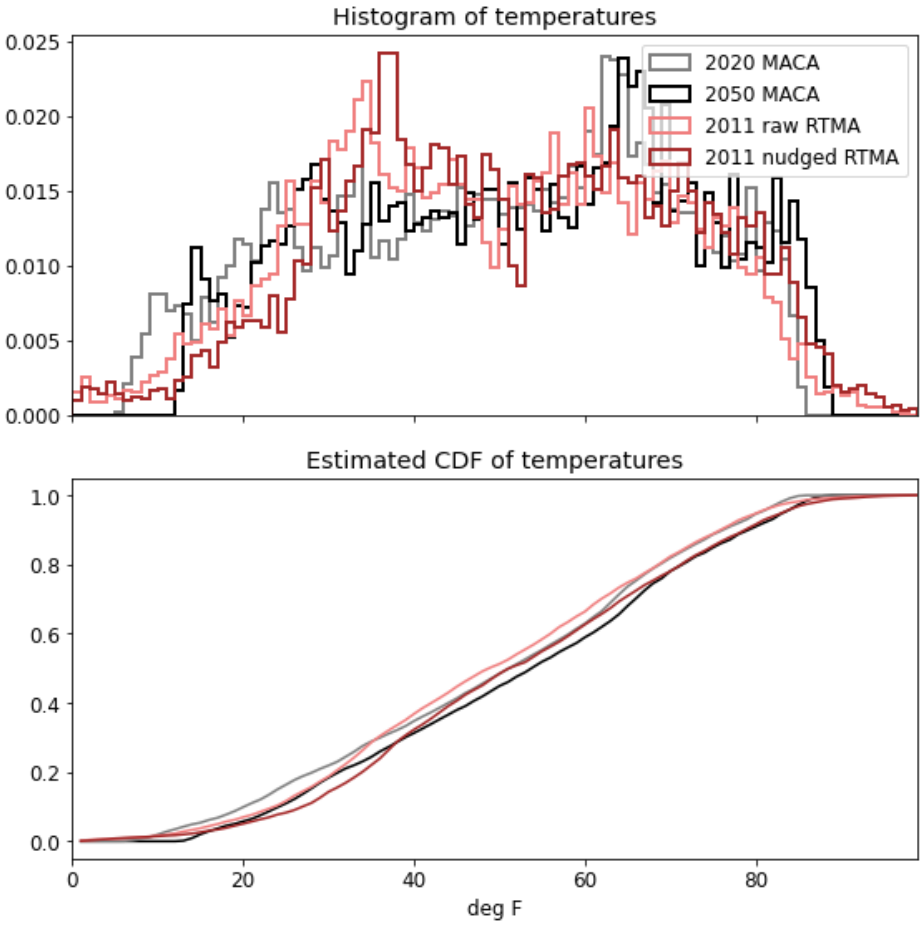

Scaling Factor

RTMA temperature projections were obtained via a *normal distribution mapping* technique (Switanek, et al., 2017). After applying cubic spline interpolation to daily minimum and maximum NEX-GDDP temperatures to obtain hourly distributions (we discuss this further in *Assumptions and Limitations*), the steps go as follows:

1. All three distributions are linearly de-trended to get a more accurate measure of the natural variability. While trends are added back at the end, all subsequent steps use the detrended time series.

2. Gaussian PDFs are fit to each of the annual distributions, then corresponding CDFs and ICDFs are derived from these.

3. An absolute scaling factor is found:

$$SF_A = \left[ICDF_{RTMA}\left(CDF_{RTMA}\right) - ICDF_{NEX-GDDP-H}\left(CDF_{NEX-GDDP-H}\right)\right] \times \left(\frac{\sigma NEX-GDDP-F}{\sigma NEX-GDDP-H}\right) \quad (7)$$

where σNEX-GDDP-F and σNEX-GDDP-H are the standard deviations of the 2050 and 2020 NEX-GDDP data and all other terms are defined as before.

4. RIs are calculated from the CDFs, scaled with (3), then used to find the modified CDF with:

$$CDF_{SC} = 0.5 + sgn\left(CDF_{NEX-GDDP-F} - 0.5\right) \times \left|0.5 - \frac{1}{RI_{SC}}\right| \quad (8)$$

Eq. (6) differs from (4) because the normal distribution is two-tailed.

5. The initial array of projected RTMA values is:

$$RTMA_I = ICDF_{NEX-GDDP-F}\left(CDF_{SC}\right) + SF_A \quad (9)$$

6. As before, reinsert projected values into the original RTMA time series. Then add the trend of the RTMA time series back into the projected one.

Mid-century relative humidity projections used a comparatively simpler approach called *empirical quantile mapping* (Gudmundsson et al., 2012). Unlike the previous two methods, it makes no assumptions about the underlying distribution of the data:

1. An empirical CDF (ECDF) was approximated for the 2020 NEX-GDDP distribution. For relative humidity, where the maximum value for humidity (100%) occurs frequently (and is therefore not an extreme) - such an approach allows for the “extremes” to behave as they would.
2. The corresponding percentiles from the ECDF are found in the RTMA data.
3. The difference between the value at each equivalent percentile was computed between the +30y and the current year NEX-GDDP data.
4. This difference in (3) was applied to each observation in the RTMA data based on its percentile.

In this way, the order of observations in the 2020 record is maintained (preserving underlying variability) while shifting towards a future climate.

Figure 6. 50th percentile Relative Humidity (RH) nudging outcomes.
Spatial differences in the delta (2050-2020; bottom right) come down to those in the underlying NEX-GDDP data. The difference between RTMA and NEX-GDDP representation of RH is large but has not yet been fully assessed.

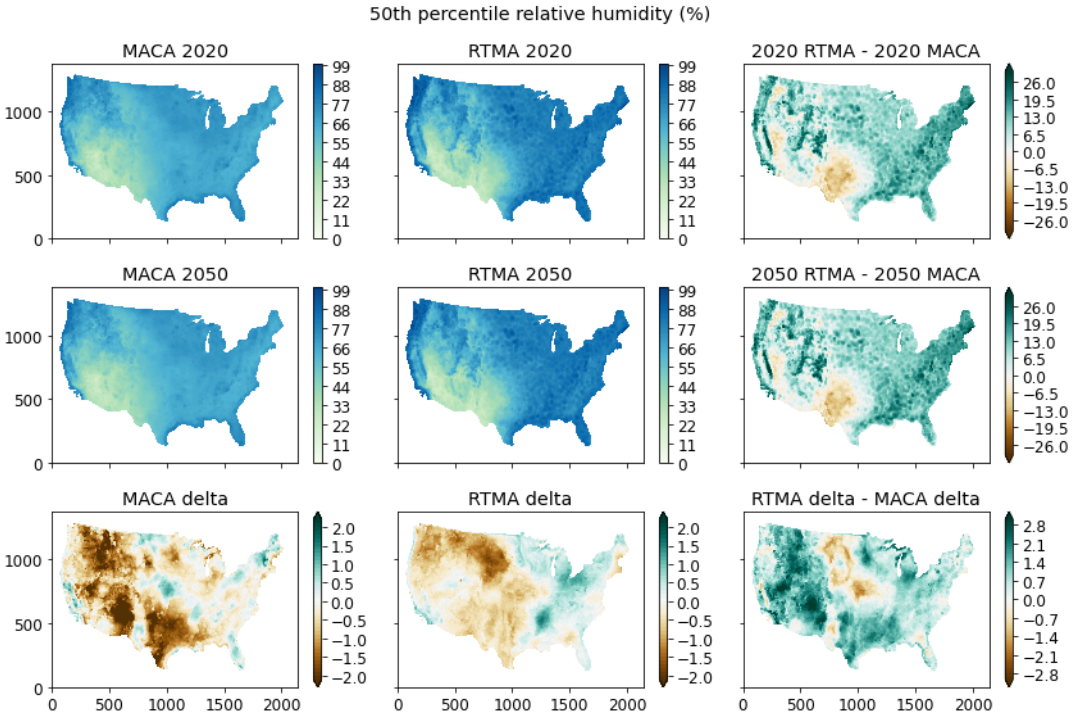

2.3.4 Assumptions and Limitations

The statistical bias adjustment of past weather towards future conditions required a multi-step statistical process, which in turn required a choice or decision to be made in the selection of the statistical test or approach. At each decision point we consciously chose the most conservative approach, to avoid generation of spurious values which could lead to dramatic intensification of fire weather. Preferring such conservative choices is in line with the selection of a conservative SSP245, and other aspects of the project that are seeking not to overestimate the future wildfire risk, but instead err on the side of caution so as to best understand the dominant factors in future fire risk. The downside to a conservative choice is that as fire behavior is sensitive to extreme conditions, which may increase in future climates in ways that our conservative statistical nudging does not account for, our selections could cause future fire risk calculations to systematically underpredict fire frequency and intensity. Sensitivity analyses on a regional basis may be performed to assess the most likely impacts of statistical choices on fire behavior and risk.

Climate change has impacted sensible fire weather both in changes in the magnitude/frequency of weather events, as well as the spatiotemporal characteristics of critical events. Examples of this include earlier or later onsets of rainy/dry seasons, downsloping wind events (i.e. Chinook, Santa Ana, Diablo), and summer-like heat waves or meteorological droughts. In turn fire behavior will change, with the fire season expected to broaden and lengthen. The statistical adjustment approach we applied will adjust past weather towards these future conditions, but does not explicitly generate new historically out-of-season, low-frequency, or extreme weather events, which may be important drivers of many new, expanded fire events in the future. Our approach adjusts the overall distributions to represent future climate, preserving historical seasonality, and the frequency of extreme events relative to the historical distribution over 2011-2020. In sum, future fire weather predictions are likely to underestimate actual fire risk, particularly in "shoulder seasons" where historically fires may have been rare, but, in the future, fires could be expected to generally occur more frequently.

To represent the future climate, we utilize the means of multiple GCMs and then build statistical distributions from the ensembles of these GCMs. This approach dampens future changes of extreme events in any single GCM run. By remapping future distributions to observed historical sequences in this way, the frequency of extreme events remains fixed relative to historical occurrence and is concurrent with the change in distributions of extreme events being damped. Together, this creates a bias of reduced extreme events in future projections, with subsequent reductions in fire events and behavior.

Each adjustment technique comes with its own limitations. Computational limits required utilization of an empirical quantile mapping applying an absolute rather than relative adjustment for each percentile, resulting at times in negative relative humidities which otherwise could have been avoided (though super-saturated conditions could still occur). In either unphysical case, the results were masked out as missing data. An alternative, potentially superior approach may be to assign a value of 100% RH to represent saturation (as in the case of supersaturation) or zero (as in the case of negative values). While neither case appeared to happen at significant scale, the overall impact to the larger Monte Carlo wildfire simulation results is unclear but is likely to contribute to an underestimation of risk. Given additional time to develop appropriate methods the applied adjustment would be relative rather than absolute (as in Grenier, 2018). Meanwhile, all methods used here have the limitation of preserving their original time series while only adjusting the magnitudes of the values with respect to future NEX-GDDP projections. This is particularly significant for the adjusted precipitation, since an increase in precipitating days in NEX-GDDP +30y would not lead to a commensurate increase in precipitation frequency in the bias-adjusted RTMA results - a topic that will require further research to resolve. We note that many downscaling techniques exist for precipitation and temperature; Luo et al., (2018) did an intercomparison of several methods, and found that empirical quantile mapping performed best for both variables in the context of a discharge model.

The data itself also presented challenges, in particular the use of daily distributions (the NEX-GDDP data resolution) to adjust hourly ones (RTMA). We assumed that daily maximum and minimum temperatures occurred 12 hours apart and applied cubic-spline interpolation to generate

synthetic hourly temperature time series to facilitate the adjustment technique (which required equal sample sizes), but recognize that this interpolation does not necessarily realistically reflect diurnal temperature cycles. That said, given the location, date, and minimum and maximum daily temperatures, it is possible to construct reasonable hourly temperature profiles (Waichler and Wigmosta, 2003), something which could be explored further in a later version of the product, if desired. Meanwhile, the use of only daily minimum and maximum relative humidity values to adjust hourly data is also not ideal. Techniques exist to derive hourly relative humidity profiles from daily data (Waichler and Wigmosta, 2003), and could be used to achieve more realistic distributions. To better maintain thermodynamic consistency with the temperature adjustment, a future version of this process could derive hourly dew point temperature profiles from the reconstructed temperature and relative humidity, perform the adjustment with the normal distribution mapping used for temperature, then re-calculate relative humidity (or alternatively, adjust both variables with the empirical quantile mapping, if sensitivity tests do indeed determine it produces more satisfactory results). Understanding the structural, spatiotemporal differences between historical observations and the representation in climate models (i.e. assessment of bias or error) is crucial for understanding how issues may propagate from observation to climate projection, and has not yet been performed. Again, the impacts on the overall Monte Carlo simulations may have both regional and temporal dependencies and would require investigation.

Precipitation adjustment was particularly challenging. As a result of the multi-ensemble, decadal averaging of daily accumulations, the NEX-GDDP precipitation distributions were substantially muted in terms of the extremes, wherein the highest values of NEX-GDDP were approximately an order of magnitude less than for the RTMA data. It is thought that this contributed to occasional spikes of spuriously large accumulations of precipitation at inappropriate time steps. Spikes were removed by limiting the maximum ratio between the adjusted and raw RTMA daily precipitation to 1.3 (i.e. SF_R, eq. 6), consistent with maximum modeled increase in extreme precipitations noted in NCA4 (Easterling et al., 2017). It is still unclear exactly of the significance of the number and location of the values that were damped by setting this ceiling, and how the overall risk estimated results were impacted. It is also worth noting that the NEX-GDDP time series at many grid points did not contain any non-precipitating days at all, likely another consequence of the decadal-ensemble averaging that effectively biases the time series. Hence, while the gamma distribution mapping technique has the inherent limitation of never producing more rain days in the future, the underlying data introduce another limitation of there not being fewer rain days in the future, either. In a future version, it would be best to preserve the full range of precipitation values in the NEX-GDDP ensembles. One possibility is to generate the NEX-GDDP distributions by randomly sampling, for example, 1000 values at each latitude-longitude grid point out of the entire decadal time series for each ensemble member, then randomly sampling *N* values from this larger pool, where *N* is equal to the length of the RTMA precipitation time series (this will vary depending on if it is hourly or daily accumulations). This should result in a reliable downward adjustment of rain days when appropriate given the changes in NEX-GDDP projections over the next 30 years. It is unknown to what degree the time vector misalignment between RTMA and NEX-GDDP may have impacted results, but is likely minor given the small range and large number (100 million) of simulations.

2.4 Wildfire Behavior Model

In this section, we document the methodology that has been used to generate annualized fire probability and hazard layers that provide a foundation for the Fire Factor product. The foundation for this product is the open source wildfire behavior model ELMFIRE (Eulerian Level Set Model of Fire Spread) fire model, which is a highly parallelized model that was used to both simulate fire spread and quantify the wildland fire risk via Monte Carlo simulations. ELMFIRE is a Rothermal-based, level set model used to track boundaries across the landscape based on the numerical solutions of Rehm and McDermott (2009) and is fully described in Lautenberger (2013). The fire probability and hard layers were generated using a series of scripts and command line tools found in the ELMFIRE repository (https://github.com/clauten/elmfire). Although the initial ELMFIRE (Eulerian Level set Model for FIRE spread) publications (Lautenberger, 2013; 2017) present a 2D fire spread model, the ELMFIRE repository has expanded to the point that the ELMFIRE fire spread model itself is now a small fraction of the overall code base, with the bulk of scripts and tools providing functionality to download and process weather data, calculate fire weather indices and fuel moisture content, process satellite data, and develop rasters such as ignition density that are needed for annualized burn probability modeling. To provide transparency and repeatability, this methodology document provides a step-by-step guide to generating the fire probability and hazard layers from scratch.

The overall fire hazard and probability modeling methodology is based on Finney et al. (2011), best practices described by Scott et al. (2018), and a relatively recent review of simulation-based burn probability modeling (Parisien et al., 2019). Consequently, the contribution of this work is not developing new techniques or approaches to fire probability and hazard modeling, but rather implementing computationally efficient and scalable modeling techniques based on existing fire probability and hazard modeling paradigms pioneered by others (Finney et al., 2011; Scott et al., 2018). These scalable computing techniques make it possible to conduct CONUS-scale fire probability and hazard simulations at 30m resolution with a cycle time of less than one week, providing orders of magnitude reductions in wall clock time compared with existing software. The simulation was optimized to run on a 22 node linux cluster, each running Dual AMD EYPC 2nd Generation 7742 chips with 64 Core apiece, running at 2.25GHz with 1TB of DDR4 3200 ECC memory. The cluster also included over 500TB of network attached storage to store inputs and outputs. In this configuration, ELMFIRE was capable of completing over 100 million wildfire simulations at 30m resolution across the CONUS domain in approximately 5 days of wall-clock time. The CONUS domain was subdivided into 48km by 48 km tiles, which were likewise surrounded by 8 similar tiles in a 3x3 grid pattern.

Inputs to ELMFIRE include fuels, weather time series, and ignition locations. While the fuels and weather time series were previously described, the ignition locations were based on historical fire locations of sizes greater than 100 acres (see the justification of this choice in the following subsection). The selection of historical fires of greater than a particular size was done to implicitly

include the effect of human-driven fire suppression activities in the model output to create a “real world” estimate of fire risk. For example, the State of Rhode Island has exhibited remarkable fire suppression over the past decades and has been able to eliminate all fires over 100 acres during the 1992-2018 time period, driving the effective burn probability in Rhode Island to zero for all properties.

For each ignition location, a weather “draw” was randomly selected for that fire which would be carried forward many hours in simulation, and could extend anywhere in the 3x3 (144x144 km) tile domain. Those simulated fires that grew to sufficient size (100 acres) were tracked and the locations, fire length, and durations were noted. This process was repeated over 100 million times, and simulations were started incrementally for each day of a year throughout the 10-year sample time series. This resulted in approximately 8-10 million tracked fires of significance per simulation period for the present year and +30y targets.

2.4.1 Ignition - Modeling spatial fire occurrence patterns

One of the primary indicators of where future fires will occur is historical fire occurrence data. The spatial component of the fire occurrence model is built from the Fire Occurrence Database (FOD) developed by the USDA Forest Service (Short, 2014; Short 2021). The FOD includes 27 years (1992-2020) of fire occurrence data, encompassing 2.17 million georeferenced wildfire records and accounts for 165 million acres burned. In a departure from some studies that remove small (<100 acre) fires prior to analysis (following the guidance in Scott et al., 2018), this database was not filtered to remove small fires for the FSF-WFM. Different thresholds (e.g. 300 acres (Scott et al., 2018), 100 ha / 247 acres (Dillon et al., 2015)) have been used in other research and models. For this study, we used all FOD wildfires greater than 1 acre in size, and we incorporated into the fire behavior modeling the impacts of geographically-variable suppression, as provided by the US Forest Service’s Wildfire Suppression Difficulty Index (https://data.nal.usda.gov/dataset/wildfire-suppression-difficulty-index-map-service-0).

The ignition density used for v2 is a refined version of a kernel-smoothed density. Within each pyrome, the density can be viewed as a mixture of one spatially uniform distribution and one Gaussian distribution per historical FOD ignition point, the Gaussian radius being determined by the class ignition cause: natural, human, or unknown. Each mixture term allocates its probability only to cells with burnable fuels. Formally, this density is equivalent to the following sampling procedure for drawing an ignition location:

1. Select a pyrome (the probability of each pyrome is proportional to the historical number of fires in it in the FOD). Denote $\lambda \in [0, 1]$ to be the mixture coefficient parameter of the uniform component for that pyrome.
2. Draw a random $U \in [0, 1)$.
3. If $U < \lambda$: we have chosen to sample from the uniform component.

   a. Draw a random location p_1 in the pyrome.
   b. If that location is burnable, return it; otherwise go back to the beginning of step 3.
4. If $U \geq \lambda$: we have chosen to sample from historical points. Pick a random historical ignition point p_0; denote c the cause class of p_0, and r_c the Gaussian radius parameter corresponding to that cause class.
   a. Draw a point p_1 by doing a "random jump" from p_0 drawn from an isotropic 2-dimensional Gaussian distribution (therefore corresponding to smoothing with an isotropic Gaussian kernel): $p_1 \sim N(\mu = p_0, \Sigma = r_c^2 I_2)$
   b. If p_1 is a burnable location, return it; otherwise go back to step 4a.

This procedure involves 4 parameters per pyrome – the uniform component coefficient λ, and the 3 Gaussian radii r_c, one per ignition cause class (human/natural/unknown) – chosen by fitting to the historical data. Said more formally, a Bayesian-refined version of a Pseudo-Likelihood Cross-Validation (PL-CV) procedure was used: an optimization algorithm searched for the parameter vector which maximized the log-likelihood of test points given training points, with an additional regularization term corresponding to a prior distribution on the parameters (to prevent the radii to be driven to zero). The population of historical ignitions used for fitting the density was the entire FOD database of CONUS fires greater than 1 acre in size. The locations considered burnable were those with a corresponding burnable fuel model.

One last refinement was made by eliminating any ignitions within the WUI area by zeroing the ignition density within those boundaries to prevent over-prediction of fire sizes. This choice was justified since WUI fire risk overwhelmingly arises from wildland-ignited fires that propagate into the WUI rather than the other way around, and any urban-ignited fires are typically quickly suppressed.

2.4.2 Modeling temporal fire occurrence patterns

The previous section describes how the spatial fire occurrence is modeled, but it does not address when large fires occur. One of the strongest predictors of temporal occurrence of both the number of large fires and acres burned is National Fire Danger Rating System (NFDRS) Energy Release Component (ERC) percentile based on fuel model G, or ERC'(G) [(Riley et al., 2013). To note, ERC(G) refers to raw ERC values (Btu/ft^2) and ERC'(G) refers to ERC percentiles.

Mathematically, ERC is 4% of the energy per unit area (Btu/ft^2) that would be released during a fire. ERC depends on live and dead fuel loading by size class (as characterized by an NFDRS fuel model) as well as fuel moisture content of live and dead fuels. ERC varies due to changes in moisture content of both live and dead fuels, which are in turn dependent on prior precipitation, relative humidity, and temperature. Although NFDRS fuel model G, which shows the best

correlation with fire occurrence and burned area, contains loadings across all dead fuel size classes and live herbaceous / live woody loadings, it has a heavy loading in the 1000-h size class. For that reason, ERC(G) is primarily a function of weather conditions over the preceding 45 days and can be thought of as a measure of intermediate to long term dryness. Being calculated solely from fuel moisture content, ERC is not a function of wind speed, slope, or spread rate.

Correlation of fire records Fire occurrence is normally assessed in terms of ERC percentile as opposed to raw ERC (Btu/ft^2) because ERC percentile shows better correlation with fire occurrence and size than raw ERC, since the same amount of precipitation corresponding to wet conditions in one region may correspond to dry conditions in another region.

Correlation of fire records with ERC'(G) (Riley *et al.* 2013) shows that the fraction fires occurring at or below a particular ERC'(G) is a power-law function of ERC'(G) percentile, leading to the dependency shown in Figure 7-ERC. In this work, spatiotemporal fire occurrence patterns are proportional to the fixed ignition density raster from Section 2.4.1 multiplied by the function shown in Figure 7-ERC. In this way, the probability of a fire occurring at a particular location and time depends on both historical fire occurrence and the instantaneous level of dryness as reflected by ERC'(G).

Figure 7-ERC. Fraction of fires occurring at or below ERC'(G).

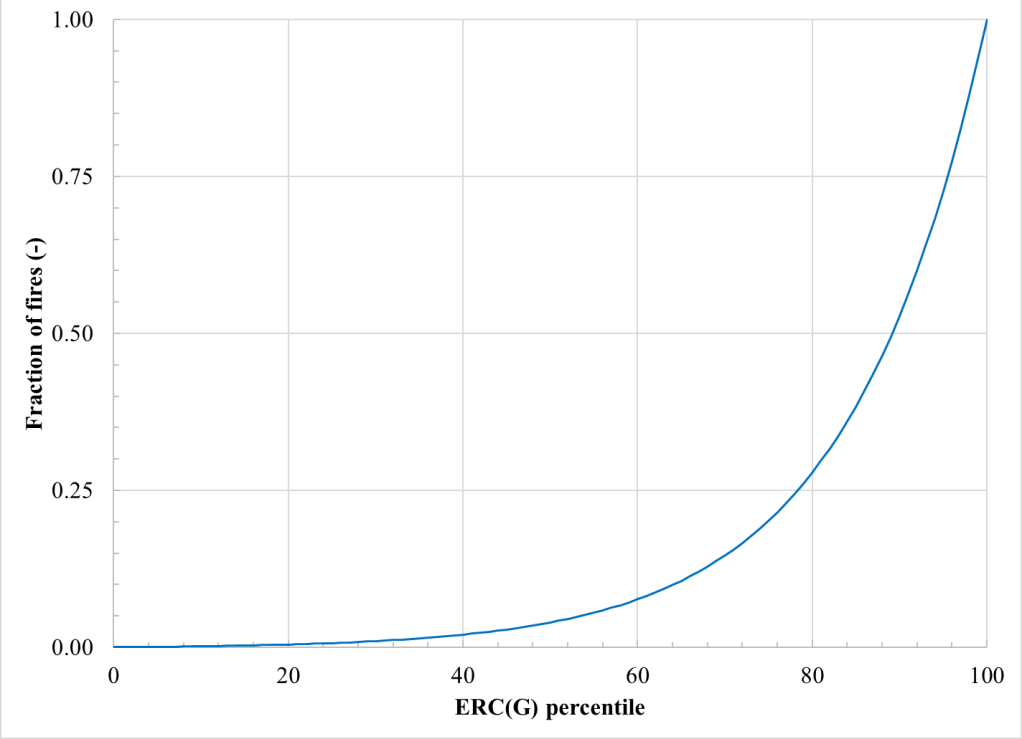

2.4.3 Fire spread model

The 2D fire simulator ELMFIRE (https://elmfire.io, https://github.com/lautenberger/elmfire; Lautenberger, 2013) is used here to drive a stochastic fire spread analysis that is used to generate CONUS burn probability and hazard surfaces. ELMFIRE's computational engine is similar to other two-dimensional fire simulators such as FARSITE (Finney, 1998) in that it calculates surface fire spread rate using the Rothermel surface spread model (Rothermel, 1972; Albini, 1976), assumes that each point along the fire front behaves as an independent elliptical wavelet (Richards, 1995) with length to breadth ratio determined empirically (Finney, 1998; Anderson, 1983), simulates transition from surface to crown fire using the Van Wagner criterion (Van Wagner, 1997) (with crown fire spread rates calculated from Cruz *et al*. (2005)), and models spotting as a stochastic process with a lognormal spotting distance distribution (Sardoy et al., 2008; Perryman et al., 2013). ELMFIRE tracks the fire front using a narrow band level set method (Sethian, 1996), a numerical technique for tracking curved surfaces on a regular grid. Parallelization is achieved using Message Passing Interface (MPI). (Real-time ELMFIRE simulations can be visualized at https://pyrecast.org where ELMFIRE is used to model the progression of hundreds of millions of fires ignited across California per day and forecast the spread of initial attack and ongoing fires across the Continental US.)

To demonstrate how ELMFIRE simulates fire spread, Figure 8 shows 24-hours of fire progression from an individual ignition site. The black contour lines in Figure 8a represent fire front position at 2-hour intervals. Figure 8a also shows which parts of the burned area experienced surface fire (blue), passive crown fire (green), or active crown fire (red). Figure 8b similarly shows fire perimeter contours and flame length variation within the fire perimeter. Flame length is highest in areas that burn as heading fires or that experience crown fire and lowest in areas that burn as a flanking, backing, or surface fire. In this example, the fire area after 24 hours of spread is approximately 560 acres.

The Monte Carlo fire spread analysis conducted here involves running millions of fire spread simulations similar to that shown in Figure 8. The basic procedure is as follows:

1. Loop sequentially over weather time series years (2011-2020), then over all CONUS tiles. Here, a tile is a 144 km by 144 km tile, consisting of a 48 km central tile surrounded by its eight neighboring tiles of the same size.
2. For each year / tile, read in fuel and topography inputs as well as the yearly weather / fuel moisture / ERC percentile inputs.
3. Starting at the beginning of the year, determine ignition locations using the spatial and temporal fire occurrence modeling techniques described earlier. Fires are ignited only in the central 48 km tile, but can spread into the adjacent 8 tiles.

4. Model the progression of each fire from the time of ignition for a spread duration determined by weather conditions, and moderated by the corresponding level of geographically-variable suppression described by the US Forest Service's Suppression Difficulty Index.

5. For each pixel within the modeled fire perimeter, increment the number of times burned. Increment discrete ember count and flame length bins for each pixel accordingly.

6. Increment time by one day and repeat steps 3-5.

Figure 8. Example ELMFIRE fire spread simulation for individual fire ignition. (a) Fire type (surface fire, passive crown fire, or active crown fire). (b) Flame length.

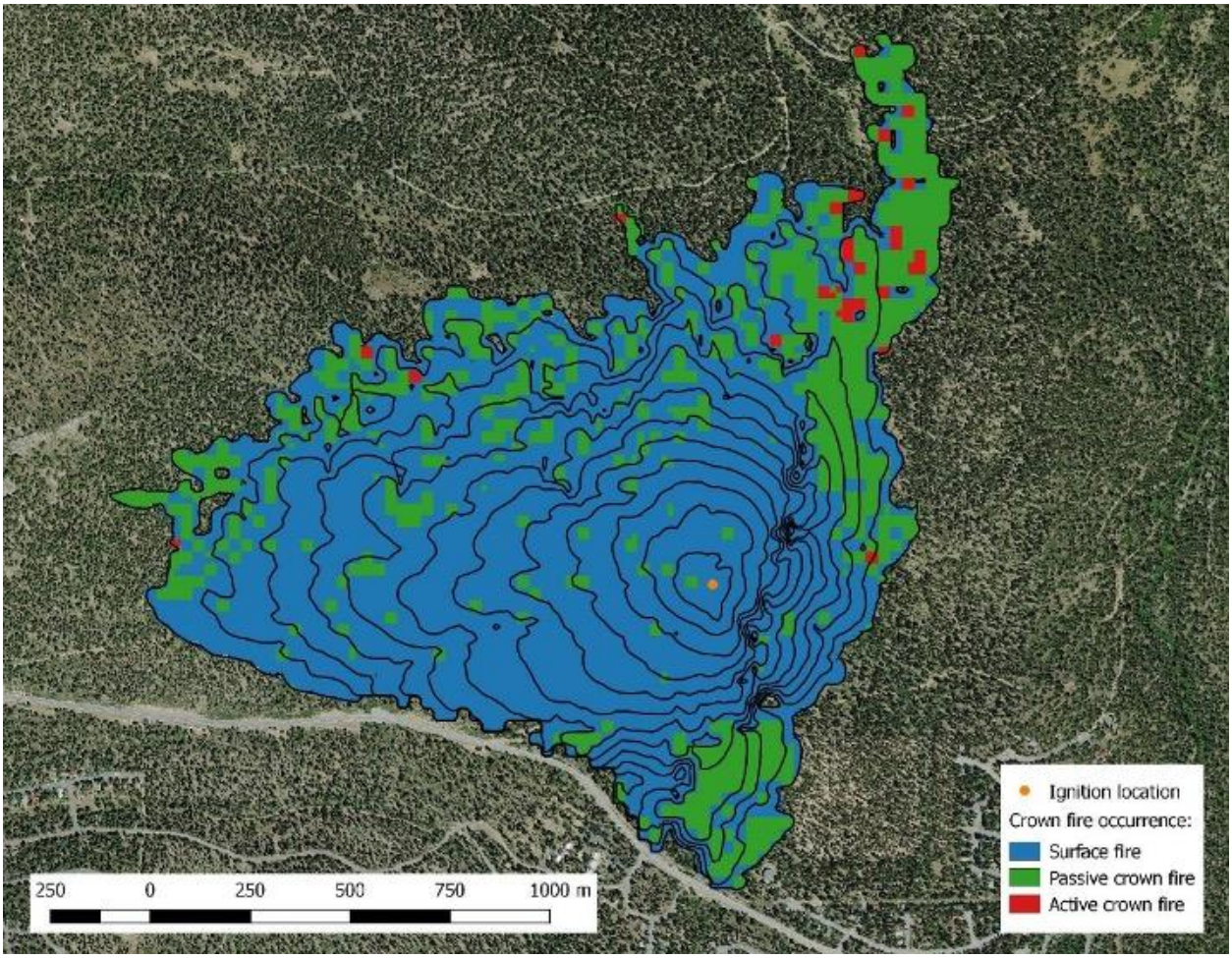

Figure 8(a)

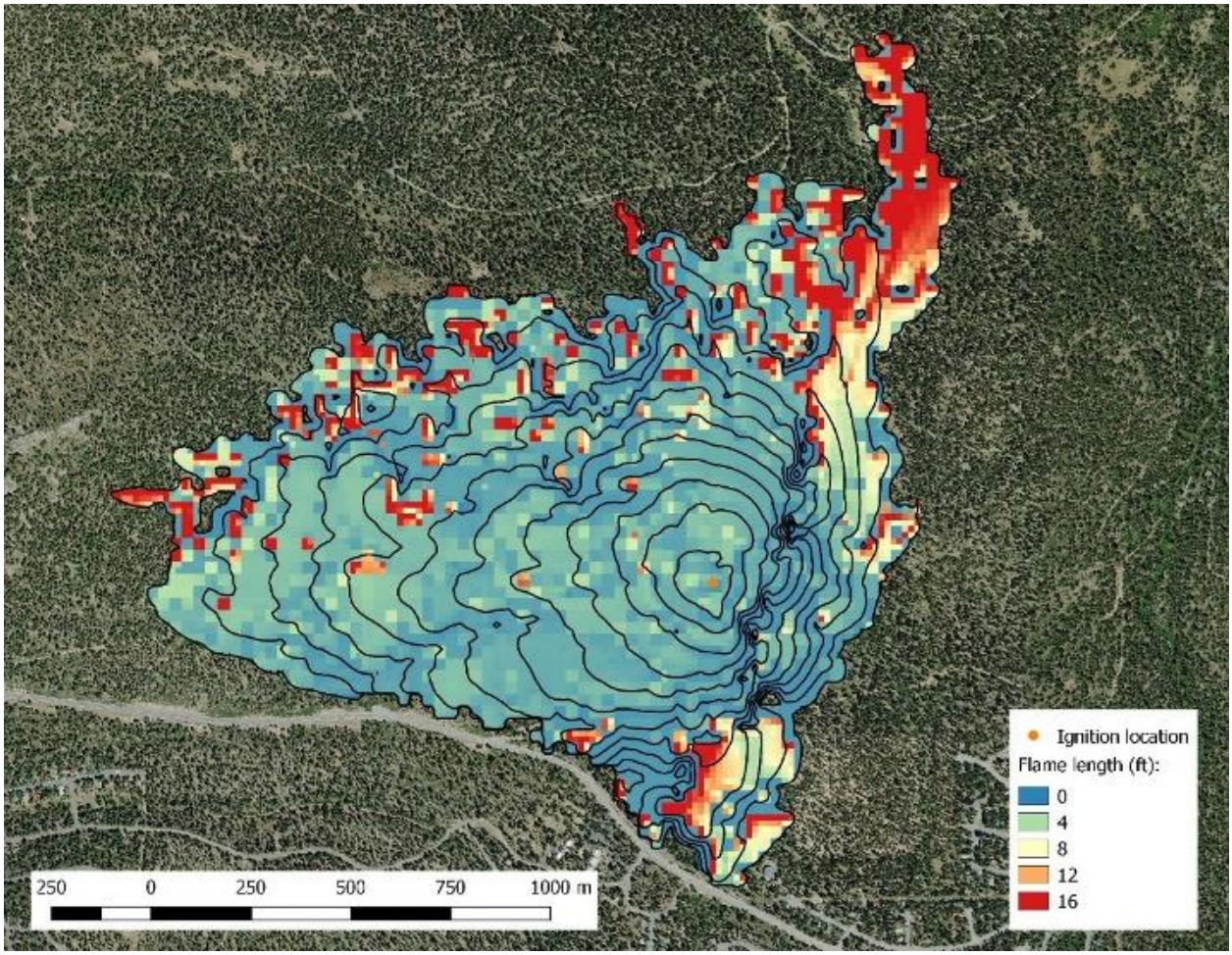

Figure 8(b)

Since fires can start in one tile and spread to adjacent tiles, each tile is post-processed concurrently with its 8 neighbors when summing fire probability and hazard layers.

The mechanics of running a CONUS burn probability simulation are as follows:

1. Navigate to the directory annual_burnprob/runs in the ELMFIRE repository and create a new folder called *e.g.*testrun. Copy all files and the subdirectory empty_run from the production01 folder to the newly created folder and navigate to the newly-created folder.

2. Edit the file hosts to specify the hostnames and number of “slots” (CPU cores, not threads) available on each host.
3. Execute the script 00a-loop.sh. This script creates a subdirectory called tiles and then loops over the ~4,000 tiles per year necessary for a CONUS run, sequentially running

ELMFIRE for each year/tile on hosts as specified in the hosts file and saving model outputs for each tile. Run time is approximately 5 days on 20 × 128 core nodes.

4. After each year has been run in ELMFIRE, the script 02a-parallel_merge.sh is automatically launched from within 00a-loop.sh to post-process all tiles for that year. It takes approximately 6-7 hours to post-process all tiles for a given year.

5. After all years/tiles have been run and post-processed, the yearly outputs must be aggregated together. This is done by launching the 04a-loop.sh script, which launches several instances of the 04b-aggregate.sh script.

Note that extreme “plume” fires (e.g. the Camp Fire of 2018) with very large flame lengths/intensities that have significant influences on their own weather are not capable of being accurately simulated using ELMFIRE at this time. Such a simulation would require a coupled fire behavior-weather model such as that described in Coen and Schroeder (2015).

Calibration of Burn Probabilities

Smooth rescaling

If the sampling of ignitions was perfectly realistic, the burn-probability map could simply be computed by dividing the burn-count map from by the number of simulated fire seasons. However, we do not rely on that assumption. Instead, the burn-count outputs of the Monte Carlo simulations are divided not by a constant factor, but by a function which varies smoothly over space. This function is designed so that the burned acreage averaged over large areas agree with the historical record (FOD). Effectively, the algorithm learns from simulation outputs how many fire seasons it has simulated, and that number varies smoothly from one region to another. The interpretation is that Monte-Carlo simulations are tasked with estimating the small-scale relative variations in wildfire risk, while the FOD remains the ground truth overall. Note that the rescaling layer is derived from the present year simulation, and then also applied to the future +30y simulation.

The detailed method for computing the rescaling layer is the following. Both the burn-count layers and the size-weighted historical FOD fires (1999-2020 period) within 30m bins are blurred by a Gaussian kernel with a 90km radius. The raw burn count layer is then divided by the ratio of blurred burn count to the blurred size-weighted FOD count. Finally, the resulting layer is multiplied by the spatially constant scalar that results in making it closest to the blurred FOD, which is virtually equivalent to making it agree with the CONUS-wide burned acres per year for the period described by the FOD. The burn probability divided by the burn count, i.e. the ratio of initial to final layer, can be interpreted as the spatially varying number of years of simulation, which is plotted as contour lines in Figure 9-BP.

Figure 9-BP. Final burn probability (colors) and spatially-varying number of simulated years (contour lines).

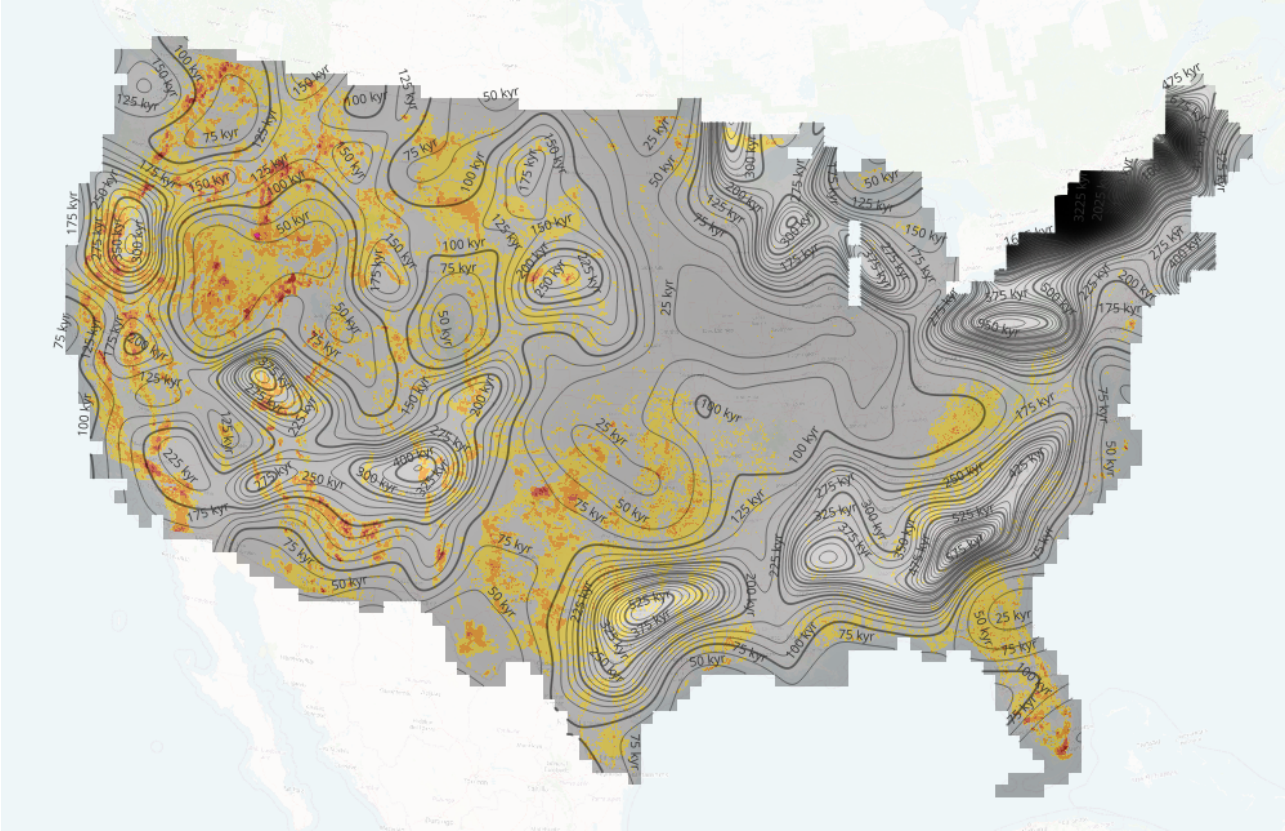

The sharp NE gradient is a Gaussian-tails artifact caused by fire absence in the FOD historical record in that area. Soft-capping - imposing a limit of the maximum size of burn probability

In a few areas, the burn probability layer presented sharp overprediction anomalies due to some fires presenting excessive concentrations and/or size, resulting in burn probabilities that exceeded the regrowth capacity of fuels - i.e. it is unrealistic that so many fires could repeatedly burn in the same location since the impact on available fuels would limit their occurrence. This was addressed by correcting each pixel's burn-probability via a "*soft-capping"* transformation:

$$p \rightarrow (p^{-1} + 2yr)^{-1}$$

This transformation prevents burn-probabilities from exceeding 50%/yr, while leaving probabilities much smaller than 50%/yr practically unchanged. This correction is more principled than a hard cap on burn probability, as it is being motivated by a notion of *no-return* interval, whereby fire cannot return to a location before two years have passed, after which it returns with the same frequency as predicted by simulations, thus addressing the shortcomings of the assumption of many repeated burns at the same location being possible in the FSF-WFM.

2.4.4 Validation

To validate the results from the fire behavior model, we compared the model fires against the FOD's historical fires' intensity and size on a pyrome-by-pyrome basis, following the definition of pyromes supplied by the US Forest Service (Short et al, 2020). We validate the FSF-WFM resulting burn probabilities for each pyrome by comparing the Monte Carlo simulation fires to the fires in the FOD.

Using a divergence metric that compares the modeled fires to the FOD, we calculate that FSF-WFM v2 are now in better agreement in aggregate with the historical information in the FOD than in FSF-WFM v1. We expect this improvement is due to the application of a geographically-variable suppression model within ELMFIRE, and since the simulation end time is no longer limited to a 7 day maximum duration (as was true in v1). Figure 10 depicts an example of the correlation between the FOD and ELMFIRE fire numbers and sizes for a selected pyrome; a discussion of the methods and metrics used and the full list of pyrome calibration figures is included in Appendix B.

Figure 10. An example of the comparison between the FOD (blue), FSF-WFM v1 (orange), and FSF-WFM v2 (green) for pyrome #16 (central-eastern Oregon).

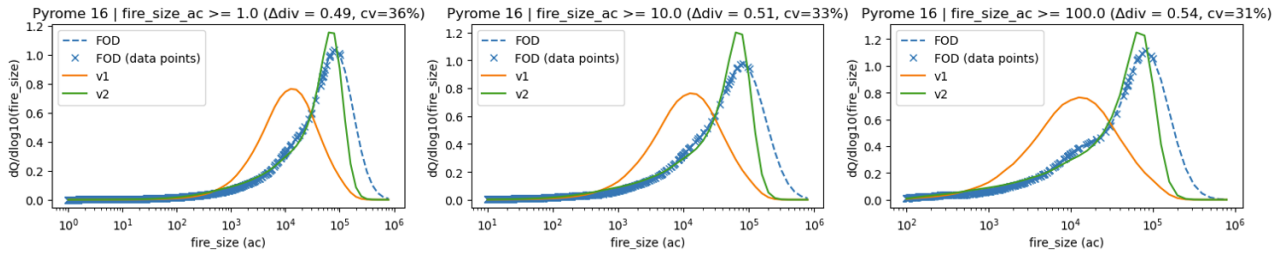

Not all pyromes saw a similar improvement, however. See Appendix B for a full discussion.

2.4.5 QA/QC Process for Fuels and Burn Probability (BP)

Disturbance Raster

We used a remote sensing approach to ensure that we did not alter fuel loads in areas that did not experience disturbance. All pixels with moderate or high severity disturbance were checked against a carbon loss raster (see Section 2.2.1 for details). Due to the nature of the Global Forest Watch dataset, we were not able to use this approach to check whether areas disturbed by low-severity treatments included false positives, but low-severity disturbances do not result in large alterations to surface or canopy fuels so this is unlikely to have a significant impact on modeled fuel loads.

WUI

To evaluate whether the RF model replaced non-burnable pixels in the WUI interface and intermix with surface fuel models that were consistent with the surrounding area, the FM40 contexts were checked at both the local and the landscape scale. At the local scale, we summarized the FM40 composition surrounding a predicted pixel on ~5 samples on each of the 11 Landfire superzones (Fig. 1 in Reeves et al. 2009). For each sample point, we summarized the percent of pixels in a 0.5km buffer around that point that shared the same FM40 class. In the most fire-prone Superzones (1-5), the fuel models that replaced nonburnable fuel classes were primarily 101 (Short, Sparse Dry Climate Grass) and 121 (Low Load, Dry Climate Grass-Shrub). In the 24 sample points located in Superzones 1-5, the replacement value was present in the 0.5km buffer area 88% of the time, indicating that the replacement value was typically a component of the local fuels. In the six Superzones that tend to be less fire-prone, the replacement value was present in the 0.5km buffer area 65% of the time. This is likely because the dry grass and dry grass-shrub fuel types are more prevalent in the dataset and being used as replacement values more often than humid-climate fuels.

Fire perimeters in WUI areas were also visually compared to evaluate whether the 1 mi buffer from wildland vegetation was an appropriate buffer.

Figure 11. Example of WUI Zones With Disturbance Raster

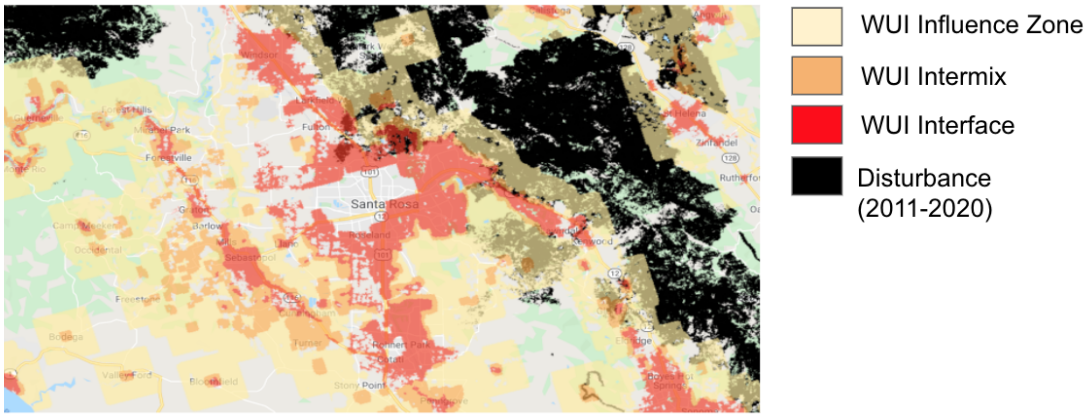

Burn probability

To evaluate the burn probability results, we compared the modeled burn probability to the only other existing CONUS-wide burn probability predictions available, a dataset known as Wildfire Risk to Communities (WRC). We used WRC as a point of reference to establish where results were similar and where they differed. If different, we sought to explain the reason for this difference.

We selected focal areas to be representative of the CONUS domain, using the USFS-defined pyromes (128 total defined) and selecting the top 10% (13 pyromes) that have the largest absolute difference between Fire Factor (FF) results and Wildfire Risk to Communities products (WRC; www.wildfirerisk.org).

We first compared fuels across the FF and WRC model results. We created bar charts of the aggregated surface fuel classes to compare LANDFIRE (LF) versions of fuels: LF 2014, LF 2014b (T. Smail personal comm., 2022), LF 2016, and this effort's FF fuels. We constructed a confusion matrix for each of the 13 pyromes for all 40 FM40 classes to compare differences between models. Differences among these fuels have been found to be highly indicative of the differences found in the FF and WRC model outputs.

FIRST STREET FOUNDATION

2.5 Risk Assessment at the Property Level

2.5.1 Hazards and Exposure

The primary outputs of the above process are conventional annualized burn probability rasters at 30m resolution with CONUS coverage, including:

- Burn probability - an estimate of the likelihood that a region on the landscape burns in a single year period
- Fire intensity (flame length) - Multiple representations of simulated flames across all scenarios including the maximum flame length experienced, the sum of all flames experienced, and a histogram of conditional (upon burning) flame lengths using discrete flame length bins
- Exposure to embers - Similar to the flame length bins, ember exposure is tracked to characterize the relative intensity of ember exposure from all modeled fires

The result is a statistically well-characterized set of simulated wildfires from which the probabilistic exposure of properties and buildings to wildfire hazard based on likelihood, flame length, and ember cast may be derived. The likelihood of a 30m pixel burning is derived from the count of the number of times that pixel had ignited over the course of all simulations. The flame length is a measure of fire intensity, captured as binned flame lengths (see Table 7. Exposure Measures) over the distribution of all fires within the pixel, and may be expressed as the mean, median, or maximum flame length. The sum of the flame length bins gives the number of times burned, which can be used with the sum of flame lengths to compute the average flame length. The ember cast is a binned measure of the number of times embers - as pushed ahead of a simulated fire by the fire weather time series - land in a pixel.

Following the ELMFIRE simulations for the present year and +30y into the future, the wildfire hazard for any 30m pixel within CONUS is represented by the combination of the burn probability, mean or maximum flame length (intensity), and exposure to embers. The full range of statistics is listed below:

Table 7. Exposure measures

Measure of Exposure	Description	Units
Burn Probability	Likelihood that a pixel catches fire out of all the simulations normalized by likelihood of ignitions.	%
Max Flame Length	-Maximum flame length experienced at a pixel across all simulations	ft
Sum of Flame Length	Sum of flame length for all simulations that experience fire	ft
Mean Flame Length	Sum of flame length divided by times burned	ft
Binned Counts of Flame Lengths	(0, 2, 4, 8, 12, 20, 20+)	ft
Ember Flux	Dimensionless number that is a proxy for the count of embers landing in a pixel. Does not reflect mass of embers, whether they are still burning, or distance traveled.	<none>
Ember Likelihood	Likelihood that an ember falls into a pixel across all simulations, similar to times burned	%
Max Embers	Max number of embers	count

The resulting burn probability for FSF-WFM v2 for the present year is shown in Figure 11 as an example of these outputs. All outputs may be viewed at RiskFactor.com .

2.5.2 Risk Score Assignment

The Fire Factor risk assessment was created on a property-level basis across CONUS. Property parcel geometries are provided by the Lightbox public-record property boundaries database. Building footprint geometries are defined by Mapbox. First Street performed a geometric intersection to match parcels to building footprints. Footprints that cross parcel boundaries were subdivided, such that no footprint geometry crosses parcel boundaries. Since some parcels

intersect multiple footprint geometries, the building footprint with the largest area was designated the primary footprint.

To evaluate the exposure to wildfire flames and embers, each hazard layer was queried at the geometric centroid of each building footprint and parcel. For scoring purposes, at properties with a building footprint the statistic at the primary footprint centroid was recorded; for parcels without a building footprint the parcel centroid was recorded. The assignment of a 30-year, climate-adjusted aggregated wildfire risk score was then computed by calculating the likelihood and nature of exposure through burn probabilities and presence of embers for a building or parcel as representative of the risk for each property for the present year and for +30y, and then linearly interpolating across that 30 year period.

Figure 12. Burn Probability Hazard Layer for 2023 as calculated from the FSF-WFM

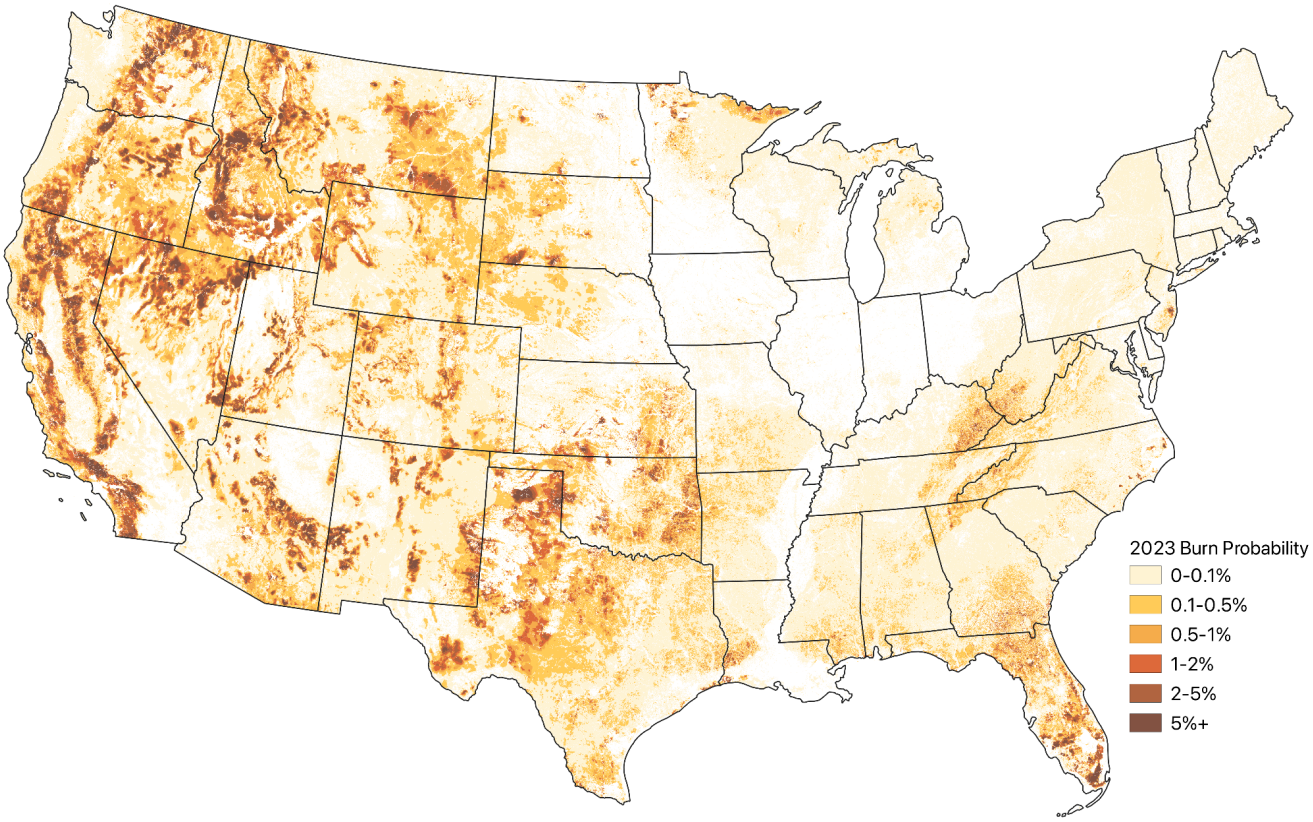

Due to the stochastic nature of the ember spread model and computational limitations even at tens of millions of simulations, not all properties at risk of ember cast received embers in an actual simulation. To address this, especially as related to assignment of a risk score to parcels, a kernel

function is used to create an “ember zone” from the modeled embers. The kernel creates a zone which is 210 meters (7 pixels) surrounding any estimated ember landing locations. This “ember zone” represents how far isolated embers may land from dense ember landing areas. Relatedly, the nature of the simulations resulted in some areas in the future with slightly decreased burn probabilities or ember likelihoods. A floor was added to the model statistics which does not allow future simulations to decrease from the current modeled burn probabilities or ember likelihoods by using the current year’s burn probability as the value for the future burn probability when it is higher than what the model simulations otherwise produces, holding burn probability constant in those areas.

FIRST STREET FOUNDATION

Summary and Discussion

The physical risk associated with wildfire incidence has been computed for the contiguous United States at 30 meter horizontal resolution, and is expressed through hazard layers quantifying burn probability, flame length, and ember spread for the present year and 30 years into the future. An open-source wildfire behavior model, ELMFIRE, was used to compute these hazard layers and was driven by augmented LANDFIRE-based estimates of fuel types, densities, and conditions at 30m resolution for the current year . The built environment within the Wildland Urban Interface (WUI) that is represented by nonburnable fuels within LANDFIRE were replaced in the fuel inputs by the results of machine-learning estimates that draw upon 549 representative, verified WUI fires from a total of approximately 3,000 documented historical fires, with the goal of allowing wildfire to propagate through the WUI in the fire behavior model in a way that more closely resembles observed conditions (see Appendix A). Future vegetation at +30y was assumed to be static since the present year, to simplify the understanding of the 30-year risk.

ELMFIRE was driven by fire weather derived from the NOAA RTMA surface reanalysis for 2011-2020 that capture a wide range of weather conditions to create the current year's hazard layers, and was driven by the same time series in +30y but with air temperature, precipitation, and humidity scaled to +30y conditions as represented by the NASA NEX-GDDP downscaled CMIP6 SP245 climate model ensemble results. Winds were held static from the present to the +30y simulation period to preserve the high resolution aspect of the present year time series in the future, to reduce uncertainties in future fire behavior and in recognition that future winds are likely to change far less significantly with climate change than other weather parameters.

Fire ignition locations for the simulations were the same for current year as for the +30y simulations, and were created from an analysis of all fires, including small fires. Fires were modeled and tracked at 30m resolution within 48km by 48 km spatial tiles, surrounded by 8 similar tiles that allow each fire to spread throughout the domain. Over 150 million simulated fires were created and tracked within a Monte Carlo simulation scheme, with over 60 million fires growing to a size and severity that warranted tracking and continued simulation. Geographically-variable suppression impacts were included in the simulations, and ELMFIRE spread rates were calibrated against the FOD's historical fire sizes and numbers on a pyrome-by-pyrome basis. The characteristics of the resulting modeled fires were then aggregated to create burn probability, flame length, and ember spread hazard estimates at 30m horizontal resolution for CONUS. These hazard estimates are conducive with assessing the exposure of buildings on US to wildfire flames and/or embers and, when combined with specific building vulnerability, could be used to provide estimates of climate-adjusted wildfire losses.

The current year's fire hazard derivation is heavily dependent upon the updated LANDFIRE v2.0.0 2016 fuel layers, and significant effort was undertaken to assemble all known disturbances, including recent fires, prescribed burns, harvests, thinning, etc. The replacement of areas within

the WUI that are represented as nonburnable within LANDFIRE leads to an improvement in the representation of fire behavior in the WUI areas, which leads to non-zero burn probabilities that are more representative of observations (Massada et al., 2009). Ignitions were not allowed to originate within the WUI. Keeping the 2022 fuels static for the assessment of +30y future risks focuses attention on the effects of climate and future weather on the state of those fuels, which has significant implications for wildfire ignitions, intensity, and spread (Penman et al., 2014).

Validation of the methodology depends upon comparison of modeled fires with the distribution of historical size and intensity. Additional comparisons to alternate risk assessment methods (e.g. Wildfire Risk to Communities) and the derivative losses estimates to the historical numbers of aggregate home losses in states across CONUS have also been useful in establishing confidence in this methodology. By matching the historical distribution of wildfires' sizes and intensities in each pyrome (following the methodology of Scott et al. 2018) the simulation has produced results that are useful in aggregate when scaled as a risk index.

There are a number of acknowledged limitations in the methodology, which are discussed below.

- Very large fires - the simulation method does not capture the behavior of very large fires, since the fire weather forcing the simulation is not directly coupled within the fire behavior model.

- House-to-house ignition - while the replacement of the non-burnable fuels in the LANDFIRE representation of the WUI with burnable fuels allows wildfires to propagate through the WUI more accurately, the ignition and subsequent contribution to wildfire by the buildings/houses within the WUI is not yet explicitly modeled.

- Vegetation changes over 30 years - the vegetation between present year and +30y was held static, although it is anticipated that changes in vegetation composition and density – and thus fuels – will be driven by climate change.

- Future weather approximation - the fire weather in +30y was approximated by scaling the 2011-2020 time series used to drive the ELMFIRE simulation for current year hazards, except for winds which were held static over the 30 year time period. The resulting high-quality winds in +30y simulations based on 2011-2020 observations is an advantage over using modeled winds, but results in a future time series that is representative of a range of fire weather conditions. Most importantly, since the length and severity of droughts captured in the 2011-2020 time series do not change for the +30y simulation, the impact of those droughts (increasing in frequency and severity under CMIP6 SSP245 estimates) is systematically underestimated by using the current methodology.

- Incomplete fuels/disturbances - disturbances are not evenly reported across the US, and some areas (e.g. many private lands in the Eastern US) are not well known.

- No future land use changes - to focus on the impacts of climate change on existing parcels under future wildfire exposure, we have elected to keep the built environment static, and to assume no changes in land use or condition. This simplifying assumption is useful for its stated purpose, but we also recognize that changes in land use would also precipitate changes in likely future ignition locations, WUI locations, fuel conditions and types.

Future Versions of the FSF-WFM may include improvements to fire behavior models that address the above limitations. Estimates of the impacts of smoke from the modeled fires, updating future climate scenarios using the most recent CMIP results that would enable better estimate of drought impacts, considering multiple future climate scenarios, and possibly driving a high-resolution weather simulation for future fire weather estimates are possible.

Data distribution

The resulting Fire Factor hazard layers and associated property-specific vulnerability and economic assessments will be freely and publicly available for noncommercial use at https://riskfactor.com. The public availability of this climate information is meant to inform the public of their wildfire risk now and in the future, level the playing field with private commercial interests that already have access to this kind of information, and help address the privatization of climate impacts information.

FIRST STREET FOUNDATION

Model Team and Partners

The First Street Foundation is grateful for the support of our philanthropic donors and guidance from our Advisory Board, without whom this project would not have been possible. The following First Street Foundation current and past personnel contributed to the preparation of this document, data, or First Street Foundation products supporting this model.

Mike Amodeo	Angela Jin	Natalie Pardy
Max Alfaro	Mike Kaminski	Mariah Pope
Viviana Barajas	Shannon Keane	Dr. Jeremy R. Porter
Mark Bauer	Dr. Edward J. Kearns	Nathan Rosler
Chris Browder	Dr. Jungho Kim	Paul-Henry Schoenhagen
Dr. Kyra Bryant	Samantha La Marca	Daniel Seripap
Helena Cawley	Kelvin Lai	Michelle Shapiro
Sara Chadwick	Marguerite Lally	Evelyn Shu
Jessica Chu	Sharai Lewis-Gruss	Ilya Solnyshkin
Elena Damm	Mavis Lim	Sean Surdovel
Payal Dhanda	Lucy Litvinova	Maggie Tarasovitch
Matthew Eby	Mike Lopes	Kai Valegapudi
Neil Freeman	Sylvia Ma	Otis Wilcox
Toby Hoang	Anna McIntosh	Dr. Bradley Wilson
Quinn Hawkins	Dr. David Melecio-Vazquez	Ray Yong
Ho Hsieh	David Miller	

We are thankful for our wildfire model partners and their their invaluable contributions on wildfire science, fuels, damage estimates, high performance computing, project management and technical expertise, including:

Spatial Informatics Group:

Biplov Bhandari, M.S.	Jeff Knickerbocker	Dr. David Saah
Dr. Farrukh Chishtie	Dr. Carrie Levine	Dr. Austin Troy
Kenneth Cheung	Dr. Kel Markert	Jean-Pierre Wack, M.S.
John Dilger	Dr. Andrea McMahon	Kyle Woodward, M.S.
Teal Richards-Dimitrie, M.S.	Dr. Jarlath O'Neil-Dunne	Valentin Waeselynck, M.S.
Dr. Gary Johnson	Carl Rudeen, M.S.	Dr. Kayla Johnson
Dominick Asberry	Dr. Anna Talucci	David Schmidt, M.S.
Dr. Ian McCullough	Dr. Max Moritz	Jeff Knickerbocker
Paul Lackovic	Taro Pusina	Jordan Combs, M.S.

Cloudfire.ai:

Dr. Chris Lautenberger

Eagle Rock Analytics:

Dr. Owen Doherty
Dr. Beth McClenny

Arup:

Meg Ackerson
Ibrahim Almufti
Rebecca Birmingham
Kenny Buyco
Isaac Campbell
Laura Elbourne-Binns
Mackenzie Hill
Jack Hogan
Susan Lamont
Jinal Mehta
Natalia Sanabria
Peter Woodburn

Acknowledgements:

The First Street Foundation Wildfire Model (FSF-WFM) is the product of a collaborative partnership that began in 2020 between the First Street Foundation and the Pyregence Consortium for the development of wildfire risk models. In addition, the building vulnerability and damage implications were developed in collaboration with Arup. The entire research team thanks all of the wildfire risk professionals, scientists, and practitioners who have contributed to the development of the model.

We also give special thanks to the following individuals below who provided invaluable comments, critiques and suggestions regarding the development of our initial methodology and results following the development of FSF-WFM v1 in 2020-2021:

- Dr. Janice Cohen of the National Center for Atmospheric Research
- Dr. LeRoy Westerling and Dr. John Abatzoglou of the University of California Merced
- Gregory Dillion, Dr. Mark Finney, Eva Karau, and Dr. Karen Short of the US Forest Service Rocky Mountain Research Station
- Dr. Joel Reynolds, Dr. Marybeth Keifer, and Windy Bunn of the National Park Service
- Dr. Ben Sleeter and Nathan Wood from the U.S. Geological Survey
- Joshua Picotte, Tobin Smail, and Dr. Inga La Puma of the USFS-DOI LANDFIRE team

FIRST STREET FOUNDATION

References

Abatzoglou, J.T., & Brown, T. J. (2012). A comparison of statistical downscaling methods suited for wildfire applications. International journal of climatology, 32(5), 772-780.

Abatzoglou, J.T., & Williams A. P. (2016). Impact of anthropogenic climate change on wildfire across western US forests. Proc. Natl. Acad. Sci. U.S.A. 113,11770–11775.

Albini, F. A. (1976). *Estimating wildfire behavior and effects* (Vol. 30). Department of Agriculture, Forest Service, Intermountain Forest and Range Experiment Station.

Anderson, H. E. (1983). Predicting wind-driven wildland fire size and shape [fire behavior models]. *USDA Forest Service Research Paper INT (USA)*.

Armal, S., Porter, J. R., Lingle, B., Chu, Z., Marston, M. L., & Wing, O. E. (2020). Assessing property level economic impacts of climate in the US, new insights and evidence from a comprehensive flood risk assessment tool. *Climate*, *8*(10), 116.

Balch, J. K., Bradley, B. A., Abatzoglou, J. T., Nagy, R. C., Fusco, E. J., & Mahood, A. L. (2017). Human-started wildfires expand the fire niche across the United States. *Proceedings of the National Academy of Sciences*, *114*(11), 2946-2951.

Bates, P. D., Quinn, N., Sampson, C., Smith, A., Wing, O., Sosa, J., ... & Krajewski, W. F. (2021). Combined modeling of US fluvial, pluvial, and coastal flood hazard under current and future climates. *Water Resources Research*, *57*(2), e2020WR028673.

Bowman, D. M., Kolden, C. A., Abatzoglou, J. T., Johnston, F. H., van der Werf, G. R., & Flannigan, M. (2020). Vegetation fires in the Anthropocene. *Nature Reviews Earth & Environment*, *1*(10), 500-515.

Bradshaw, L. S., Deeming, J.E., Burgan, R.E., and Cohen, J.D. (1984). *The 1978 national fire-danger rating system: technical documentation* (Vol. 169). US Department of Agriculture, Forest Service, Intermountain Forest and Range Experiment Station.

Burke, W. D., Tague, C., Kennedy, M. C., & Moritz, M. A. (2021). Understanding How Fuel Treatments Interact With Climate and Biophysical Setting to Affect Fire, Water, and Forest Health: A Process-Based Modeling Approach. *Frontiers in Forests and Global Change*, *3*, 143.

Cohen, J. (1999). Reducing the Wildland Fire Threat to Homes: where and how much? Jack D. Cohen, RMRS. In *Fire Economics Symposium, San Diego, CA April* (Vol. 12, p. 1999).

Coen, J. L., and W. Schroeder (2015), The High Park fire: Coupled weather-wildland fire model simulation of a windstorm driven wildfire in Colorado's Front Range, J. Geophys. Res. Atmos., 120, 131–146, doi:10.1002/2014JD021993.

Cruz, M. G., Alexander, M. E., & Wakimoto, R. H. (2005). Development and testing of models for predicting crown fire rate of spread in conifer forest stands. *Canadian Journal of Forest Research*, *35*(7), 1626-1639.

Dale, L. (2009). *The true cost of wildfire in the Western US*. Western Forestry Leadership Coalition.

Dillon, G., Menakis, J., & Fay, F. (2015). Wildland fire potential: A tool for assessing wildfire risk and fuels management needs. *In: Keane, Robert E.; Jolly, Matt; Parsons, Russell; Riley, Karin. Proceedings of the large wildland fires conference; May 19-23, 2014; Missoula, MT. Proc. RMRS-P-73. Fort Collins, CO: US Department of Agriculture, Forest Service, Rocky Mountain Research Station. p. 60-76.* (Vol. 73, pp. 60-76).

Easterling, D. R., Kunkel, K. E., & Arnold, J. R. (2017). Precipitation change in the United States.

Eyring, V., Bony, S., Meehl, G. A., Senior, C. A., Stevens, B., Stouffer, R. J., and Taylor, K. E.: Overview of the Coupled Model Intercomparison Project Phase 6 (CMIP6) experimental design and organization, Geosci. Model Dev., 9, 1937-1958, doi:10.5194/gmd-9-1937-2016, 2016.

Fang, G. H., Yang, J., Chen, Y. N., & Zammit, C. (2015). Comparing bias correction methods in downscaling meteorological variables for a hydrologic impact study in an arid area in China. Hydrology and Earth System Sciences, 19(6), 2547-2559.

Finco, M., Quayle, B., Zhang, Y., Lecker, J., Megown, K. A., & Brewer, C. K. (2012). Monitoring trends and burn severity (MTBS): monitoring wildfire activity for the past quarter century using Landsat data. *In: Morin, Randall S.; Liknes, Greg C., comps. Moving from status to trends: Forest Inventory and Analysis (FIA) symposium 2012; 2012 December 4-6; Baltimore, MD. Gen. Tech. Rep. NRS-P-105. Newtown Square, PA: US Department of Agriculture, Forest Service, Northern Research Station.[CD-ROM]: 222-228.* (pp. 222-228).

Finney, M. A. (1998). *FARSITE, Fire Area Simulator--model development and evaluation* (No. 4). US Department of Agriculture, Forest Service, Rocky Mountain Research Station.

Finney, M. A., Grenfell, I. C., McHugh, C. W., Seli, R. C., Trethewey, D., Stratton, R. D., & Brittain, S. (2011). A method for ensemble wildland fire simulation. *Environmental Modeling & Assessment*, *16*(2), 153-167.

Finney, M. A., McHugh, C. W., Grenfell, I. C., Riley, K. L., & Short, K. C. (2011). A simulation of probabilistic wildfire risk components for the continental United States. *Stochastic Environmental Research and Risk Assessment*, *25*(7), 973-1000.

Gentemann, C. L., Holdgraf, C., Abernathey, R., Crichton, D., Colliander, J., Kearns, E. J., ... & Signell, R. P. (2021). Science storms the cloud. *AGU Advances*, *2*(2), e2020AV000354.

Glickman, D., & Babbitt, B. (2001). Urban wildland interface communities within the vicinity of federal lands that are at high risk from wildfire. *Federal Register*, *66*(3), 751-777.

Grenier, P. (2018). Two types of physical inconsistency to avoid with univariate quantile mapping: A case study over North America concerning relative humidity and its parent variables. Journal of Applied Meteorology and Climatology, 57(2), 347-364.

Gudmundsson, L., Bremnes, J. B., Haugen, J. E., & Skaugen, T. E. (2012). Technical Note: Downscaling RCM precipitation to the station scale using quantile mapping–a comparison of methods. Hydrol. Earth Syst. Sci. Discuss, 9(5), 6185-6201.

Hansen, M. C., Potapov, P. V., Moore, R., Hancher, M., Turubanova, S. A., Tyukavina, A., ... & Townshend, J. (2013). High-resolution global maps of 21st-century forest cover change. *science*, *342*(6160), 850-853.

Holtslag, A. A. M., & Van Ulden, A. P. (1983). A simple scheme for daytime estimates of the surface fluxes from routine weather data. *Journal of Applied Meteorology and Climatology*, *22*(4), 517-529.

Iowa State, Iowa Environmental Mesonet, 2022; accessed from: https://mtarchive.geol.iastate.edu/

Jolly, W. M., Nemani, R., & Running, S. W. (2005). A generalized, bioclimatic index to predict foliar phenology in response to climate. *Global Change Biology*, *11*(4), 619-632.

Kearns, E. J., Amodeo, M., Chadwick, S., Eby, M., & Porter, J. R. (2020, December). Making Climate Change Personal: Enabling Action Through Communication of Flood Risk Science to Individuals. In *AGU Fall Meeting Abstracts* (Vol. 2020, pp. SY040-06).

Krawchuk, M. A., Moritz, M. A., Parisien, M. A., Van Dorn, J., & Hayhoe, K. (2009). Global pyrogeography: the current and future distribution of wildfire. *PloS one*, *4*(4), e5102.

LANDFIRE (2020). Existing Vegetation Type Layer, LANDFIRE 2.0.0, U.S. Department of the Interior, Geological Survey, and U.S. Department of Agriculture. Accessed July 2021 at http://landfire.cr.usgs.gov/viewer/

Lautenberger, C. (2013). Wildland fire modeling with an Eulerian level set method and automated calibration. *Fire Safety Journal*, *62*, 289-298.

Lautenberger, C. (2017). Mapping areas at elevated risk of large-scale structure loss using Monte Carlo simulation and wildland fire modeling. *Fire Safety Journal*, *91*, 768-775.

LFD: Landfire Fuel Dictionary; accessed from: https://landfire.gov/DataDictionary/LF200/LF2016Remap_CC.pdf.

LUCAS: Land Use and Carbon Scenario Simulator; accessed from: https://www.usgs.gov/centers/western-geographic-science-center/science/lucas-model.

Luo, M., Liu, T., Meng, F., Duan, Y., Frankl, A., Bao, A., & De Maeyer, P. (2018). Comparing bias correction methods used in downscaling precipitation and temperature from regional climate models: a case study from the Kaidu River Basin in Western China. Water, 10(8), 1046.

Martinuzzi, S., Stewart, S. I., Helmers, D. P., Mockrin, M. H., Hammer, R. B., & Radeloff, V. C. (2015). The 2010 wildland-urban interface of the conterminous United States. *Research Map NRS-8. Newtown Square, PA: US Department of Agriculture, Forest Service, Northern Research Station. 124 p.[includes pull-out map].*, *8*, 1-124.

Massada, A. B., Radeloff, V. C., Stewart, S. I., & Hawbaker, T. J. (2009). Wildfire risk in the wildland–urban interface: a simulation study in northwestern Wisconsin. *Forest Ecology and Management*, *258*(9), 1990-1999.

Melecio-Vázquez, D.; Lautenberger, C.; Hsieh, H.; Amodeo, M.; Porter, J.R.; Wilson, B.; Pope, M.; Shu, E.; Waeselynck, V.; Kearns, E.J. A Coupled Wildfire-Emission and Dispersion Framework for Probabilistic PM2.5 Estimation. *Fire* **2023**, *6*, 220. https://doi.org/10.3390/fire6060220

Morin, X., Fahse, L., Jactel, H. *et al.* Long-term response of forest productivity to climate change is mostly driven by change in tree species composition. *Sci Rep* 8, 5627 (2018). https://doi.org/10.1038/s41598-018-23763-y

NOAA National Centers for Environmental Information (2022). Accessed from: https://www.ncei.noaa.gov/has/HAS.FileAppRouter?datasetname=9950_01&subqueryby=STATION&applname=&outdest=FILE

Parisien, M. A., Dawe, D. A., Miller, C., Stockdale, C. A., & Armitage, O. B. (2019). Applications of simulation-based burn probability modelling: a review. *International journal of wildland fire*, *28*(12), 913-926.

Penman, T. D., Collins, L., Syphard, A. D., Keeley, J. E., & Bradstock, R. A. (2014). Influence of fuels, weather and the built environment on the exposure of property to wildfire. *PLoS One*, *9*(10), e111414.

Perryman, H. A., Dugaw, C. J., Varner, J. M., & Johnson, D. L. (2012). A cellular automata model to link surface fires to firebrand lift-off and dispersal. *International journal of wildland fire*, *22*(4), 428-439.

PRISM: Parameter-elevation Relationships on Independent Slopes Model; accessed from: https://prism.oregonstate.edu/

Radeloff, V. C., Helmers, D. P., Kramer, H. A., Mockrin, M. H., Alexandre, P. M., Bar-Massada, A., ... & Stewart, S. I. (2018). Rapid growth of the US wildland-urban interface raises wildfire risk. *Proceedings of the National Academy of Sciences*, *115*(13), 3314-3319.

Reeves, M. C., Ryan, K. C., Rollins, M. G., & Thompson, T. G. (2009). Spatial fuel data products of the LANDFIRE project. *International Journal of Wildland Fire*, *18*(3), 250-267.

Rehm, R. G., & McDermott, R. J. (2009). *Fire-front propagation using the level set method, Tech*. Note 1611, Natl. Inst. Stand. Technol., Gaithersburg, MD, USA.

Richards, G. D. (1995). A general mathematical framework for modeling two-dimensional wildland fire spread. *International Journal of Wildland Fire*, *5*(2), 63-72.

Righi, M., Andela, B., Eyring, V., Lauer, A., Predoi, V., Schlund, M., Vegas-Regidor, J., Bock, L., Brötz, B., de Mora, L., Diblen, F., Dreyer, L., Drost, N., Earnshaw, P., Hassler, B., Koldunov, N., Little, B., Loosveldt Tomas, S., and Zimmermann, K.: Earth System Model Evaluation Tool (ESMValTool) v2.0 – technical overview, Geosci. Model Dev., 13, 1179–1199, https://doi.org/10.5194/gmd-13-1179-2020, 2020.

Riley, K. L., Abatzoglou, J. T., Grenfell, I. C., Klene, A. E., & Heinsch, F. A. (2013). The relationship of large fire occurrence with drought and fire danger indices in the western USA, 1984–2008: the role of temporal scale. *International Journal of Wildland Fire*, *22*(7), 894-909.

Rothermel, R. C. (1972). *A mathematical model for predicting fire spread in wildland fuels* (Vol. 115). Intermountain Forest & Range Experiment Station, Forest Service, US Department of Agriculture.

Sardoy, N., Consalvi, J. L., Kaiss, A., Fernandez-Pello, A. C., & Porterie, B. (2008). Numerical study of ground-level distribution of firebrands generated by line fires. *Combustion and Flame*, *154*(3), 478-488.

Scott, J. H., Thompson, M. P., & Calkin, D. E. (2013). A wildfire risk assessment framework for land and resource management. U.S. Department of Agriculture, Forest Service, Rocky Mountain Research Station.

Scott, J.H., Short, K.C., and Finney, M.A. (2018). FSim: the large fire simulator Guide to best practices. Pyrologix LLC, Available at https://pyrologix.com/wp-content/uploads/2019/11/FSimBestPractices_0.3.1.pdf

Scott, J. H., Gilbertson-Day, J. W., Moran, C., Dillon, G. K., Short, K. C., & Vogler, K. C. (2020). Wildfire Risk to Communities: Spatial datasets of landscape-wide wildfire risk components for the United States.

Sethian, J. A. (1996). A fast marching level set method for monotonically advancing fronts. *Proceedings of the National Academy of Sciences*, *93*(4), 1591-1595.

Sheehan, T., Bachelet, D., & Ferschweiler, K. (2015). Projected major fire and vegetation changes in the Pacific Northwest of the conterminous United States under selected CMIP5 climate futures. *Ecological Modeling*, *317*, 16-29.

Short, K. C. (2014). A spatial database of wildfires in the United States, 1992-2011. *Earth System Science Data*, *6*(1), 1-27.

Short, K. C. (2021). Spatial wildfire occurrence data for the United States, 1992-2018 [FPA_FOD_20210617]. 5th Edition. Fort Collins, CO: Forest Service Research Data Archive. https://doi.org/10.2737/RDS-2013-0009.5 (2021).

Short, Karen C.; Grenfell, Isaac C.; Riley, Karin L.; Vogler, Kevin C. 2020. Pyromes of the conterminous United States. Fort Collins, CO: Forest Service Research Data Archive. https://doi.org/10.2737/RDS-2020-0020

Silverman, B. W. (1986). Density Estimation for Statistics and Data Analysis. New York: Chapman and Hall.

Sleeter, Benjamin M., Tamara S. Wilson, Ethan Sharygin, and Jason T. Sherba. "Future scenarios of land change based on empirical data and demographic trends." *Earth's Future* 5, no. 11 (2017): 1068-1083.

Smith, A. B. (2022, January). 2021 US Billion Dollar Weather and Climate Disasters in Historical Context including New County-Level Exposure, Vulnerability and Projected Damage Mapping. In 102nd American Meteorological Society Annual Meeting. AMS.

Switanek, M. B., Troch, P. A., Castro, C. L., Leuprecht, A., Chang, H. I., Mukherjee, R., & Demaria, E. (2017). Scaled distribution mapping: a bias correction method that preserves raw climate model projected changes. Hydrology and Earth System Sciences, 21(6), 2649-2666.

Syphard AD, Sheehan T, Rustigian-Romsos H, Ferschweiler K (2018) Mapping future fire probability under climate change: Does vegetation matter?. PLOS ONE 13(8): e0201680. https://doi.org/10.1371/journal.pone.0201680

Taylor, K. E., Stouffer, R. J., & Meehl, G. A. (2012). An overview of CMIP5 and the experiment design. Bulletin of the American Meteorological Society, 93(4), 485-498.

Thrasher, B., Wang, W., Michaelis, A. et al. NASA Global Daily Downscaled Projections, CMIP6. Sci Data 9, 262 (2022). https://doi.org/10.1038/s41597-022-01393-4

Thrasher, B., Wang, W., Michaelis, A. Nemani, R. (2021). NEX-GDDP-CMIP6. NASA Center for Climate Simulation. https://doi.org/10.7917/OFSG3345

Torralba, V., Doblas-Reyes, F. J., & Gonzalez-Reviriego, N. (2017). Uncertainty in recent near-surface wind speed trends: a global reanalysis intercomparison. Environmental Research Letters, 12(11), 114019.

Van Wagner, C. (1977). Conditions for the start and spread of crown fire. *Canadian Journal of Forest Research*, *7*(1), 23-34.

Vose, J. M., D.L. Peterson, G.M. Domke, C.J. Fettig, L.A. Joyce, R.E. Keane, C.H. Luce, J.P. Prestemon, L.E. Band, J.S. Clark, N.E. Cooley, A. D'Amato, and J.E. Halofsky (2018). Forests. In impacts, risks, and adaptation in the United States: Fourth National Climate Assessment. *US Global Change Research Program, Washington, DC, USA.* https://doi.org/10.7930/NCA4, 232-267.

Waichler, S. R., & Wigmosta, M. S. (2003). Development of hourly meteorological values from daily data and significance to hydrological modeling at HJ Andrews Experimental Forest. Journal of Hydrometeorology, 4(2), 251-263.

Westerling, A. L., Hidalgo, H. G., Cayan, D. R., & Swetnam, T. W. (2006). Warming and earlier spring increase western US forest wildfire activity. *science*, *313*(5789), 940-943.

Westerling, A. L., Bryant, B. P., Preisler, H. K., Holmes, T. P., Hidalgo, H. G., Das, T., & Shrestha, S. R. (2011). Climate change and growth scenarios for California wildfire. *Climatic Change*, *109*(1), 445-463.

Zhao, T., and Dai, A. (2015). The Magnitude and Causes of Global Drought Changes in the Twenty-First Century under a Low-Moderate Emissions Scenario. *J. Clim.* 28 (11), 4490–4512. doi:10.1175/Jcli-D-14-00363.1

FIRST STREET FOUNDATION

Appendix A. Fires used to estimate fuels in WUI areas

Incident Name	State	Ignition Date	Lat.	Long.	Acres Burned	Total Structures Damaged	Total Structures Destroyed	Total Structures Threatened
Shockey	CA	9/23/2012	32.618	-116.335	2667	10	45	125
Bastrop County Complex	TX	9/4/2011	30.13	-97.235	31838	0	1709	1160
Pine Creek	OR	7/14/2014	44.808	-120.273	31033	0	0	16
Highway 613 Fire	MS	10/31/2014	30.507	-88.526	635	0	0	30
Carlton Complex	WA	7/14/2014	48.248	-119.96	276091	0	471	1103
Mills Canyon	WA	7/8/2014	47.626	-120.297	21952	0	3	571
Anaconda	UT	7/20/2014	40.562	-112.237	1142	0	0	30
High Range	ID	8/3/2014	45.743	-116.493	5328	0	3	30
Happy Camp Complex	CA	8/14/2014	41.707	-123.196	118491	2	6	767
Knf Beaver	CA	7/30/2014	41.89	-122.871	34274	0	6	235
Snag Canyon	WA	8/3/2014	47.167	-120.475	12508	1	22	279
Johnson Bar	ID	8/3/2014	46.096	-115.614	15170	0	0	57
Rain	ID	8/3/2014	45.583	-115.185	4772	0	0	4
Assayii Lake	NM	6/13/2014	36.032	-108.844	13176	0	5	50
Slide	AZ	5/20/2014	35.009	-111.802	22698	0	0	350
French	CA	7/28/2014	37.294	-119.36	14534	0	0	106
Way	CA	8/18/2014	35.735	-118.461	3947	12	12	1500
Eiler	CA	7/31/2014	40.799	-121.558	30967	0	30	755
Taylor Mountain Road	UT	7/5/2014	40.531	-109.573	2965	3	3	50
Triple G	FL	5/9/2015	26.118	-81.591	736	0	0	0
Grand Lake	FL	4/19/2015	25.75	-80.455	1368	0	0	11
Lime Hill	OR	8/5/2015	44.37	-117.33	12210	0	5	4
Dry Gulch	OR	9/12/2015	44.829	-117.139	18369	0	0	507
Mann	ID	8/18/2015	44.263	-116.84	1527	0	0	30
Mm43 Hwy 52	ID	6/25/2015	43.977	-116.4	11022	2	0	10
Celebration	ID	6/6/2015	43.26	-116.497	7281	0	0	0
Soda	ID	8/10/2015	43.319	-116.861	282888	1	1	145
Sleepy Hollow	WA	6/28/2015	47.455	-120.375	3238	27	35	0
I-90	WA	7/19/2015	47.013	-119.959	1397	0	0	20
Highway 8	WA	8/4/2015	45.802	-120.184	35296	0	0	350

FIRST STREET FOUNDATION

Brown Ranch	TX	8/11/2015	29.993	-100.428	17881	0	3	22
County Line 2	OR	8/12/2015	44.829	-121.412	68189	0	7	1452
Roosa Gap	NY	5/3/2015	41.638	-74.421	2747	0	0	11
Pipeline 1	PA	5/3/2015	41.123	-75.677	666	0	0	0
North	CA	7/17/2015	34.372	-117.474	4366	5	23	700
Gilmore Gulch	WA	7/5/2015	46.16	-116.964	8074	0	0	11
Tucannon	WA	8/29/2015	46.359	-117.678	2809	0	0	140
Ridge Road	ND	4/14/2015	48.079	-103.09	3390	0	0	0
Powerline	OK	1/26/2015	35.364	-95.884	1183	0	0	11
Highway	CA	4/19/2015	33.907	-117.624	1212	0	0	252
Z Bar 7	OK	3/31/2015	36.664	-96.149	5908	0	0	0
2230 Road	OK	4/4/2015	36.454	-96.158	2650	0	6	0
Wf West End 2015	TX	2/13/2015	29.588	-94.341	6590	0	0	0
Razor Fire	PA	4/18/2015	40.779	-75.682	728	0	0	4
Boars Hammock	FL	4/26/2015	26.885	-81.253	790	0	0	0
Tallgrass East	KS	4/14/2015	38.41	-96.525	1745	0	0	0
Wf Texas Point Northeast	TX	10/4/2015	29.705	-93.93	4635	0	0	0
Greenwood	OK	3/23/2015	36.054	-96.319	5774	0	0	0
West Prong	OK	3/24/2015	36.413	-96.064	3676	0	1	500
Trail 12	FL	5/5/2015	28.788	-82.366	1041	0	0	0
Station	WY	10/11/2015	42.882	-106.18	9845	94	46	392
Big Spring Branch	WV	11/17/2015	37.701	-81.825	1044	0	0	0
Little Horse Creek	WV	11/17/2015	38.132	-81.851	1145	0	0	0
Little Jerrell	WV	11/18/2015	37.985	-81.646	1193	0	0	0
Trace Fork	WV	11/14/2015	37.434	-81.934	784	0	0	0
Kearny River	AZ	6/17/2015	33.068	-110.92	1543	5	5	50
Willow	AZ	8/8/2015	34.837	-114.544	6084	40	31	710
Goodell	WA	8/11/2015	48.683	-121.227	6624	0	0	50
Stouts Creek	OR	7/30/2015	42.859	-122.985	27570	0	0	645
Route Complex	CA	7/31/2015	40.601	-123.541	35444	0	2	475
Grenade	CA	4/29/2015	33.404	-117.514	1776	0	0	0
River Complex	CA	7/31/2015	40.914	-123.364	78531	0	0	506
Solimar	CA	12/26/2015	34.303	-119.342	1083	0	0	103
Cuesta	CA	8/17/2015	35.356	-120.612	2415	0	1	339
Parkhill	CA	6/20/2015	35.367	-120.424	1795	5	18	100
Tassajara	CA	9/19/2015	36.391	-121.589	1085	1	21	0

Lowell	CA	7/25/2015	39.212	-120.869	2633	1	3	1800
Tesla	CA	8/19/2015	37.636	-121.594	2508	0	1	0
Lumpkin	CA	9/11/2015	39.527	-121.327	1137	0	0	200
Wragg	CA	7/22/2015	38.481	-122.069	8455	5	2	700
Rocky	CA	7/29/2015	38.91	-122.45	96125	8	96	6959
Valley	CA	9/12/2015	38.788	-122.613	77507	95	2019	9150
Rough	CA	7/31/2015	36.852	-118.884	146369	0	4	1536
Washington	CA	6/19/2015	38.642	-119.699	18485	0	2	251
Butte	CA	9/9/2015	38.266	-120.592	72894	48	901	6400
Corrine	CA	6/19/2015	37.179	-119.5	1064	0	3	250
Willow	CA	7/25/2015	37.282	-119.479	5990	0	0	455
Cape Horn	ID	7/5/2015	47.998	-116.521	1505	1	14	309
Slide	ID	8/14/2015	46.096	-115.382	13509	0	0	29
I-90 Sprague	WA	8/1/2015	47.314	-117.934	1771	0	0	2
Carpenter Rd.	WA	8/15/2015	48.05	-118.091	62488	0	43	1005
Lawyer 2	ID	8/11/2015	46.23	-116.108	11378	0	0	25
Municipal	ID	8/15/2015	46.469	-116.19	1969	5	11	302
Woodrat	ID	8/11/2015	46.167	-115.771	6513	0	0	81
Tepee Springs	ID	8/12/2015	45.318	-116.116	94878	0	6	1410
Eagle	OR	8/11/2015	45.028	-117.373	14502	0	1	52
Canyon Creek Complex	OR	8/12/2015	44.301	-118.85	109786	100	54	722
Black Canyon	WA	8/14/2015	47.976	-120.053	61379	0	0	0
First Creek	WA	8/14/2015	47.929	-120.244	7971	22	19	556
Chelan Complex	WA	8/14/2015	47.912	-119.846	21774	1	55	2948
West Fork Fish Creek	MT	8/14/2015	46.909	-114.804	14495	0	5	372
North Star	WA	8/13/2015	48.415	-118.94	218547	0	1	4225
Marble Valley	WA	8/14/2015	48.404	-117.892	3431	22	41	326
Renner	WA	8/14/2015	48.758	-118.193	13975	0	0	120
Blue Creek	WA	7/20/2015	46.037	-118.08	5990	0	12	250
9 Mile	WA	8/13/2015	48.971	-119.296	5052	0	10	80
Limebelt	WA	8/14/2015	48.507	-119.694	137098	0	0	20
Hidden Pines	TX	10/13/2015	30.081	-97.183	3807	2	141	406
Tunk Block	WA	8/14/2015	48.478	-119.339	180111	0	145	3000
Liberty Hill	LA	10/13/2015	32.345	-92.907	711	0	3	12
Lake	CA	6/17/2015	34.147	-116.762	30421	0	4	7390
Sunland	WA	5/29/2016	47.045	-119.99	1940	0	0	20
16 Mile	PA	4/20/2016	41.199	-75.149	7896	9	11	287

Bear Town	PA	4/20/2016	41.181	-75.222	649	0	0	0
Sams Point Fire-Verkeerder Fire	NY	4/23/2016	41.681	-74.343	1929	0	0	7
Road 10	WA	8/2/2016	47.23	-119.357	2750	0	8	87
Elmer City	WA	9/11/2016	47.978	-118.942	5619	0	1	140
Rocky Mtn Fire 2016	VA	4/16/2016	38.31	-78.665	9299	0	0	337
Fifteen Mile	OR	7/1/2016	45.638	-121.006	4044	0	0	45
Range 12	WA	7/30/2016	46.495	-119.869	167604	0	0	250
County Line Road Fire	NC	3/10/2016	35.011	-79.513	1704	0	0	0
Mcbee Command	WA	7/15/2016	46.249	-119.519	1813	0	0	20
Cellar Mountain	VA	3/17/2016	37.93	-79.128	737	0	0	8
South Ward Gap	WA	7/31/2016	46.177	-119.825	4184	0	2	100
Kahlotus	WA	8/22/2016	46.645	-118.633	9386	0	4	30
Starbuck	WA	7/18/2016	46.527	-118.087	2414	0	0	0
Eades Hollow	VA	11/21/2016	37.775	-78.851	1564	0	0	17
Rattlesnake	OR	7/24/2016	44.835	-121.118	9296	0	0	41
Table Rock	ID	6/30/2016	43.591	-116.131	2481	1	2	100
Cottonwood Ca	SD	10/16/2016	43.905	-101.862	41775	0	2	0
Clifton	ID	8/23/2016	42.159	-112.01	2356	0	0	20
Henrys Creek	ID	8/21/2016	43.447	-111.765	52988	0	8	125
Salvage	ID	6/24/2016	42.8	-114.669	1847	1	0	11
Rock	NV	7/29/2016	39.871	-119.896	2387	0	0	800
Metz	CA	5/22/2016	36.387	-121.217	3826	0	0	5
Bug Creek	AZ	6/28/2016	34.294	-112.117	1184	0	0	105
Longview	AZ	6/6/2016	31.633	-110.548	1105	0	0	40
Ridge	AZ	5/25/2016	31.529	-110.338	1391	0	0	53
Crutch	TX	3/23/2016	35.615	-101.117	45052	0	4	0
Optima	OK	12/16/2016	36.692	-101.09	5084	0	0	0
Poplar	NC	3/31/2015	36.106	-82.337	768	0	0	3
Chestnut Knob	NC	11/6/2016	35.619	-81.657	6418	0	0	417
Horton	NC	11/22/2016	36.146	-81.568	1480	0	0	325
Bench Bluff	TN	11/12/2016	35.594	-85.242	1715	0	0	0
Pinnacle Mountain	SC	11/9/2016	35.055	-82.721	7869	0	1	1136
Rd 80	KS	3/17/2016	38.164	-96.391	63061	0	0	0
Bar-Dew Lake	OK	3/19/2016	36.828	-96.039	14806	0	0	62
Bear	OK	2/17/2016	36.309	-96.17	5966	0	0	80
Pawnee Cove	OK	2/18/2016	36.228	-96.411	3418	0	50	200

Pharoah	OK	2/18/2016	35.535	-96.097	13579	0	14	50
Sand Creek	OK	2/18/2016	35.3	-96.104	3839	0	0	170
Double Header	OK	3/6/2016	35.35	-96.083	1413	0	0	15
Katie	OK	3/6/2016	35.258	-96.099	1573	2	0	35
Mustang	OK	3/6/2016	36.669	-96.025	10060	0	0	82
Hall Horn	OK	3/16/2016	36.557	-96.298	5180	0	0	0
Walker	OK	3/19/2016	36.354	-96.235	2340	0	0	0
Varsity	OK	4/7/2016	35.728	-96.439	1216	0	0	55
Burmac	KS	3/23/2016	38.087	-97.668	10668	12	11	0
Burley Hill	KS	4/5/2016	39.016	-96.645	16381	1	0	0
Quinton Fire	OK	2/17/2016	35.14	-95.399	1219	0	0	5
Mason Fire	OK	2/19/2016	35.261	-95.473	1915	0	0	0
Round Prairie Road Fire	OK	2/19/2016	34.677	-95.173	2858	0	0	0
Cyclops	AL	11/5/2016	33.845	-87.033	660	0	0	4
Mount Pleasant	VA	11/19/2016	37.738	-79.178	11001	0	0	120
Gap	CA	8/27/2016	41.856	-123.036	33940	0	14	160
Willard	CA	9/11/2016	40.378	-120.749	2828	0	7	625
Kewa Fire	WA	8/2/2016	48.183	-118.284	1985	0	5	90
Cayuse Mtn	WA	8/22/2016	47.847	-118.038	9744	0	23	1535
Hart	WA	8/21/2016	47.822	-118.125	2819	20	40	605
Whit	WY	8/2/2016	44.409	-109.361	12731	0	8	165
Cliff Creek	WY	7/17/2016	43.296	-110.382	36131	0	1	135
Chimney	CA	6/1/2016	35.855	-118.025	1477	0	0	24
Erskine	CA	6/23/2016	35.569	-118.334	48066	75	286	2500
Cedar	CA	8/16/2016	35.791	-118.571	29191	0	12	2599
Slate	CA	10/4/2016	36.082	-118.556	2121	0	0	0
Meadow	CA	10/30/2016	35.975	-118.579	4346	0	0	0
Pioneer	ID	7/18/2016	44.139	-115.585	189596	0	6	465
Roaring Lion	MT	7/31/2016	46.177	-114.248	8096	3	66	2347
Spokane Complex	WA	8/22/2016	47.492	-117.289	6839	2	17	303
Sherpa	CA	6/15/2016	34.497	-120.033	7549	0	5	271
Rey	CA	8/18/2016	34.586	-119.725	33323	5	5	301
Pilot	CA	8/7/2016	34.308	-117.247	8267	0	0	5600
Blue Cut	CA	8/16/2016	34.324	-117.506	36856	8	321	611
Bogart	CA	8/30/2016	33.986	-116.933	1475	0	2	426
Fish	CA	6/20/2016	34.181	-117.939	4528	0	0	869
Deer	CA	7/1/2016	35.222	-118.688	1885	0	0	300

Sage	CA	7/9/2016	34.366	-118.574	1002	1	0	2500
Little Valley	NV	10/14/2016	39.266	-119.839	2964	0	40	200
Cold	CA	8/3/2016	38.536	-122.077	6289	0	2	52
Trailhead	CA	6/28/2016	38.963	-120.83	5743	0	0	2600
Soberanes	CA	7/22/2016	36.322	-121.701	132380	5	68	2010
Sand	CA	7/22/2016	34.391	-118.35	41561	6	20	10300
Clayton	CA	8/13/2016	38.915	-122.587	3792	29	302	1500
Loma	CA	9/26/2016	37.116	-121.818	4380	1	28	325
Border 3	CA	6/19/2016	32.611	-116.572	7958	3	17	1000
Mormon	AZ	5/15/2016	34.961	-111.573	7897	0	0	0
Goose	CA	7/30/2016	37.015	-119.466	2487	1	9	400
Tenderfoot	AZ	6/8/2016	34.232	-112.708	4363	0	3	300
Curry	CA	7/2/2016	36.087	-120.45	2837	0	0	25
Chimney	CA	8/13/2016	35.738	-121.075	46950	24	70	1898
Juniper	AZ	5/20/2016	33.864	-110.926	32293	1	0	141
Elk	AZ	7/21/2016	34.174	-109.864	1965	0	0	0
Beaver Creek	CO	6/19/2016	40.957	-106.505	44221	0	17	131
Fulton	AZ	9/12/2016	34.281	-110.89	3237	0	0	296
Beulah Hill	CO	10/3/2016	38.07	-104.928	5769	0	14	750
Junkins	CO	10/17/2016	38.14	-105.136	19023	0	26	745
Topock	AZ	4/6/2016	34.74	-114.51	1422	1	0	12
I40	TX	3/23/2016	35.244	-100.355	14780	0	14	200
350 Complex	OK	4/5/2016	36.647	-99.266	58055	0	0	825
Anderson Creek Fire	OK	3/23/2016	37.107	-98.835	374523	0	54	10000
Big Creek	MO	2/13/2016	36.634	-92.83	4031	0	0	0
Bob White	WV	4/3/2016	37.957	-81.7	824	0	0	10
Upper Conley Hollow	WV	4/4/2016	37.889	-82.095	1438	0	0	0
Jimmie Creek Rd	KY	10/26/2016	37.373	-82.386	500	0	0	0
Raven Rock	VA	11/2/2016	37.172	-82.61	2273	1	2	104
Bridge Creek Road	TN	10/30/2016	35.241	-85.559	1777	0	0	0
Spruce Pine Rd St Rt 7	KY	4/13/2016	37.522	-82.894	786	0	0	0
Little Shepherd Trail	KY	10/26/2016	36.951	-83.113	6751	0	0	0
Big Branch	KY	11/17/2016	37.062	-82.956	762	0	0	0
Poe Road	TN	11/11/2016	35.261	-85.254	758	0	0	0
Mowbray	TN	11/9/2016	35.286	-85.208	721	0	0	50
Bolts Br.	KY	11/24/2016	37.087	-83.656	1069	0	0	0
Lake Chinnabee	AL	11/28/2016	33.473	-85.871	1254	2	0	35

Caney Head	AL	3/20/2016	33.391	-85.843	957	0	0	0
Halls Top	TN	4/4/2016	35.875	-83.142	2464	1	1	71
Eagles Nest	KY	11/2/2016	37.53	-83.392	2857	0	0	50
Jetts Creek Fire	KY	11/6/2016	37.508	-83.563	3021	0	0	0
Bowlings Creek	KY	11/21/2016	37.361	-83.43	1023	0	0	0
Moore Peach	VA	4/10/2016	36.625	-82.986	1345	0	0	0
Sr116	TN	11/3/2016	36.169	-84.318	2222	0	0	0
Charles Branch Lane	TN	11/8/2016	36.204	-84.345	1071	0	0	0
Timber Ridge	GA	11/12/2016	34.828	-83.363	1002	0	0	400
Neddy Mountain Road	TN	11/11/2016	35.948	-83.072	788	0	0	150
Silver Mine	NC	4/21/2016	35.908	-82.791	6082	0	0	15
Party Rock	NC	11/5/2016	35.472	-82.241	8572	0	3	1050
State Line	TN	4/16/2016	35.926	-82.922	1111	0	0	17
Sr116-Devonia	TN	11/4/2016	36.116	-84.41	3077	0	0	0
Tellico	NC	11/3/2016	35.299	-83.589	14172	0	1	336
Maple Springs	NC	11/4/2016	35.392	-83.932	7696	1	0	29
Dick's Creek	NC	10/23/2016	35.399	-83.249	833	0	0	31
Dobson 3	NC	11/8/2016	35.506	-83.244	741	0	0	50
Hwy 190	KY	11/2/2016	36.74	-83.724	957	0	0	0
Railroad Grade 2016	TN	4/18/2016	36.227	-82.113	1790	0	0	25
Kentucky Ridge	KY	11/7/2016	36.686	-83.858	1133	0	0	0
Old Roughy	NC	11/9/2016	35.371	-83.85	534	0	0	44
East Miller Cove	TN	11/17/2016	35.744	-83.799	1331	0	0	100
Quarry Creek	TN	11/16/2016	35.349	-84.281	643	0	0	9
Cobbly Nob	TN	11/28/2016	35.779	-83.342	732	23	108	0
Stinking Creek	TN	11/9/2016	36.453	-84.199	10768	0	0	0
Boteler	NC	10/25/2016	35.068	-83.673	8626	0	0	314
Knob	NC	11/2/2016	35.114	-83.537	1132	0	0	0
Camp Branch	NC	11/23/2016	35.179	-83.558	3234	0	2	140
Wild Goose	LA	2/9/2016	31.406	-92.898	1260	0	3	20
Chimney Tops 2	TN	11/23/2016	35.687	-83.503	14998	257	2066	2800
Knox Bell Line	KY	10/29/2016	36.907	-83.605	1272	0	0	0
Rock Mountain	GA	11/9/2016	34.99	-83.522	25224	0	0	250
North Peak	NC	3/23/2016	35.753	-81.986	680	0	0	2
Old 50	FL	9/27/2016	28.547	-80.906	804	0	0	1
Island	FL	5/5/2016	29.318	-81.767	527	0	0	0
Skibo	MN	5/6/2016	47.498	-92.044	763	0	0	110

Clear Creek	NC	11/20/2016	35.72	-82.113	3493	0	0	392
Tombstone	NC	3/8/2016	35.545	-81.725	1747	0	0	0
Chetco Bar	OR	7/12/2017	42.238	-124.049	194877	9	30	12483
Helena	CA	8/31/2017	40.775	-123.062	18709	8	141	5350
Canyon	CA	9/25/2017	33.861	-117.66	2740	6	0	1910
Canyon 2	CA	10/9/2017	33.823	-117.734	9102	58	26	5000
Minerva 5	CA	7/29/2017	39.903	-120.944	4545	0	0	395
Detwiler	CA	7/16/2017	37.55	-120.121	83297	21	131	1500
Gate	CA	5/20/2017	32.654	-116.829	2265	0	0	315
Railroad	CA	8/29/2017	37.441	-119.613	12765	0	19	511
Lilac 5	CA	12/7/2017	33.299	-117.203	4159	69	193	1500
Mission	CA	9/3/2017	37.236	-119.466	1006	8	9	250
Earthstone	NV	7/3/2017	39.591	-119.517	35299	0	1	131
Preacher	NV	7/24/2017	38.855	-119.588	5330	0	0	800
Prater	NV	8/6/2017	39.551	-119.669	1572	0	0	30
Long Valley	CA	7/11/2017	39.992	-119.92	80456	3	10	500
Winnemucca Ranch	NV	7/4/2017	39.756	-119.644	4153	0	5	300
Cold Springs	NV	7/14/2017	39.646	-119.938	1557	0	0	100
Opera	CA	4/30/2017	33.997	-117.301	1070	0	0	0
Cutter	NV	10/3/2017	38.829	-119.604	4065	0	0	150
Roadrunner	CA	7/30/2017	36.015	-118.933	2436	0	0	10
Pier	CA	8/29/2017	36.122	-118.708	36626	0	2	1360
Winter	CA	7/6/2017	38.526	-122.054	2485	0	0	63
Atlas	CA	10/9/2017	38.364	-122.237	51664	129	790	5000
Jones	OR	8/11/2017	44.004	-122.512	10260	0	1	5
Nuns	CA	10/9/2017	38.349	-122.503	56883	0	0	0
Hatchery	NV	7/4/2017	38.977	-114.091	1142	0	0	0
Creek	CA	12/5/2017	34.294	-118.352	15833	81	123	2500
East Fork	MT	8/27/2017	48.231	-109.576	21165	5	5	80
Rye	CA	12/5/2017	34.43	-118.635	4895	3	6	5460
Gibralter Ridge	MT	8/8/2017	48.86	-114.849	6299	0	1	145
Caribou	MT	8/11/2017	48.979	-115.351	28101	0	40	570
West Fork	MT	8/30/2017	48.519	-115.606	21154	0	0	709
Canyon Creek	WA	7/15/2017	48.271	-120.072	1232	0	2	85
East Saddle	WA	8/12/2017	46.782	-119.349	17318	2	2	40
Wall	CA	7/7/2017	39.463	-121.406	6488	12	91	5400
Cascade	CA	10/9/2017	39.359	-121.375	16155	0	200	1000

Cherokee	CA	10/9/2017	39.591	-121.585	8415	0	3	53
Tubbs	CA	10/9/2017	38.568	-122.68	36981	14	576	29192
Sulfur	CA	10/9/2017	38.992	-122.666	2591	70	205	1720
Oil Well	NV	7/17/2017	40.92	-115.725	7240	0	28	200
Redwood Valley Incident	CA	10/9/2017	39.339	-123.213	36545	0	90	100
Pocket	CA	10/9/2017	38.77	-122.883	18691	0	0	0
Palmer	CA	9/2/2017	33.991	-117.121	4148	1	0	150
Mecca Fire	OR	6/26/2017	44.781	-121.231	2515	0	0	23
Emerson 0638 Rn	OR	7/25/2017	44.69	-121.012	10683	0	1	25
Thomas	CA	12/4/2017	34.459	-119.303	281982	280	1063	18000
Nena Springs	OR	8/9/2017	44.974	-121.198	70074	4	10	199
Pilot Valley	NV	8/13/2017	41.106	-114.095	2578	2	6	157
Ana	OR	7/8/2017	43.009	-120.769	5801	2	4	55
Eagle Creek	OR	9/2/2017	45.618	-121.942	48816	0	9	5526
Sheep Gap	MT	8/29/2017	47.475	-115.046	24702	0	0	80
Silver Dollar	WA	7/2/2017	46.57	-119.779	30789	0	0	30
Horn Butte 0594 Rn	OR	7/21/2017	45.682	-120.069	9325	0	0	35
Glade 3	WA	7/30/2017	46.144	-120.054	10582	0	1	20
Morgan Creek	OR	8/3/2017	44.426	-117.235	2329	0	0	0
Martin Canyon	ID	7/23/2017	43.49	-114.168	4053	0	0	0
Lagoon	ID	7/26/2017	42.955	-114.438	1484	0	3	10
Mammoth Cave	ID	8/4/2017	43.155	-114.193	50391	0	3	50
Breeze	ID	6/26/2017	43.302	-115.87	1863	0	0	40
North Delphia	MT	7/14/2017	46.548	-108.278	3767	0	0	40
Sage Hills	MT	7/20/2017	45.763	-108.348	1197	0	0	100
Lincoln Beach	UT	6/23/2017	40.071	-111.842	2298	0	0	14
Mulberry	AZ	5/6/2017	31.901	-110.611	1846	0	4	20
Lizard	AZ	6/7/2017	31.986	-110.006	15791	0	0	108
Encino	AZ	6/21/2017	31.65	-110.648	1357	2	15	250
Cajete	NM	6/15/2017	35.809	-106.559	1433	0	0	233
Sawmill	AZ	4/23/2017	31.822	-110.687	47357	0	0	415
Alice Creek	MT	7/22/2017	47.142	-112.438	29971	0	4	240
Sunrise	MT	7/17/2017	47.07	-114.838	26896	0	0	382
Tarina	CA	6/30/2017	35.385	-118.793	1257	0	0	6
Lolo Peak	MT	7/15/2017	46.666	-114.242	62316	2	10	1962
Mendenhall	MT	8/26/2017	45.653	-110.18	1196	0	2	30
July	MT	7/3/2017	47.89	-108.575	11409	0	6	101

FIRST STREET FOUNDATION

Hondito	NM	5/15/2017	36.608	-106.02	6949	0	0	0
Hill	CA	6/26/2017	35.405	-120.481	1900	5	4	30
Wolf	SD	3/4/2017	43.998	-102.169	1797	0	0	45
Hodgeman County	KS	3/6/2017	38.143	-99.853	8518	9	8	0
South Wenas	WA	6/27/2017	46.72	-120.601	2956	0	0	175
Spartan	WA	6/26/2017	47.32	-120.155	8775	0	0	91
Sheep	WA	7/24/2017	46.758	-120.544	1564	0	0	0
Monument Hill	WA	8/17/2017	47.304	-119.718	6437	19	23	175
Meyers	MT	7/14/2017	45.989	-113.552	68711	0	1	344
Jolly Mountain	WA	8/11/2017	47.341	-120.978	38159	0	0	5624
Rattlesnake Hills	WA	7/6/2017	46.515	-120.432	3553	0	0	30
Perryton	TX	3/6/2017	35.99	-100.36	290211	0	11	200
Monitor	WA	11/1/2017	47.503	-120.4	1196	0	0	300
Brianhead	UT	6/17/2017	37.788	-112.693	74276	5	26	1526
Thirty Seven	CA	10/9/2017	38.155	-122.474	1773	4	0	80
303	TX	2/28/2017	33.401	-102.535	9601	0	0	0
Slinkard	CA	8/29/2017	38.659	-119.571	8814	0	0	510
Keystone	WY	7/3/2017	41.174	-106.281	2784	0	1	80
Tripp	TX	2/10/2017	34.448	-100.789	2573	0	0	4
Dumas Complex	TX	3/6/2017	35.357	-101.722	26155	0	0	150
Prison	TX	2/28/2017	34.522	-101.804	2420	4	13	1143
2018 North Sargent Wf	TX	10/16/2017	28.813	-95.62	3959	0	0	60
Oks - 283	OK	3/7/2017	36.689	-99.755	68558	0	0	300
Lefors East	TX	3/7/2017	35.365	-100.524	68701	0	0	0
Beaver Mountain	OK	1/31/2017	35.168	-95.339	4754	0	0	0
Powder Mill	OK	2/2/2017	34.964	-95.382	1551	0	0	47
Highlands	KS	3/7/2017	38.182	-97.919	7418	9	13	1100
Jupiter Hills	KS	3/4/2017	38.109	-97.848	1283	1	1	100
Legion Lake	SD	12/11/2017	43.669	-103.394	54868	0	3	203
Sugar Cove	NC	1/28/2017	35.75	-82.143	638	0	0	14
Turn Table Fire	SC	4/2/2017	33.312	-79.878	1868	0	0	0
Dobson Knob	NC	4/9/2017	35.812	-81.993	1720	0	0	45
Big Branch Fire	KY	4/9/2017	37.181	-83.054	651	0	0	32
Ne 212th St	FL	3/31/2017	29.469	-81.956	610	0	0	40
Sod Farm 2	FL	4/16/2017	28.913	-81.453	901	0	0	0
Lost Creek	OK	3/3/2017	35.403	-96.141	2420	0	0	25
Spocogee	OK	3/1/2017	36.071	-96.33	6318	0	0	45

FIRST STREET FOUNDATION

Gun Range	OK	3/21/2017	35.646	-96.063	1524	0	0	3
Cod Dr	FL	7/8/2017	28.767	-82.258	640	0	0	12
Conner	FL	3/26/2017	29.252	-81.918	676	0	0	10
310 West Of Como	MS	1/29/2017	34.518	-90.075	745	2	1	6
Cr630 E	FL	2/15/2017	27.782	-81.315	5096	0	142	0
Oks - Starbuck	OK	3/7/2017	37.081	-99.893	657299	0	0	1000
Bonita	NM	6/3/2017	36.58	-106.149	7754	0	0	65
Garfield Road	FL	3/22/2017	30.418	-82.022	721	14	21	3
West Mims	GA	4/6/2017	30.651	-82.294	166737	0	4	920
Apple	CA	6/9/2018	39.924	-122.349	2849	0	9	0
Creek	CA	6/24/2018	40.486	-122.518	1353	0	11	610
Middle Ridge	OK	3/21/2017	35.577	-94.626	8501	0	0	0
Persimmon Ridge	OK	3/21/2017	35.653	-95.088	5333	0	0	0
Sun	CA	10/7/2018	40.23	-122.143	3921	0	0	70
Lost Fire	OK	3/21/2017	34.708	-95.757	4178	0	2	4
Potato Hills	OK	3/23/2017	34.694	-95.226	2503	0	0	0
Montecito	WA	6/28/2018	46.175	-119.762	1877	0	0	50
Wagon Wheel	WA	9/1/2018	46.35	-119.513	4063	0	0	90
Milepost Twenty Two	WA	6/20/2018	46.966	-120.05	7406	0	0	16
Boffer	WA	8/11/2018	46.142	-119.141	4645	0	7	0
Conrad	WA	7/1/2018	46.739	-120.665	4611	0	1	220
Milepost 90	WA	8/1/2018	45.681	-120.937	10757	0	0	70
Lee Williams Rd	FL	3/5/2017	26.133	-81.637	7288	1	6	1000
South Valley Road	OR	8/1/2018	45.371	-121.161	20471	0	19	212
Jackson Ranch	OK	3/23/2017	35.797	-96.217	4243	0	0	40
Substation 0730 Rn	OR	7/17/2018	45.5	-120.939	69109	8	52	1363
Mile Marker 44	WA	9/1/2018	46.149	-120.529	4063	0	0	0
Boxcar 0410 Rn	OR	6/21/2018	45.022	-121.004	99874	0	0	55
Tenino Fire	OR	8/16/2018	44.708	-121.371	8821	0	0	0
Graham 0420 Od	OR	6/21/2018	44.55	-121.4	2102	0	11	204
Angel Springs	WA	8/2/2018	47.775	-118.029	4718	0	14	170
Eagle	CA	7/13/2018	41.268	-120.105	2116	0	0	18
Soap Lake	WA	6/11/2018	47.436	-119.49	2158	0	0	35
Chelan Hills	WA	7/27/2018	47.782	-119.962	1850	4	8	100
Rocky Reach	WA	7/13/2018	47.527	-120.327	3346	0	0	313
Boylston	WA	7/19/2018	46.85	-120.11	66292	1	6	1
Keithly	ID	7/25/2018	44.464	-116.843	17588	0	0	31

FIRST STREET FOUNDATION

Silver State	NV	7/14/2018	40.886	-115.665	3766	0	0	0
Rocky	NV	6/23/2018	40.378	-118.262	1641	1	1	10
Owyhee	NV	7/21/2018	41.948	-116.077	5347	0	0	60
South Sugarloaf	NV	8/17/2018	41.716	-116.019	241426	3	17	116
Goodwin	AZ	6/24/2017	34.381	-112.299	28192	3	33	1400
La Tuna	CA	9/1/2017	34.23	-118.316	7035	1	10	1376
Powerline	ID	8/4/2017	42.699	-112.605	54378	0	1	35
White Creek	NC	3/16/2017	35.837	-81.883	4166	0	0	7
Shoestring	ID	8/5/2017	42.878	-114.574	35543	0	1	2
Penn Swamp Fire	NJ	7/20/2017	39.677	-74.638	3587	0	0	0
Weogufkee	OK	3/20/2017	35.233	-95.904	2226	0	0	0
Holiday	FL	4/5/2017	26.003	-80.468	8858	0	0	20
30th Ave	FL	4/20/2017	26.177	-81.605	6463	18	14	3884
Powerline	WY	8/12/2018	44.461	-108.926	1837	0	0	0
Raintree Blvd	FL	5/13/2017	27.074	-82.052	3319	0	0	0
Flat Rock Fire	NY	7/12/2018	44.87	-73.637	658	0	0	2
Tye River	VA	5/3/2018	37.905	-79.154	1761	0	0	29
Spring Creek	CO	6/27/2018	37.543	-105.144	107108	119	225	2878
Blaine	CA	8/13/2017	33.984	-117.29	1117	46	0	441
Roosevelt	WY	9/15/2018	43.06	-110.387	55330	1	57	1153
8 Mile	ID	9/22/2018	42.595	-111.54	1001	0	5	95
Miles	OR	7/16/2018	42.828	-122.699	40343	0	2	1011
Ramsey Canyon	OR	8/22/2018	42.587	-122.992	2127	0	1	540
Natchez	CA	7/15/2018	41.895	-123.566	38800	0	0	104
Taylor Creek	OR	7/15/2018	42.488	-123.619	57505	0	0	3292
Klondike	OR	7/16/2018	42.418	-123.873	178311	0	0	1940
Ferguson	CA	7/13/2018	37.635	-119.807	97307	0	11	5236
Kerlin	CA	9/4/2018	40.625	-123.512	1775	0	5	100
Hirz	CA	8/9/2018	40.984	-122.279	46700	0	1	171
Delta	CA	9/5/2018	41.007	-122.462	63732	7	45	330
River	CA	7/27/2018	39.055	-123.019	48920	0	2	305
County	CA	6/30/2018	38.683	-122.155	92450	4	31	1516
Nelson	CA	8/10/2018	38.312	-121.999	2205	1	1	260
Whaleback	CA	7/27/2018	40.627	-120.824	18640	0	0	460
Hat	CA	8/9/2018	40.998	-121.489	1971	0	0	380
Boyds	WA	8/11/2018	48.632	-118.154	5196	0	10	529
Crescent Mountain	WA	7/29/2018	48.384	-120.446	53258	0	0	1196

FIRST STREET FOUNDATION

Camp	CA	11/8/2018	39.748	-121.565	153687	751	18838	17500
Stone	CA	8/15/2018	41.425	-121.013	39455	0	2	119
Chaves	NV	6/3/2018	39.3	-119.412	3652	1	0	98
Upper Colony	NV	6/17/2018	38.812	-119.411	1255	0	0	92
Donnell	CA	8/1/2018	38.383	-119.822	36151	0	136	305
Rattlesnake Creek	ID	7/23/2018	45.232	-116.376	8461	0	0	618
Rabbit Foot	ID	8/2/2018	44.848	-114.23	33787	0	0	1446
Pinery	AZ	5/12/2018	31.982	-109.353	1474	0	0	25
Viewpoint	AZ	5/11/2018	34.693	-112.343	5389	14	0	0
Tinder	AZ	4/27/2018	34.59	-111.11	16083	0	96	1700
Hub Point	AZ	7/27/2018	34.251	-110.29	4674	0	0	0
Soldier Canyon	NM	6/7/2018	33.185	-105.759	1386	0	0	100
Pierson	NM	4/17/2018	32.499	-103.418	1060	0	0	2
Ute Park	NM	5/31/2018	36.533	-105.028	30177	3	15	2952
Valley	CA	7/6/2018	34.105	-116.946	1250	0	0	500
Harbor Bay	TX	4/13/2018	35.619	-101.631	1428	0	8	50
Cranston	CA	7/25/2018	33.715	-116.705	13096	6	12	6230
Holy	CA	8/6/2018	33.704	-117.468	22845	18	24	13300
Stone	CA	6/4/2018	34.55	-118.292	1659	0	0	150
Badger Hole	CO	4/17/2018	37.433	-102.088	49146	1	24	0
Charlie	CA	9/22/2018	34.521	-118.559	3367	0	0	100
Cr 26	TX	4/14/2018	35.256	-100.084	1386	0	0	6
Milliron	TX	4/13/2018	34.913	-100.011	20437	0	21	75
34 Complex	OK	4/12/2018	36.585	-99.352	57533	0	55	150
Hill	CA	11/8/2018	34.207	-118.953	4427	2	4	437
Front	CA	8/19/2018	35.119	-120.097	1126	0	0	5
Perry	NV	7/27/2018	39.802	-119.496	53734	3	16	418
Airline	CA	6/4/2018	36.391	-120.962	1477	0	0	1
Lake Christine	CO	7/3/2018	39.419	-107.037	12506	9	6	1329
Chateau	CO	6/29/2018	38.815	-105.3	1414	0	8	754
Carson Midway	CO	3/16/2018	38.527	-104.716	4773	0	2	0
Rhea	OK	4/12/2018	36.003	-99.003	277949	0	50	3500
Organ	NM	6/24/2018	32.454	-106.527	4880	0	0	1
Harman Road	TX	7/18/2018	31.333	-97.972	3094	0	1	115
Owl Creek	NV	8/30/2018	40.658	-115.526	1165	0	0	12
Lime Rock Rd (19)	FL	6/24/2018	29.765	-84.866	1190	4	36	400
Cougar Creek	WA	7/28/2018	47.816	-120.478	42681	0	0	3000

FIRST STREET FOUNDATION

Rozell	MO	2/15/2018	36.587	-92.862	1970	0	6	0
Bald Mountain	UT	8/24/2018	39.925	-111.693	21016	0	1	2600
Pole Creek	UT	9/6/2018	39.982	-111.53	102426	0	1	2626
Hill Top	UT	8/6/2018	39.737	-111.441	1784	2	4	320
Dollar Ridge	UT	7/1/2018	40.111	-110.877	69817	6	453	1023
Little Shepherds Trail	KY	5/1/2018	36.976	-83.034	541	0	0	0
Keepers Branch Fire	SC	3/4/2018	33.189	-79.542	819	0	0	6
Range Two	NV	9/30/2018	40.669	-115.448	9361	0	8	60
Dog Head	NM	6/14/2016	34.851	-106.3	19816	0	73	1950
Ranch	CA	7/27/2018	39.269	-122.775	427048	0	0	86
416	CO	6/1/2018	37.493	-107.903	55123	0	0	3386
Grass Valley	WA	8/11/2018	47.94	-119.166	76074	1	20	330
West 60	OK	3/7/2018	36.789	-96.487	18715	0	0	10
Carr	CA	7/23/2018	40.715	-122.593	233710	282	1608	5013
Badger Creek	WY	6/10/2018	41.055	-106.11	20752	4	3	553
Tomahawk	AR	4/12/2018	36.056	-92.671	533	0	8	15
Woolsey	CA	11/8/2018	34.125	-118.824	97962	365	1643	57000
Flag Pond (11)	FL	3/21/2018	26.139	-81.595	2562	0	0	0
Buffalo Corral	AZ	7/14/2019	31.573	-110.377	1144	0	0	0
Kincade	CA	10/23/2019	38.672	-122.776	77785	60	375	90015
Easy	CA	10/30/2019	34.267	-118.829	2105	1	1	2635
Sandalwood	CA	10/10/2019	33.999	-117.084	1048	16	76	0
Tick	CA	10/24/2019	34.451	-118.394	4932	48	31	10425
Maria	CA	11/1/2019	34.314	-119.066	10036	0	5	2722
Saddleridge	CA	10/10/2019	34.318	-118.515	9656	93	38	25760
Black Bridge	CO	4/4/2019	38.074	-103.177	1690	0	0	7
116th Ave Se (11)	FL	3/21/2018	26.034	-81.56	29262	0	3	0
335	TX	4/13/2018	32.676	-99.716	2481	0	15	100
Blue Creek #2	OK	3/14/2018	35.052	-95.594	2578	0	0	0
Deerte	OK	3/15/2018	35.367	-95.871	1833	0	0	8
Henry	OK	3/20/2018	35.581	-96.42	1160	0	0	17
Brewster	OK	3/16/2018	35.685	-96.299	4049	0	0	20
Flying G	OK	3/12/2018	36.124	-96.203	1886	0	0	184
Walker	OK	3/24/2018	36.35	-96.233	2626	0	0	9
Drumb	OK	3/24/2018	36.467	-96.3	30419	0	0	9
Onion Prairie	OK	3/6/2018	36.641	-96.017	3911	0	0	20
New Years Wf	TX	1/1/2018	29.706	-93.908	5613	0	0	12

FIRST STREET FOUNDATION

Farmers Road	TX	1/22/2018	32.738	-97.596	2379	0	0	252
Carbon	TX	4/13/2018	35.214	-100.068	12148	0	0	500
Pemberton	AZ	8/6/2019	34.731	-112.676	1211	0	0	0
Green Ravine	UT	9/3/2019	40.683	-112.228	2260	0	0	3
Goose Point	UT	8/21/2019	40.076	-111.832	9190	0	0	23
Dove	AZ	5/24/2019	33.799	-112.429	1078	0	0	10
White Wing	AZ	5/30/2019	33.796	-112.437	1797	0	0	30
Tenaja	CA	9/4/2019	33.549	-117.258	1820	2	0	1200
Walker	CA	9/4/2019	40.09	-120.585	58752	0	9	78
Long Valley	CA	8/24/2019	39.882	-119.995	2451	4	1	80
Briceburg	CA	10/6/2019	37.608	-119.932	5555	0	1	160
Woodbury	AZ	6/8/2019	33.52	-111.175	130243	0	0	1537
Stuckey Rd Ma	MT	9/2/2019	47.586	-111.357	4077	0	9	0
Matson	WA	10/7/2019	46.619	-118.93	8715	0	0	86
Sand	CA	6/8/2019	38.904	-122.259	2473	0	7	125
Museum	AZ	7/21/2019	35.263	-111.62	2011	0	0	0
Elmer City	WA	6/23/2019	48.064	-118.943	1996	2	2	45
Desert Canyon	WA	7/23/2019	47.711	-120.148	1505	0	0	16
243 Command	WA	6/4/2019	46.855	-119.785	18891	1	2	36
Cut Across	MT	4/7/2019	45.63	-106.7	1858	0	0	130
Boulder	CA	6/5/2019	35.32	-119.93	1199	0	0	0
Decker	CO	9/8/2019	38.441	-105.995	9876	0	4	142
Boulin	AZ	8/6/2019	35.382	-112.036	4094	0	0	12
Coldwater	AZ	5/30/2019	34.481	-111.335	16824	0	0	14
Cave	CA	11/25/2019	34.489	-119.768	2761	1	0	15000
Left Hand	WA	7/23/2019	46.915	-120.975	3234	0	0	347
North Hills	MT	7/26/2019	46.765	-111.944	4144	0	0	600
Tx Point East Christmas Eve	TX	12/24/2019	29.716	-93.9	1163	0	0	43
Williams Flats	WA	8/2/2019	47.977	-118.498	44680	0	3	56
Pedro Mountain	WY	8/24/2019	42.337	-106.826	21910	0	8	90
Cove Creek	ID	8/4/2019	45.346	-114.465	5273	0	0	39
Channing	TX	2/16/2019	35.663	-102.275	7855	0	0	20
Burnside	OK	3/19/2019	34.593	-97.029	1117	0	0	10
East Kennedy Creek	KS	4/2/2019	38.29	-95.815	1003	0	0	0
Clark Branch #2	KY	9/17/2019	37.603	-82.621	1315	0	0	0
344 D	FL	9/11/2019	30.356	-84.632	2339	0	0	0

Cr 2297 Allenton (03)	FL	3/30/2019	30.115	-85.482	725	0	0	52
Dry Hollow	WV	11/28/2019	38.831	-79.308	1412	0	0	16
Kennedy Peak	VA	11/14/2019	38.762	-78.466	769	0	0	0
Spring Hill Fire	NJ	3/30/2019	39.79	-74.451	8182	0	0	0

FIRST STREET FOUNDATION

Appendix B. Pyrome-specific validation/calibration

The results from the FSF-WFM were compared to the historical records in the FOD with respect to fire number and size. To reduce the effect of small fires on comparisons between FSF-WFM results and those from the FOD, as well as to reduce the impact of variability in the FOD's historical record, the FSF-WFM and FOD records burn probabilities were smoothed spatially before comparisons. Additionally, a "soft cap" on the FSF-WFM maximum burn probability was applied to accommodate possible overestimation from the Monte Carlo simulation's systematic reburning of the most vulnerable areas while neglecting the impact on annual probabilities due to fuel changes from previously burned areas.

Fire size-divergence metric

A divergence metric was first created to allow the quantitative comparison of probability distributions with the observed data from the FOD. While we can measure this divergence for v1 and v2 of the FSF-WFM results and this evidence suggests that the correlation with the FOD is better with v2 than it was with v1 for the majority of pyromes (see Figure B1), some are not so clearly defined. We will continue to research this comparison and validation method so that it can be applied to future versions of the FSF-WFM to continue to measure our progress.

The logic of this divergence metric is the following. If our models emitted a probability density function **p(fire size, pyrome)**, then established statistical methods would readily give us an appropriate metric of divergence from the historical record: *deviance* (-2 times the log-likelihood). There are 2 problems preventing us from simply applying this method directly, which are addressed by 2 adaptations:

1. Problem: our models produce samples, not PDFs.
    a. Solution: we apply a density estimation algorithm to the samples.
2. Problem: this deviance metric would give huge importance to the numerous but small fires, which we know should be considered relatively inconsequential with respect to overall fire risk.
    a. Solution: we transform the underlying probability distributions so that they are weighted not by number of fires, but by burned acres. The meaning of probability thus changes as follows:
        i. Before: *if I pick a fire at random, what is its size and pyrome of origin?*
        ii. After: *if I pick a **burned acre** at random, what is the size and pyrome of origin of the fire that burned it?*

The comparison results for each pyrome are shown in Figure B2 for those pyromes with a sufficient number of simulated fires to conduct this analysis. The analysis is shown for all fires, fires

of size greater than 10ac, and of size greater than 100ac. The location of each pyrome is depicted in Figure B3.

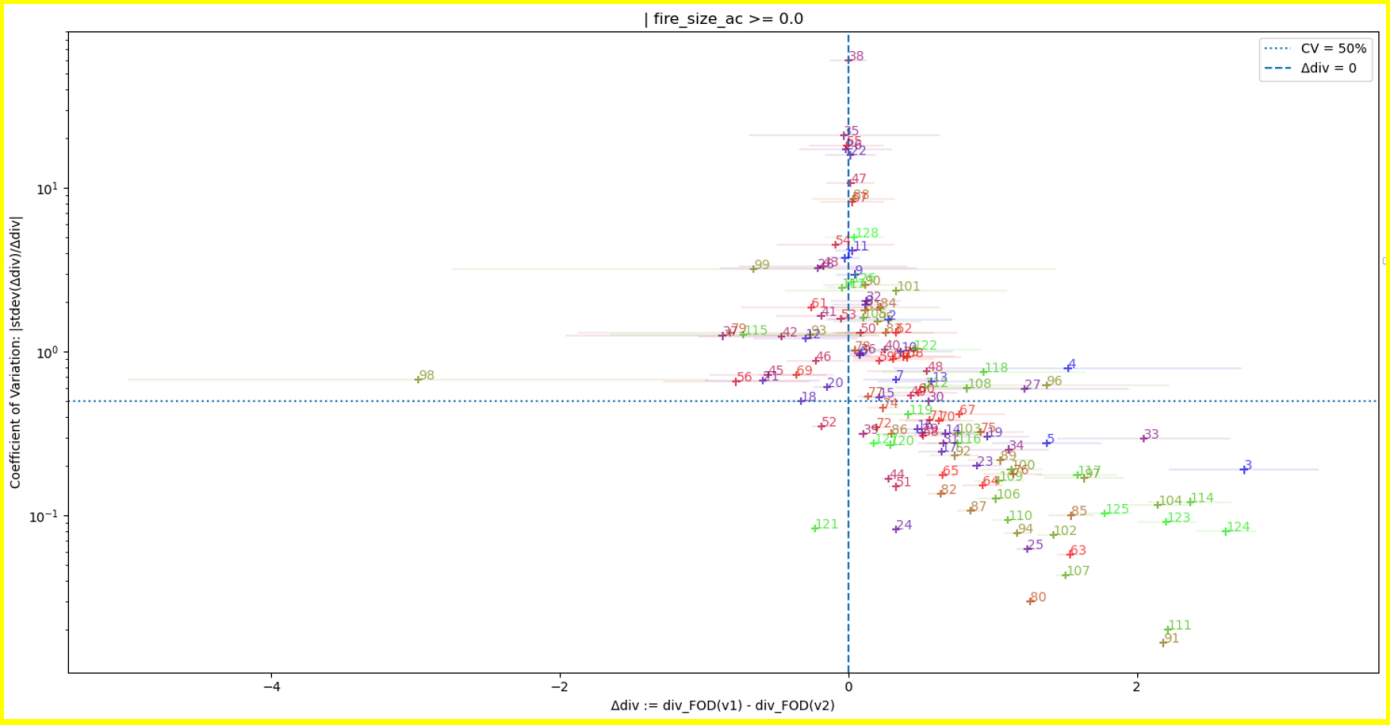

Figure B1. The FSF-WFM V1-V2 divergence difference for each pyrome (for the curves seen in Figure B2) is presented as a function of pyrome (colored number). Pyromes to the right of the dashed line exhibit better goodness-of-fit for V2 than V1, while above the dotted line the comparison is considered uncertain since it is highly sensitive to FOD variability. Horizontal segments are 2 standard-deviations wide under resampling of FOD years.

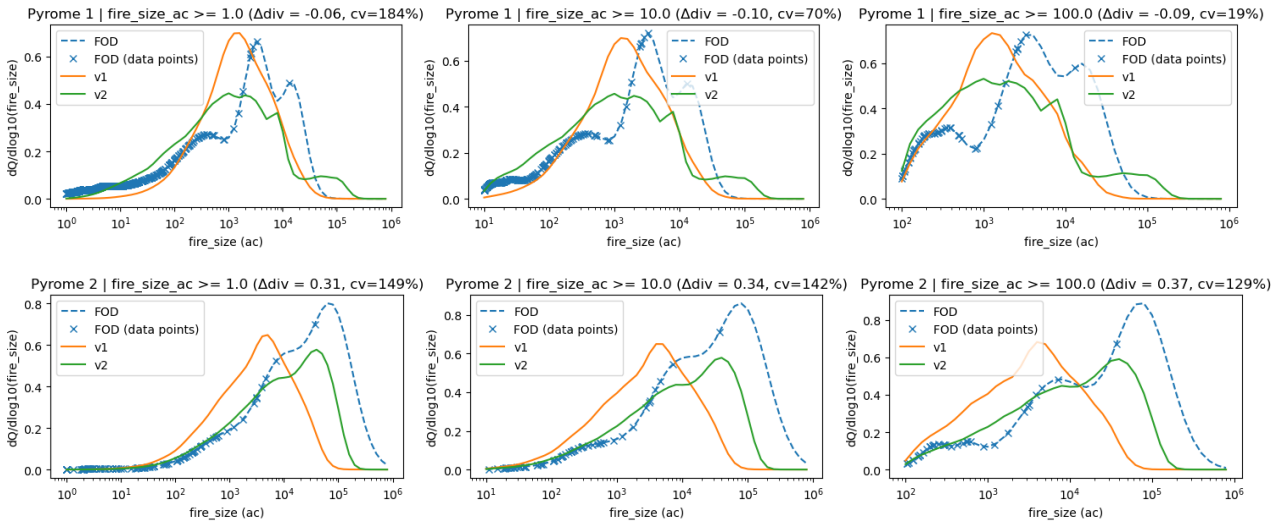

Size-weighted probability densities of fire size.
WARNING: the density estimation for the FOD curve can be poor due at the right tail, due to lack of data. That is not a problem for computing Δdiv).

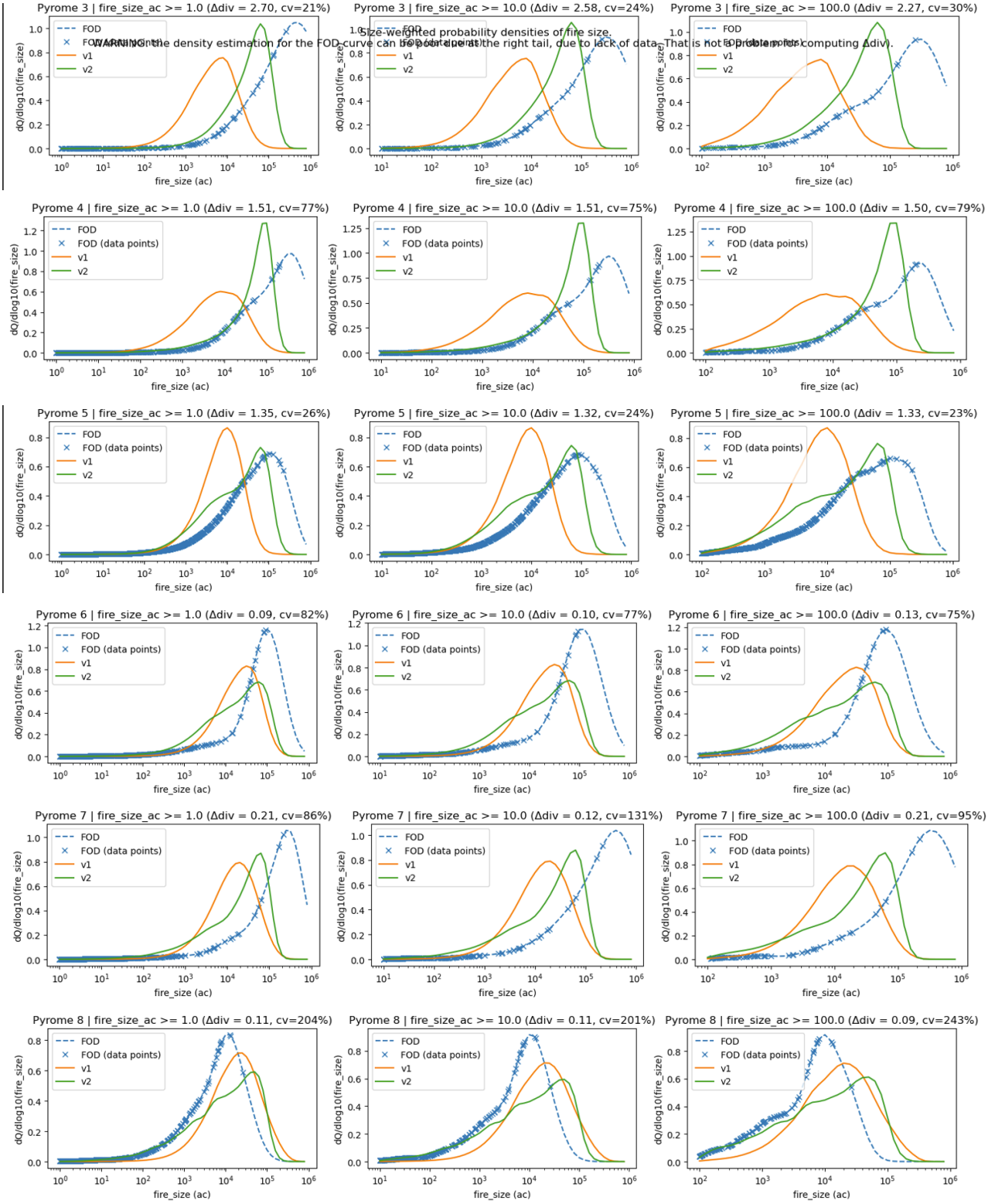

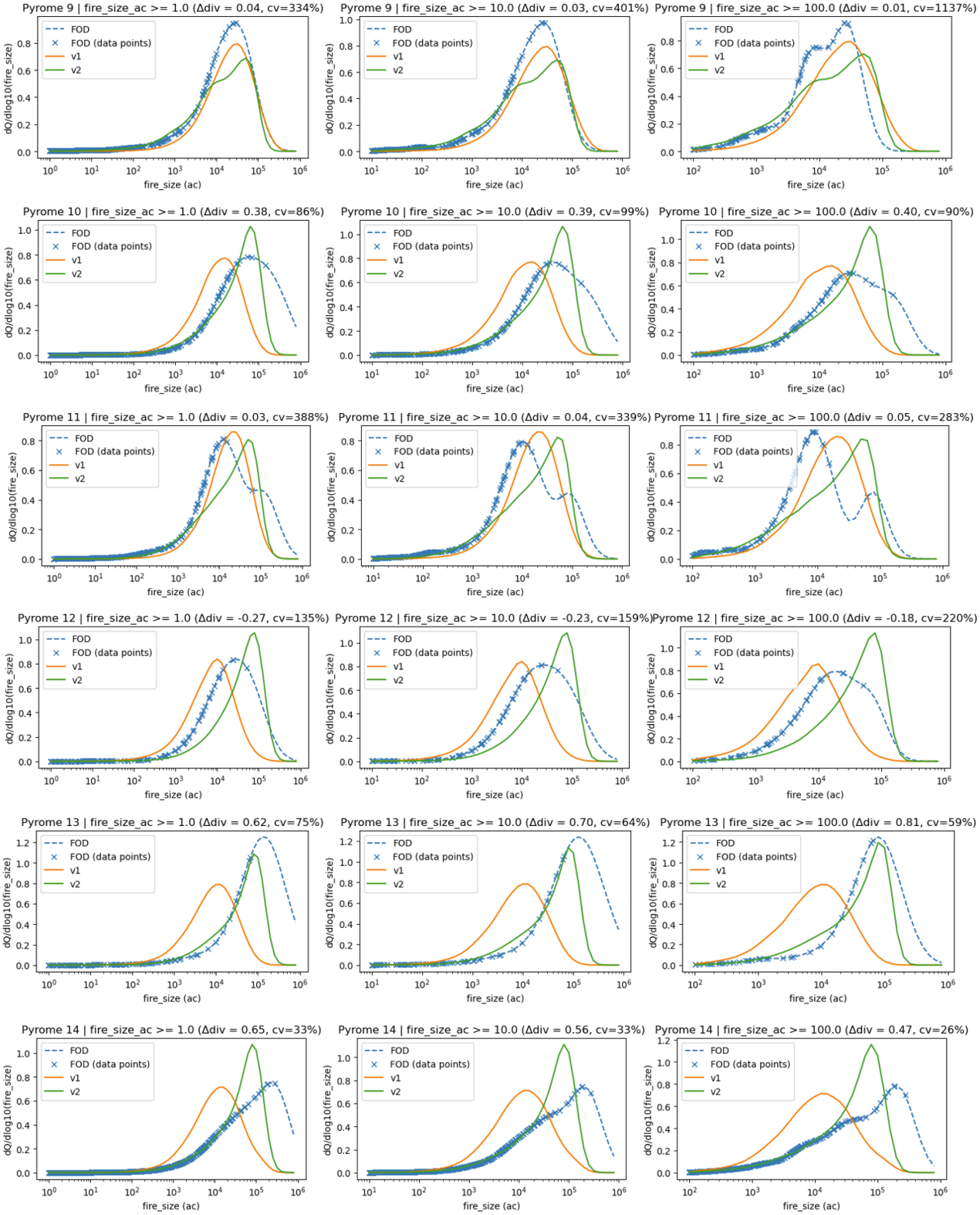
Pyrome 9 | fire_size_ac >= 1.0 (Δdiv = 0.04, cv=334%)
Pyrome 9 | fire_size_ac >= 10.0 (Δdiv = 0.03, cv=401%)
Pyrome 9 | fire_size_ac >= 100.0 (Δdiv = 0.01, cv=1137%)
Pyrome 10 | fire_size_ac >= 1.0 (Δdiv = 0.38, cv=86%)
Pyrome 10 | fire_size_ac >= 10.0 (Δdiv = 0.39, cv=99%)
Pyrome 10 | fire_size_ac >= 100.0 (Δdiv = 0.40, cv=90%)
Pyrome 11 | fire_size_ac >= 1.0 (Δdiv = 0.03, cv=388%)
Pyrome 11 | fire_size_ac >= 10.0 (Δdiv = 0.04, cv=339%)
Pyrome 11 | fire_size_ac >= 100.0 (Δdiv = 0.05, cv=283%)
Pyrome 12 | fire_size_ac >= 1.0 (Δdiv = -0.27, cv=135%)
Pyrome 12 | fire_size_ac >= 10.0 (Δdiv = -0.23, cv=159%)
Pyrome 12 | fire_size_ac >= 100.0 (Δdiv = -0.18, cv=220%)
Pyrome 13 | fire_size_ac >= 1.0 (Δdiv = 0.62, cv=75%)
Pyrome 13 | fire_size_ac >= 10.0 (Δdiv = 0.70, cv=64%)
Pyrome 13 | fire_size_ac >= 100.0 (Δdiv = 0.81, cv=59%)
Pyrome 14 | fire_size_ac >= 1.0 (Δdiv = 0.65, cv=33%)
Pyrome 14 | fire_size_ac >= 10.0 (Δdiv = 0.56, cv=33%)
Pyrome 14 | fire_size_ac >= 100.0 (Δdiv = 0.47, cv=26%)
FOD
FOD (data points)
v1
v2
dQ/dlog10(fire_size)
fire_size (ac)

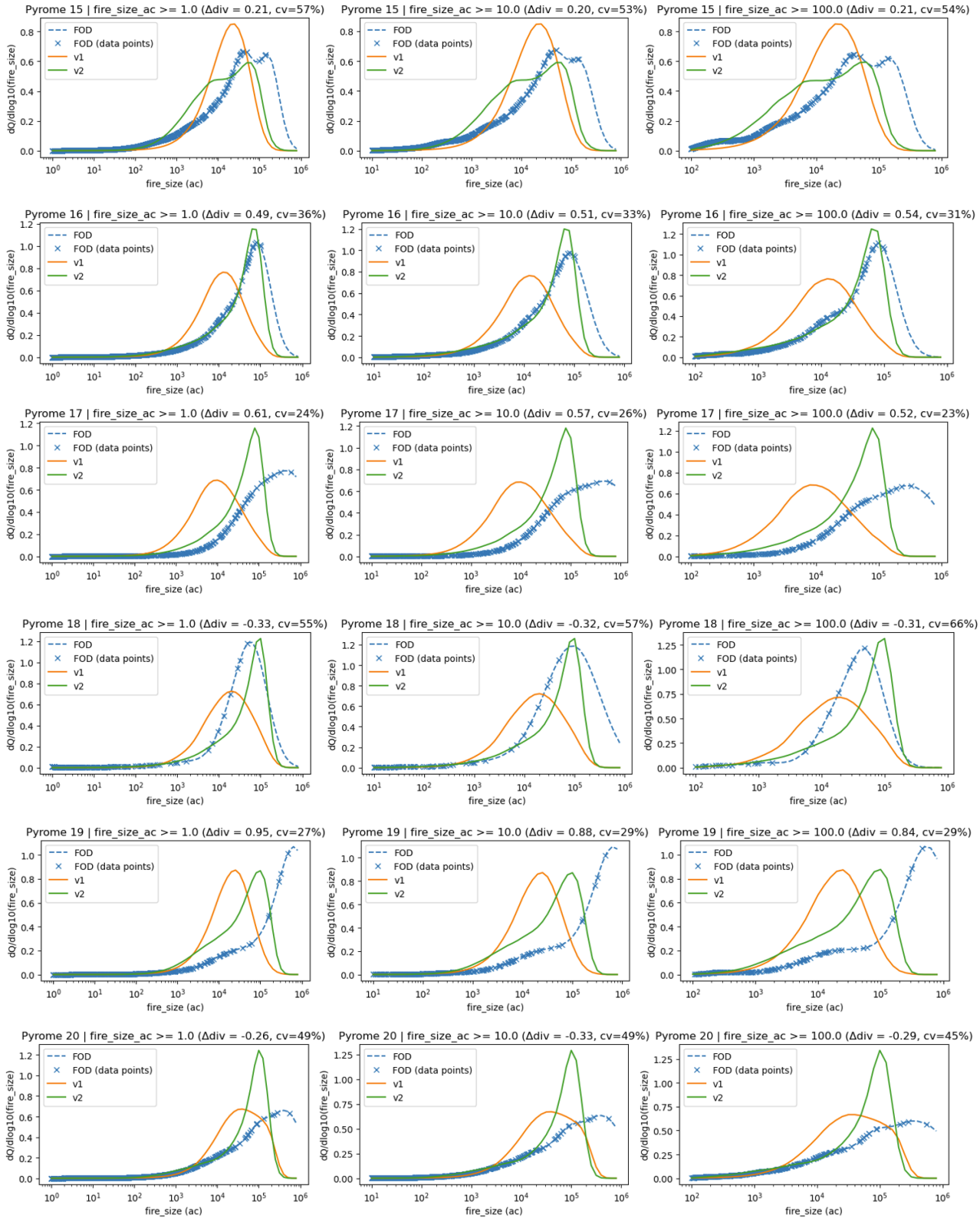
Pyrome 15 | fire_size_ac >= 1.0 (Δdiv = 0.21, cv=57%)
Pyrome 15 | fire_size_ac >= 10.0 (Δdiv = 0.20, cv=53%)
Pyrome 15 | fire_size_ac >= 100.0 (Δdiv = 0.21, cv=54%)
Pyrome 16 | fire_size_ac >= 1.0 (Δdiv = 0.49, cv=36%)
Pyrome 16 | fire_size_ac >= 10.0 (Δdiv = 0.51, cv=33%)
Pyrome 16 | fire_size_ac >= 100.0 (Δdiv = 0.54, cv=31%)
Pyrome 17 | fire_size_ac >= 1.0 (Δdiv = 0.61, cv=24%)
Pyrome 17 | fire_size_ac >= 10.0 (Δdiv = 0.57, cv=26%)
Pyrome 17 | fire_size_ac >= 100.0 (Δdiv = 0.52, cv=23%)
Pyrome 18 | fire_size_ac >= 1.0 (Δdiv = -0.33, cv=55%)
Pyrome 18 | fire_size_ac >= 10.0 (Δdiv = -0.32, cv=57%)
Pyrome 18 | fire_size_ac >= 100.0 (Δdiv = -0.31, cv=66%)
Pyrome 19 | fire_size_ac >= 1.0 (Δdiv = 0.95, cv=27%)
Pyrome 19 | fire_size_ac >= 10.0 (Δdiv = 0.88, cv=29%)
Pyrome 19 | fire_size_ac >= 100.0 (Δdiv = 0.84, cv=29%)
Pyrome 20 | fire_size_ac >= 1.0 (Δdiv = -0.26, cv=49%)
Pyrome 20 | fire_size_ac >= 10.0 (Δdiv = -0.33, cv=49%)
Pyrome 20 | fire_size_ac >= 100.0 (Δdiv = -0.29, cv=45%)
FOD
FOD (data points)
v1
v2
dQ/dlog10(fire_size)
fire_size (ac)

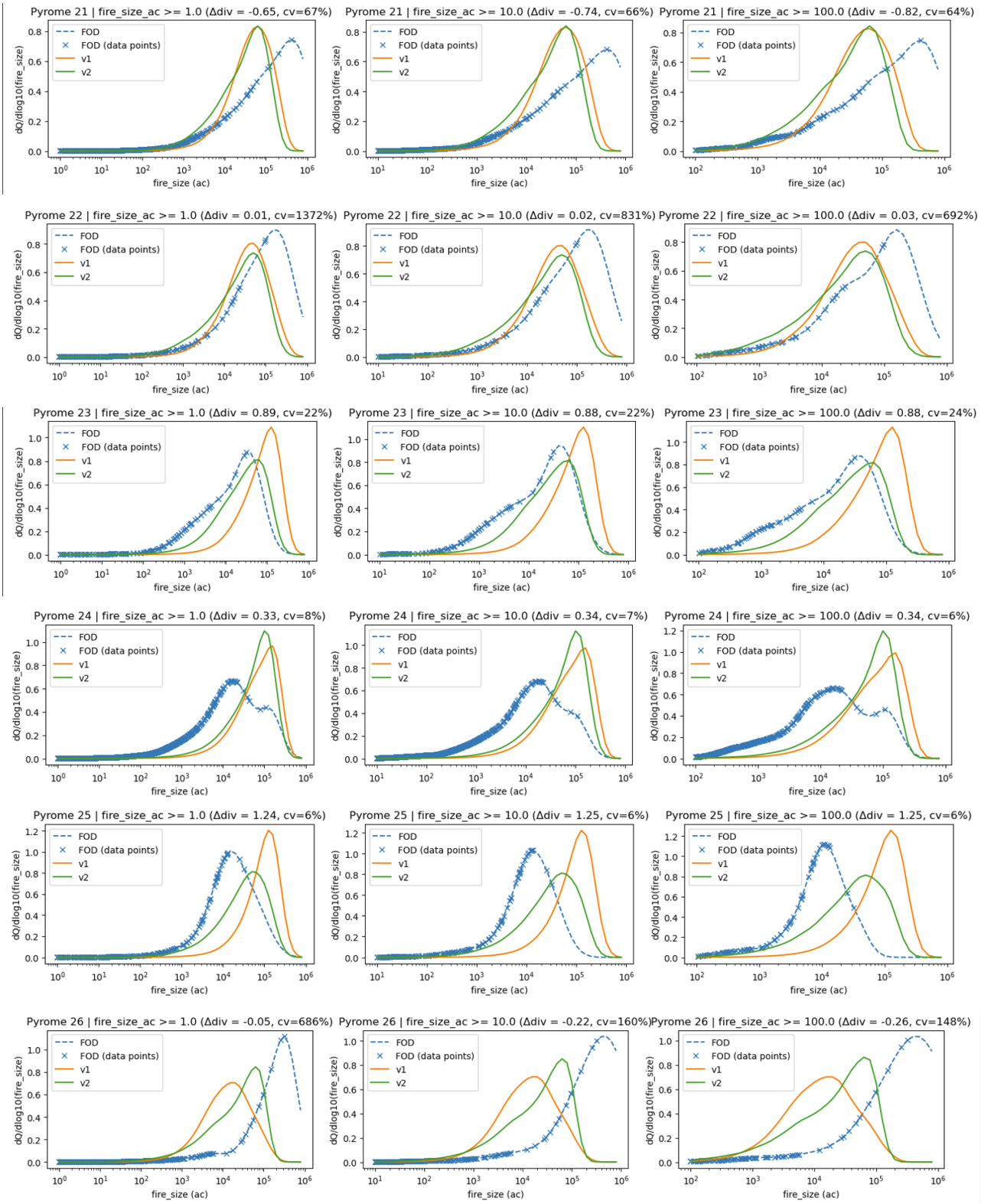
Pyrome 21 | fire_size_ac >= 1.0 (Δdiv = -0.65, cv=67%)
Pyrome 21 | fire_size_ac >= 10.0 (Δdiv = -0.74, cv=66%)
Pyrome 21 | fire_size_ac >= 100.0 (Δdiv = -0.82, cv=64%)
Pyrome 22 | fire_size_ac >= 1.0 (Δdiv = 0.01, cv=1372%)
Pyrome 22 | fire_size_ac >= 10.0 (Δdiv = 0.02, cv=831%)
Pyrome 22 | fire_size_ac >= 100.0 (Δdiv = 0.03, cv=692%)
Pyrome 23 | fire_size_ac >= 1.0 (Δdiv = 0.89, cv=22%)
Pyrome 23 | fire_size_ac >= 10.0 (Δdiv = 0.88, cv=22%)
Pyrome 23 | fire_size_ac >= 100.0 (Δdiv = 0.88, cv=24%)
Pyrome 24 | fire_size_ac >= 1.0 (Δdiv = 0.33, cv=8%)
Pyrome 24 | fire_size_ac >= 10.0 (Δdiv = 0.34, cv=7%)
Pyrome 24 | fire_size_ac >= 100.0 (Δdiv = 0.34, cv=6%)
Pyrome 25 | fire_size_ac >= 1.0 (Δdiv = 1.24, cv=6%)
Pyrome 25 | fire_size_ac >= 10.0 (Δdiv = 1.25, cv=6%)
Pyrome 25 | fire_size_ac >= 100.0 (Δdiv = 1.25, cv=6%)
Pyrome 26 | fire_size_ac >= 1.0 (Δdiv = -0.05, cv=686%)
Pyrome 26 | fire_size_ac >= 10.0 (Δdiv = -0.22, cv=160%)
Pyrome 26 | fire_size_ac >= 100.0 (Δdiv = -0.26, cv=148%)
FOD
FOD (data points)
v1
v2
dQ/dlog10(fire_size)
fire_size (ac)

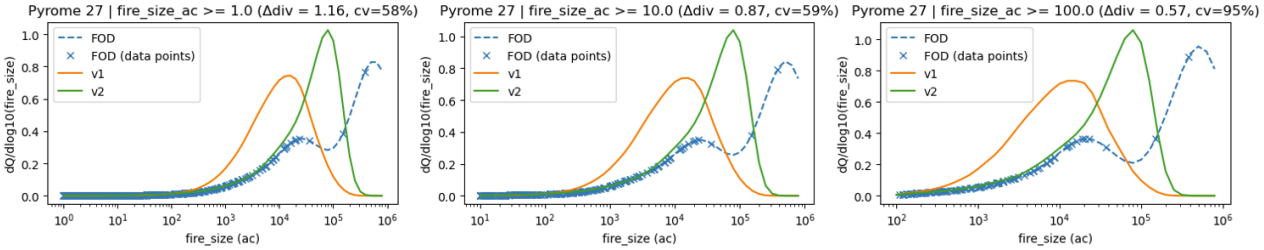
Pyrome 27 | fire_size_ac >= 1.0 (Δdiv = 1.16, cv=58%)
Pyrome 27 | fire_size_ac >= 10.0 (Δdiv = 0.87, cv=59%)
Pyrome 27 | fire_size_ac >= 100.0 (Δdiv = 0.57, cv=95%)
FOD
FOD (data points)
v1
v2
dQ/dlog10(fire_size)
fire_size (ac)

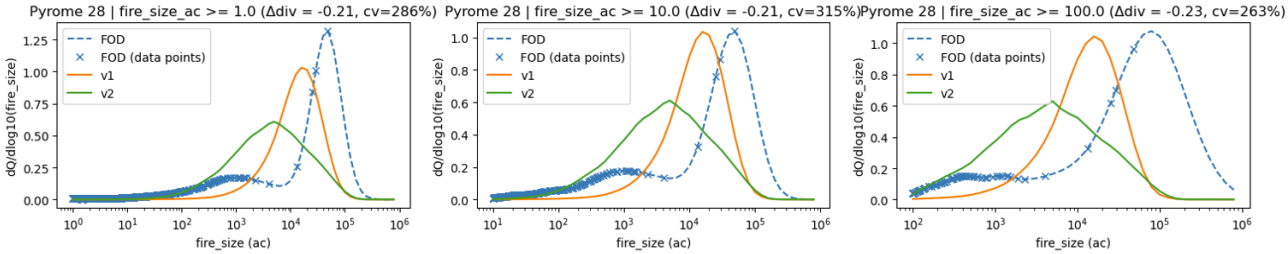
Pyrome 28 | fire_size_ac >= 1.0 (Δdiv = -0.21, cv=286%)
Pyrome 28 | fire_size_ac >= 10.0 (Δdiv = -0.21, cv=315%)
Pyrome 28 | fire_size_ac >= 100.0 (Δdiv = -0.23, cv=263%)
FOD
FOD (data points)
v1
v2
dQ/dlog10(fire_size)
fire_size (ac)

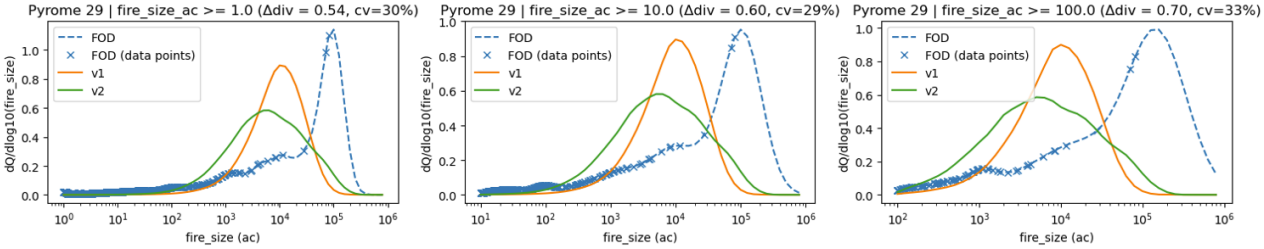
Pyrome 29 | fire_size_ac >= 1.0 (Δdiv = 0.54, cv=30%)
Pyrome 29 | fire_size_ac >= 10.0 (Δdiv = 0.60, cv=29%)
Pyrome 29 | fire_size_ac >= 100.0 (Δdiv = 0.70, cv=33%)
FOD
FOD (data points)
v1
v2
dQ/dlog10(fire_size)
fire_size (ac)

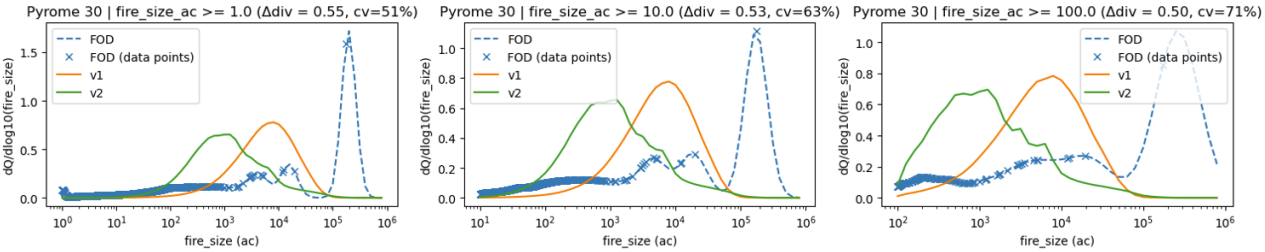
Pyrome 30 | fire_size_ac >= 1.0 (Δdiv = 0.55, cv=51%)
Pyrome 30 | fire_size_ac >= 10.0 (Δdiv = 0.53, cv=63%)
Pyrome 30 | fire_size_ac >= 100.0 (Δdiv = 0.50, cv=71%)
FOD
FOD (data points)
v1
v2
dQ/dlog10(fire_size)
fire_size (ac)

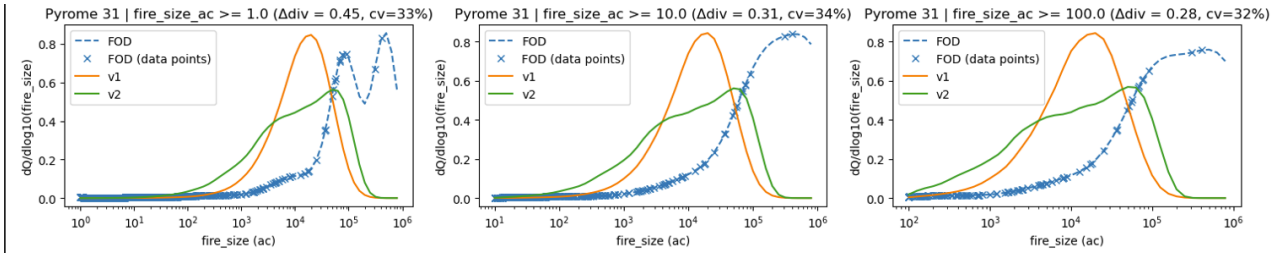
Pyrome 31 | fire_size_ac >= 1.0 (Δdiv = 0.45, cv=33%)
Pyrome 31 | fire_size_ac >= 10.0 (Δdiv = 0.31, cv=34%)
Pyrome 31 | fire_size_ac >= 100.0 (Δdiv = 0.28, cv=32%)
FOD
FOD (data points)
v1
v2
dQ/dlog10(fire_size)
fire_size (ac)

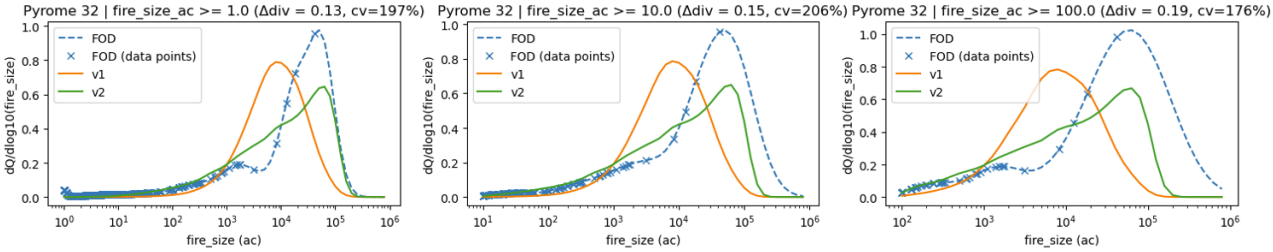
Pyrome 32 | fire_size_ac >= 1.0 (Δdiv = 0.13, cv=197%)
Pyrome 32 | fire_size_ac >= 10.0 (Δdiv = 0.15, cv=206%)
Pyrome 32 | fire_size_ac >= 100.0 (Δdiv = 0.19, cv=176%)
FOD
FOD (data points)
v1
v2
dQ/dlog10(fire_size)
fire_size (ac)

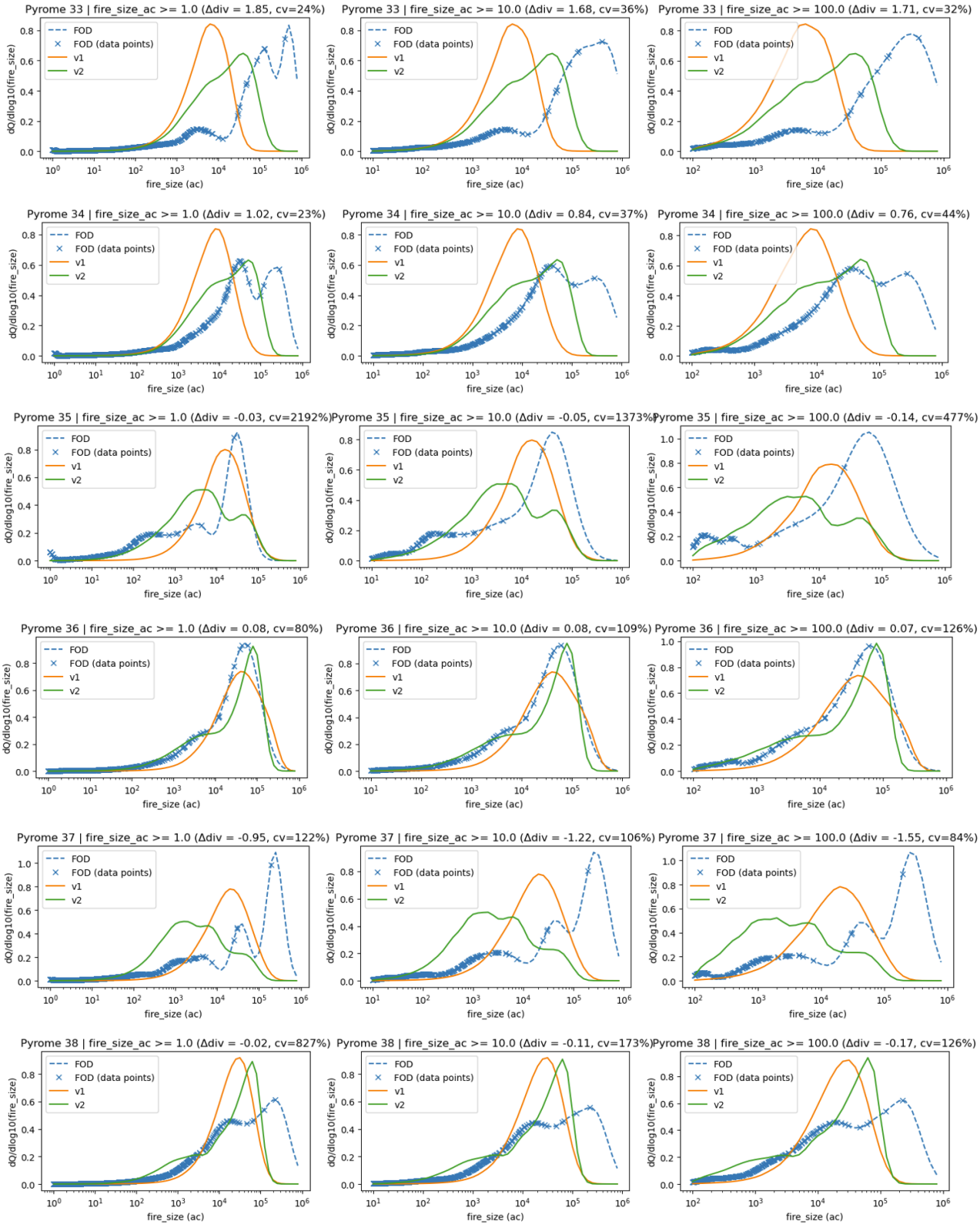
Pyrome 33 | fire_size_ac >= 1.0 (Δdiv = 1.85, cv=24%)
Pyrome 33 | fire_size_ac >= 10.0 (Δdiv = 1.68, cv=36%)
Pyrome 33 | fire_size_ac >= 100.0 (Δdiv = 1.71, cv=32%)
Pyrome 34 | fire_size_ac >= 1.0 (Δdiv = 1.02, cv=23%)
Pyrome 34 | fire_size_ac >= 10.0 (Δdiv = 0.84, cv=37%)
Pyrome 34 | fire_size_ac >= 100.0 (Δdiv = 0.76, cv=44%)
Pyrome 35 | fire_size_ac >= 1.0 (Δdiv = -0.03, cv=2192%)
Pyrome 35 | fire_size_ac >= 10.0 (Δdiv = -0.05, cv=1373%)
Pyrome 35 | fire_size_ac >= 100.0 (Δdiv = -0.14, cv=477%)
Pyrome 36 | fire_size_ac >= 1.0 (Δdiv = 0.08, cv=80%)
Pyrome 36 | fire_size_ac >= 10.0 (Δdiv = 0.08, cv=109%)
Pyrome 36 | fire_size_ac >= 100.0 (Δdiv = 0.07, cv=126%)
Pyrome 37 | fire_size_ac >= 1.0 (Δdiv = -0.95, cv=122%)
Pyrome 37 | fire_size_ac >= 10.0 (Δdiv = -1.22, cv=106%)
Pyrome 37 | fire_size_ac >= 100.0 (Δdiv = -1.55, cv=84%)
Pyrome 38 | fire_size_ac >= 1.0 (Δdiv = -0.02, cv=827%)
Pyrome 38 | fire_size_ac >= 10.0 (Δdiv = -0.11, cv=173%)
Pyrome 38 | fire_size_ac >= 100.0 (Δdiv = -0.17, cv=126%)
FOD
FOD (data points)
v1
v2
dQ/dlog10(fire_size)
fire_size (ac)

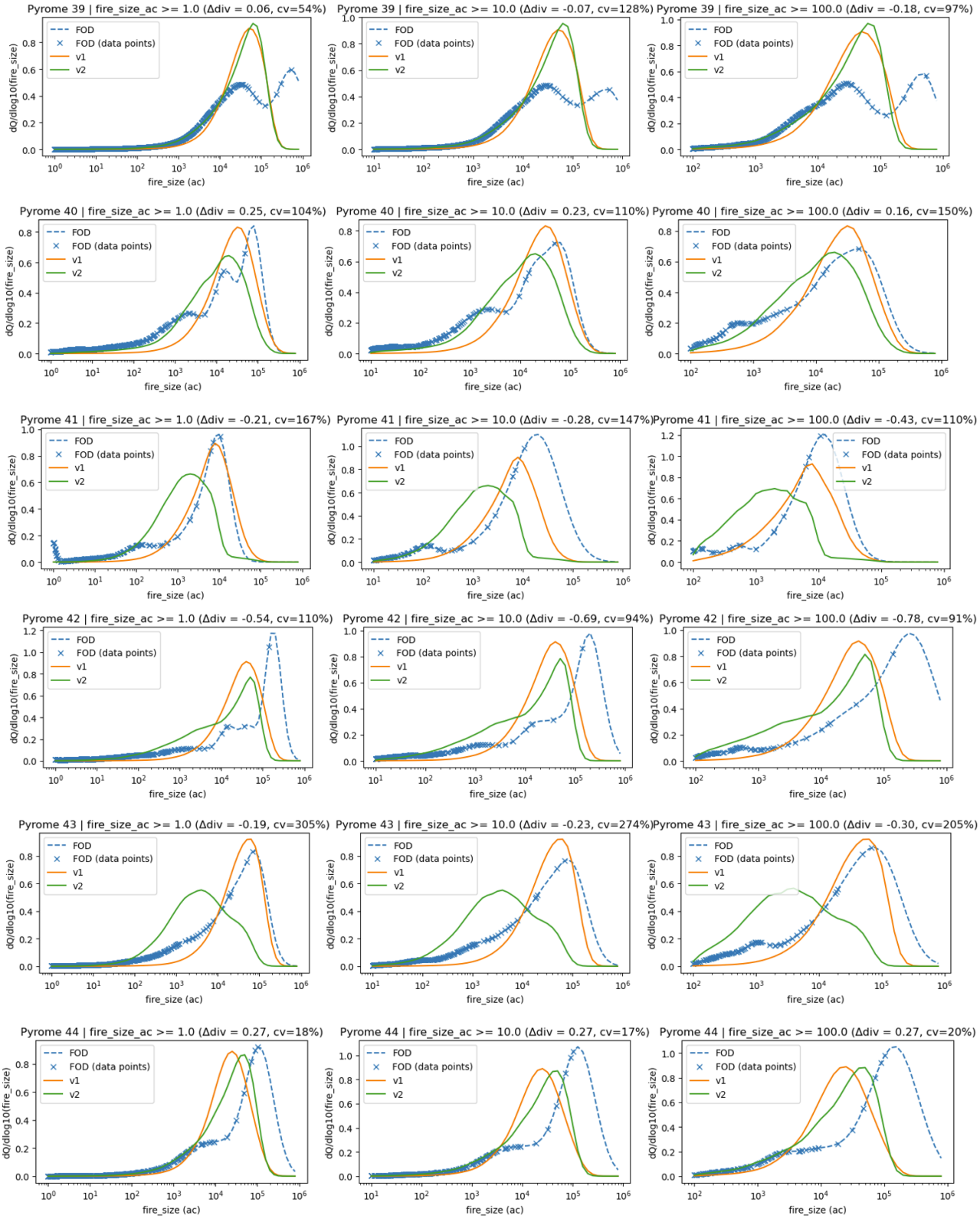
Pyrome 39 | fire_size_ac >= 1.0 (Δdiv = 0.06, cv=54%)
Pyrome 39 | fire_size_ac >= 10.0 (Δdiv = -0.07, cv=128%)
Pyrome 39 | fire_size_ac >= 100.0 (Δdiv = -0.18, cv=97%)
Pyrome 40 | fire_size_ac >= 1.0 (Δdiv = 0.25, cv=104%)
Pyrome 40 | fire_size_ac >= 10.0 (Δdiv = 0.23, cv=110%)
Pyrome 40 | fire_size_ac >= 100.0 (Δdiv = 0.16, cv=150%)
Pyrome 41 | fire_size_ac >= 1.0 (Δdiv = -0.21, cv=167%)
Pyrome 41 | fire_size_ac >= 10.0 (Δdiv = -0.28, cv=147%)
Pyrome 41 | fire_size_ac >= 100.0 (Δdiv = -0.43, cv=110%)
Pyrome 42 | fire_size_ac >= 1.0 (Δdiv = -0.54, cv=110%)
Pyrome 42 | fire_size_ac >= 10.0 (Δdiv = -0.69, cv=94%)
Pyrome 42 | fire_size_ac >= 100.0 (Δdiv = -0.78, cv=91%)
Pyrome 43 | fire_size_ac >= 1.0 (Δdiv = -0.19, cv=305%)
Pyrome 43 | fire_size_ac >= 10.0 (Δdiv = -0.23, cv=274%)
Pyrome 43 | fire_size_ac >= 100.0 (Δdiv = -0.30, cv=205%)
Pyrome 44 | fire_size_ac >= 1.0 (Δdiv = 0.27, cv=18%)
Pyrome 44 | fire_size_ac >= 10.0 (Δdiv = 0.27, cv=17%)
Pyrome 44 | fire_size_ac >= 100.0 (Δdiv = 0.27, cv=20%)
FOD
FOD (data points)
v1
v2
dQ/dlog10(fire_size)
fire_size (ac)

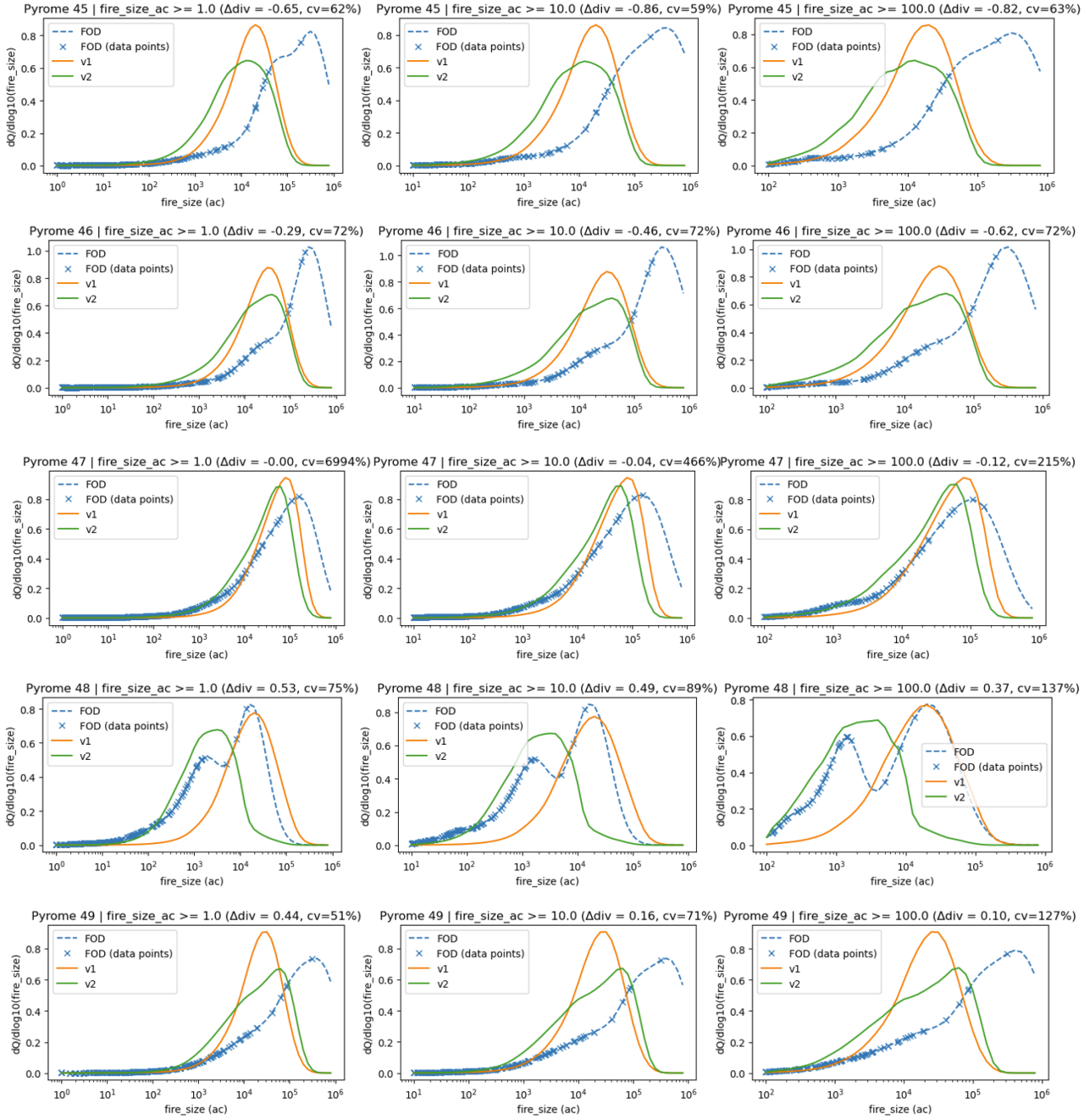
Pyrome 45 | fire_size_ac >= 1.0 (Δdiv = -0.65, cv=62%)
Pyrome 45 | fire_size_ac >= 10.0 (Δdiv = -0.86, cv=59%)
Pyrome 45 | fire_size_ac >= 100.0 (Δdiv = -0.82, cv=63%)
Pyrome 46 | fire_size_ac >= 1.0 (Δdiv = -0.29, cv=72%)
Pyrome 46 | fire_size_ac >= 10.0 (Δdiv = -0.46, cv=72%)
Pyrome 46 | fire_size_ac >= 100.0 (Δdiv = -0.62, cv=72%)
Pyrome 47 | fire_size_ac >= 1.0 (Δdiv = -0.00, cv=6994%)
Pyrome 47 | fire_size_ac >= 10.0 (Δdiv = -0.04, cv=466%)
Pyrome 47 | fire_size_ac >= 100.0 (Δdiv = -0.12, cv=215%)
Pyrome 48 | fire_size_ac >= 1.0 (Δdiv = 0.53, cv=75%)
Pyrome 48 | fire_size_ac >= 10.0 (Δdiv = 0.49, cv=89%)
Pyrome 48 | fire_size_ac >= 100.0 (Δdiv = 0.37, cv=137%)
Pyrome 49 | fire_size_ac >= 1.0 (Δdiv = 0.44, cv=51%)
Pyrome 49 | fire_size_ac >= 10.0 (Δdiv = 0.16, cv=71%)
Pyrome 49 | fire_size_ac >= 100.0 (Δdiv = 0.10, cv=127%)
FOD
FOD (data points)
v1
v2
dQ/dlog10(fire_size)
fire_size (ac)

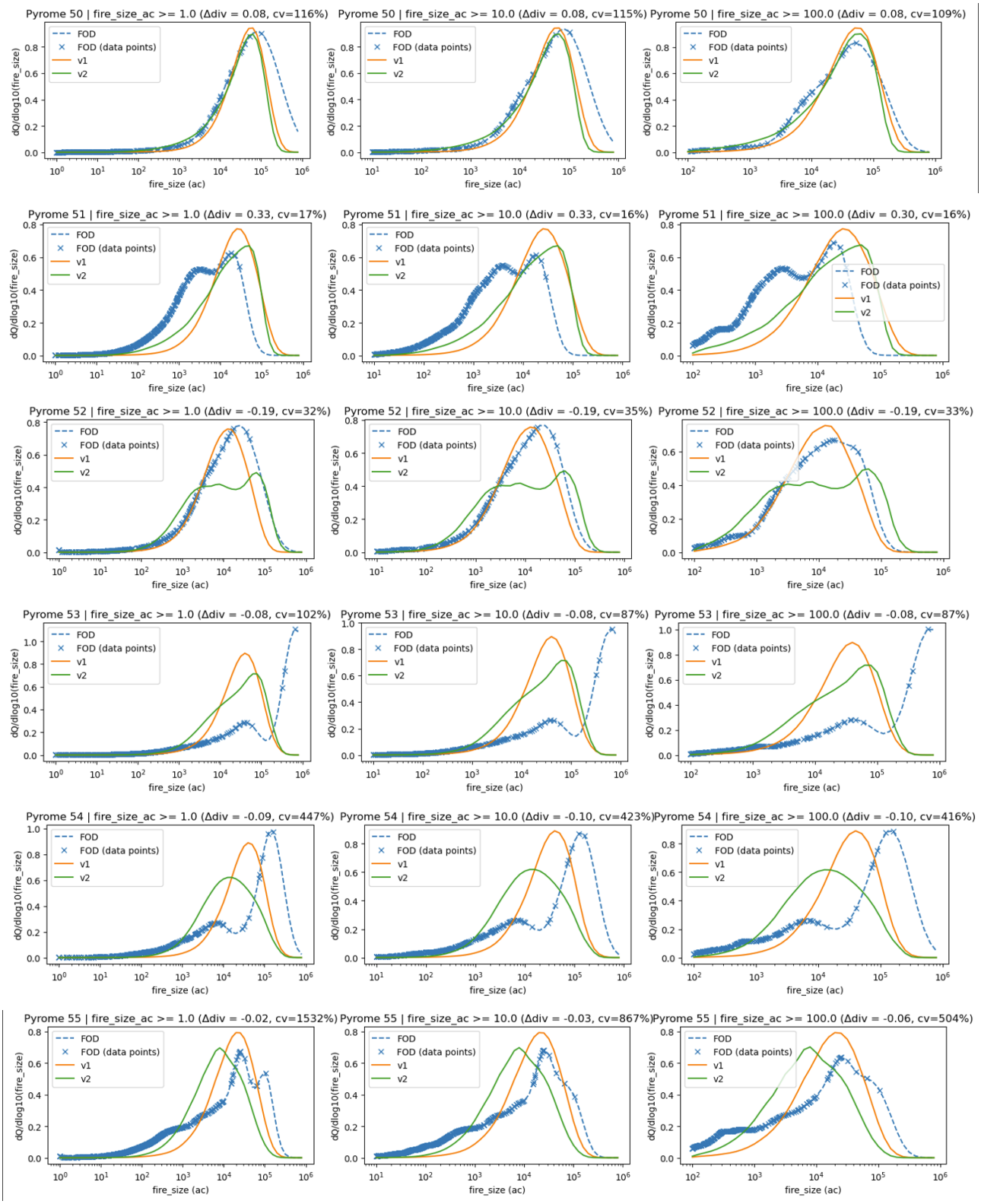
Pyrome 50 | fire_size_ac >= 1.0 (Δdiv = 0.08, cv=116%)
Pyrome 50 | fire_size_ac >= 10.0 (Δdiv = 0.08, cv=115%)
Pyrome 50 | fire_size_ac >= 100.0 (Δdiv = 0.08, cv=109%)
Pyrome 51 | fire_size_ac >= 1.0 (Δdiv = 0.33, cv=17%)
Pyrome 51 | fire_size_ac >= 10.0 (Δdiv = 0.33, cv=16%)
Pyrome 51 | fire_size_ac >= 100.0 (Δdiv = 0.30, cv=16%)
Pyrome 52 | fire_size_ac >= 1.0 (Δdiv = -0.19, cv=32%)
Pyrome 52 | fire_size_ac >= 10.0 (Δdiv = -0.19, cv=35%)
Pyrome 52 | fire_size_ac >= 100.0 (Δdiv = -0.19, cv=33%)
Pyrome 53 | fire_size_ac >= 1.0 (Δdiv = -0.08, cv=102%)
Pyrome 53 | fire_size_ac >= 10.0 (Δdiv = -0.08, cv=87%)
Pyrome 53 | fire_size_ac >= 100.0 (Δdiv = -0.08, cv=87%)
Pyrome 54 | fire_size_ac >= 1.0 (Δdiv = -0.09, cv=447%)
Pyrome 54 | fire_size_ac >= 10.0 (Δdiv = -0.10, cv=423%)
Pyrome 54 | fire_size_ac >= 100.0 (Δdiv = -0.10, cv=416%)
Pyrome 55 | fire_size_ac >= 1.0 (Δdiv = -0.02, cv=1532%)
Pyrome 55 | fire_size_ac >= 10.0 (Δdiv = -0.03, cv=867%)
Pyrome 55 | fire_size_ac >= 100.0 (Δdiv = -0.06, cv=504%)
FOD
FOD (data points)
v1
v2
dQ/dlog10(fire_size)
fire_size (ac)

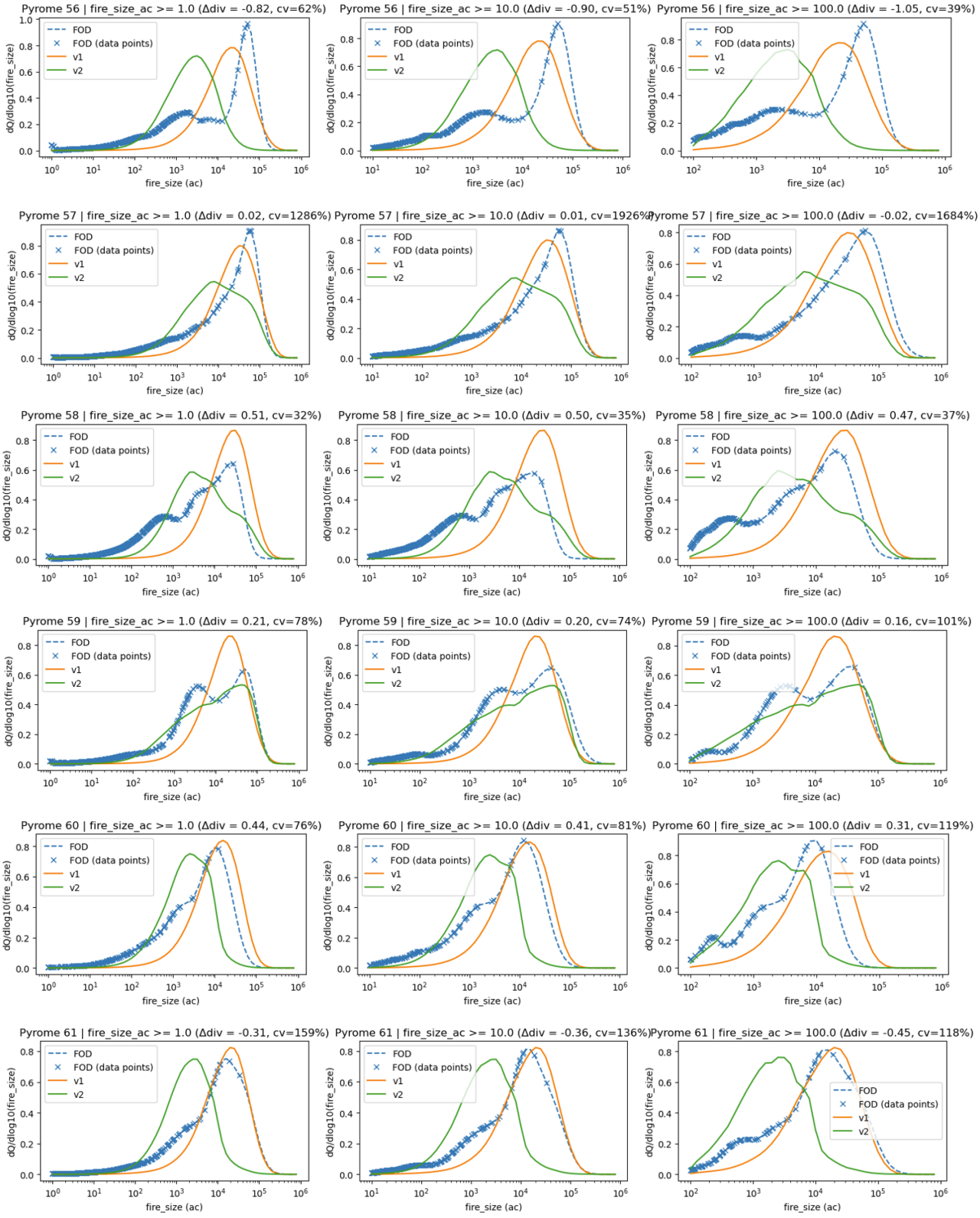
Pyrome 56 | fire_size_ac >= 1.0 (Δdiv = -0.82, cv=62%)
Pyrome 56 | fire_size_ac >= 10.0 (Δdiv = -0.90, cv=51%)
Pyrome 56 | fire_size_ac >= 100.0 (Δdiv = -1.05, cv=39%)
Pyrome 57 | fire_size_ac >= 1.0 (Δdiv = 0.02, cv=1286%)
Pyrome 57 | fire_size_ac >= 10.0 (Δdiv = 0.01, cv=1926%)
Pyrome 57 | fire_size_ac >= 100.0 (Δdiv = -0.02, cv=1684%)
Pyrome 58 | fire_size_ac >= 1.0 (Δdiv = 0.51, cv=32%)
Pyrome 58 | fire_size_ac >= 10.0 (Δdiv = 0.50, cv=35%)
Pyrome 58 | fire_size_ac >= 100.0 (Δdiv = 0.47, cv=37%)
Pyrome 59 | fire_size_ac >= 1.0 (Δdiv = 0.21, cv=78%)
Pyrome 59 | fire_size_ac >= 10.0 (Δdiv = 0.20, cv=74%)
Pyrome 59 | fire_size_ac >= 100.0 (Δdiv = 0.16, cv=101%)
Pyrome 60 | fire_size_ac >= 1.0 (Δdiv = 0.44, cv=76%)
Pyrome 60 | fire_size_ac >= 10.0 (Δdiv = 0.41, cv=81%)
Pyrome 60 | fire_size_ac >= 100.0 (Δdiv = 0.31, cv=119%)
Pyrome 61 | fire_size_ac >= 1.0 (Δdiv = -0.31, cv=159%)
Pyrome 61 | fire_size_ac >= 10.0 (Δdiv = -0.36, cv=136%)
Pyrome 61 | fire_size_ac >= 100.0 (Δdiv = -0.45, cv=118%)
FOD
FOD (data points)
v1
v2
dQ/dlog10(fire_size)
fire_size (ac)

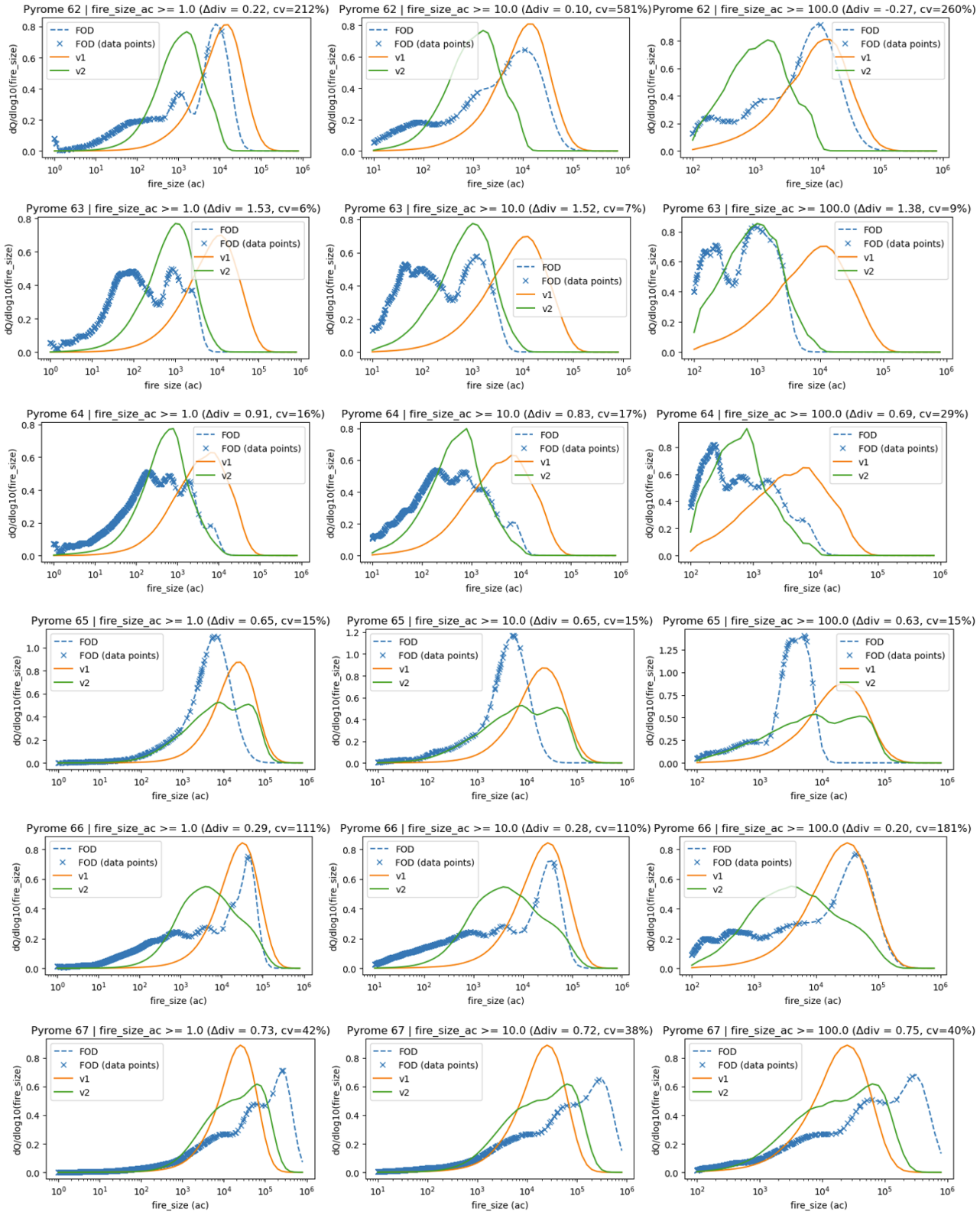
Pyrome 62 | fire_size_ac >= 1.0 (Δdiv = 0.22, cv=212%)
Pyrome 62 | fire_size_ac >= 10.0 (Δdiv = 0.10, cv=581%)
Pyrome 62 | fire_size_ac >= 100.0 (Δdiv = -0.27, cv=260%)
Pyrome 63 | fire_size_ac >= 1.0 (Δdiv = 1.53, cv=6%)
Pyrome 63 | fire_size_ac >= 10.0 (Δdiv = 1.52, cv=7%)
Pyrome 63 | fire_size_ac >= 100.0 (Δdiv = 1.38, cv=9%)
Pyrome 64 | fire_size_ac >= 1.0 (Δdiv = 0.91, cv=16%)
Pyrome 64 | fire_size_ac >= 10.0 (Δdiv = 0.83, cv=17%)
Pyrome 64 | fire_size_ac >= 100.0 (Δdiv = 0.69, cv=29%)
Pyrome 65 | fire_size_ac >= 1.0 (Δdiv = 0.65, cv=15%)
Pyrome 65 | fire_size_ac >= 10.0 (Δdiv = 0.65, cv=15%)
Pyrome 65 | fire_size_ac >= 100.0 (Δdiv = 0.63, cv=15%)
Pyrome 66 | fire_size_ac >= 1.0 (Δdiv = 0.29, cv=111%)
Pyrome 66 | fire_size_ac >= 10.0 (Δdiv = 0.28, cv=110%)
Pyrome 66 | fire_size_ac >= 100.0 (Δdiv = 0.20, cv=181%)
Pyrome 67 | fire_size_ac >= 1.0 (Δdiv = 0.73, cv=42%)
Pyrome 67 | fire_size_ac >= 10.0 (Δdiv = 0.72, cv=38%)
Pyrome 67 | fire_size_ac >= 100.0 (Δdiv = 0.75, cv=40%)
FOD
FOD (data points)
v1
v2
dQ/dlog10(fire_size)
fire_size (ac)

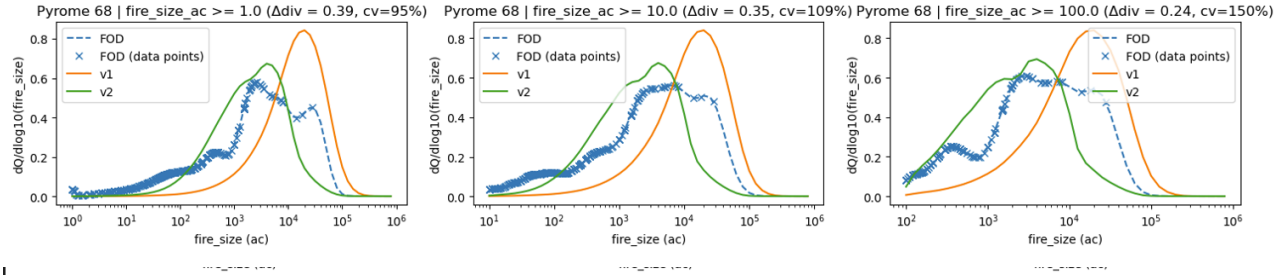
Pyrome 68 | fire_size_ac >= 1.0 (Δdiv = 0.39, cv=95%)
Pyrome 68 | fire_size_ac >= 10.0 (Δdiv = 0.35, cv=109%)
Pyrome 68 | fire_size_ac >= 100.0 (Δdiv = 0.24, cv=150%)
FOD
FOD (data points)
v1
v2
dQ/dlog10(fire_size)
fire_size (ac)

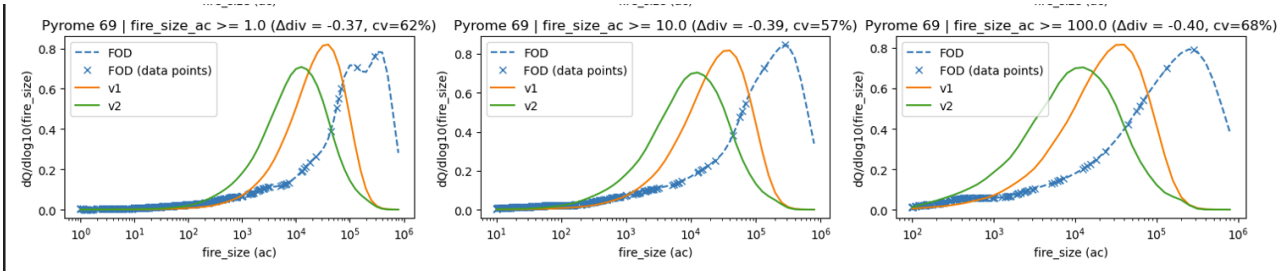
Pyrome 69 | fire_size_ac >= 1.0 (Δdiv = -0.37, cv=62%)
Pyrome 69 | fire_size_ac >= 10.0 (Δdiv = -0.39, cv=57%)
Pyrome 69 | fire_size_ac >= 100.0 (Δdiv = -0.40, cv=68%)
FOD
FOD (data points)
v1
v2
dQ/dlog10(fire_size)
fire_size (ac)

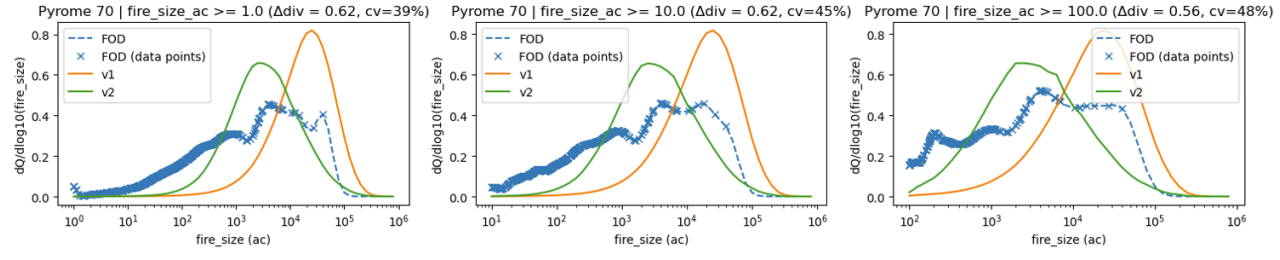
Pyrome 70 | fire_size_ac >= 1.0 (Δdiv = 0.62, cv=39%)
Pyrome 70 | fire_size_ac >= 10.0 (Δdiv = 0.62, cv=45%)
Pyrome 70 | fire_size_ac >= 100.0 (Δdiv = 0.56, cv=48%)
FOD
FOD (data points)
v1
v2
dQ/dlog10(fire_size)
fire_size (ac)

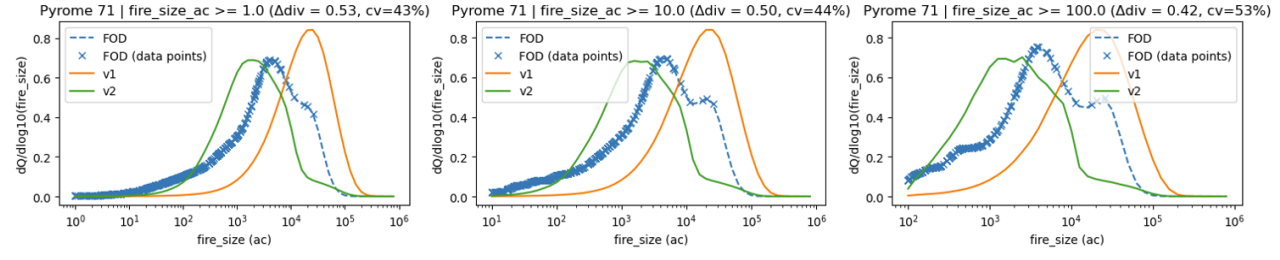
Pyrome 71 | fire_size_ac >= 1.0 (Δdiv = 0.53, cv=43%)
Pyrome 71 | fire_size_ac >= 10.0 (Δdiv = 0.50, cv=44%)
Pyrome 71 | fire_size_ac >= 100.0 (Δdiv = 0.42, cv=53%)
FOD
FOD (data points)
v1
v2
dQ/dlog10(fire_size)
fire_size (ac)

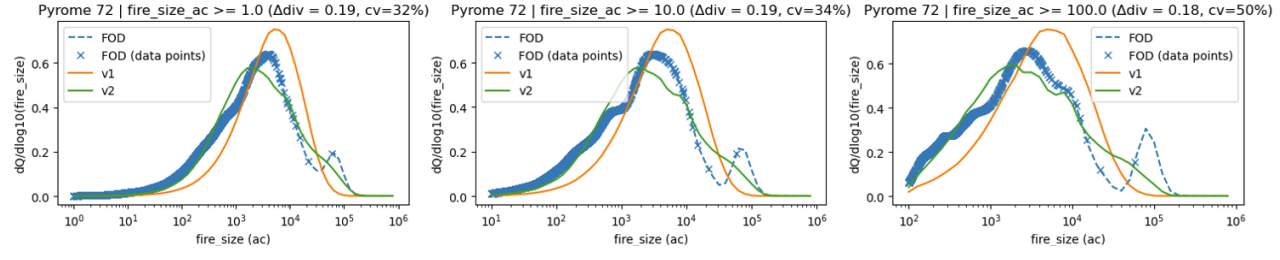
Pyrome 72 | fire_size_ac >= 1.0 (Δdiv = 0.19, cv=32%)
Pyrome 72 | fire_size_ac >= 10.0 (Δdiv = 0.19, cv=34%)
Pyrome 72 | fire_size_ac >= 100.0 (Δdiv = 0.18, cv=50%)
FOD
FOD (data points)
v1
v2
dQ/dlog10(fire_size)
fire_size (ac)

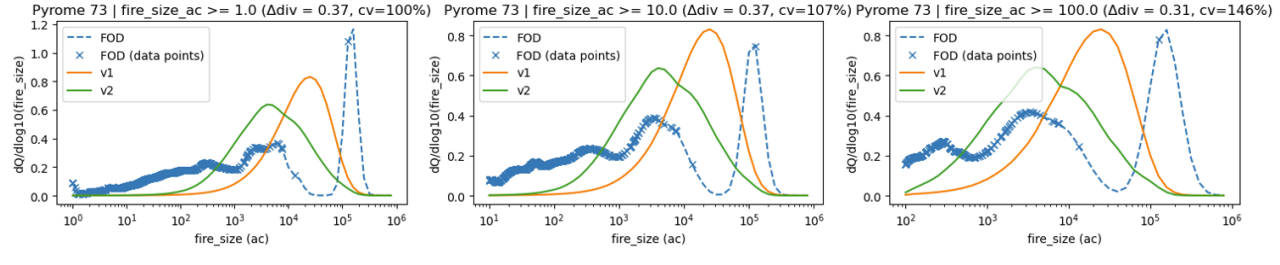
Pyrome 73 | fire_size_ac >= 1.0 (Δdiv = 0.37, cv=100%)
Pyrome 73 | fire_size_ac >= 10.0 (Δdiv = 0.37, cv=107%)
Pyrome 73 | fire_size_ac >= 100.0 (Δdiv = 0.31, cv=146%)
FOD
FOD (data points)
v1
v2
dQ/dlog10(fire_size)
fire_size (ac)

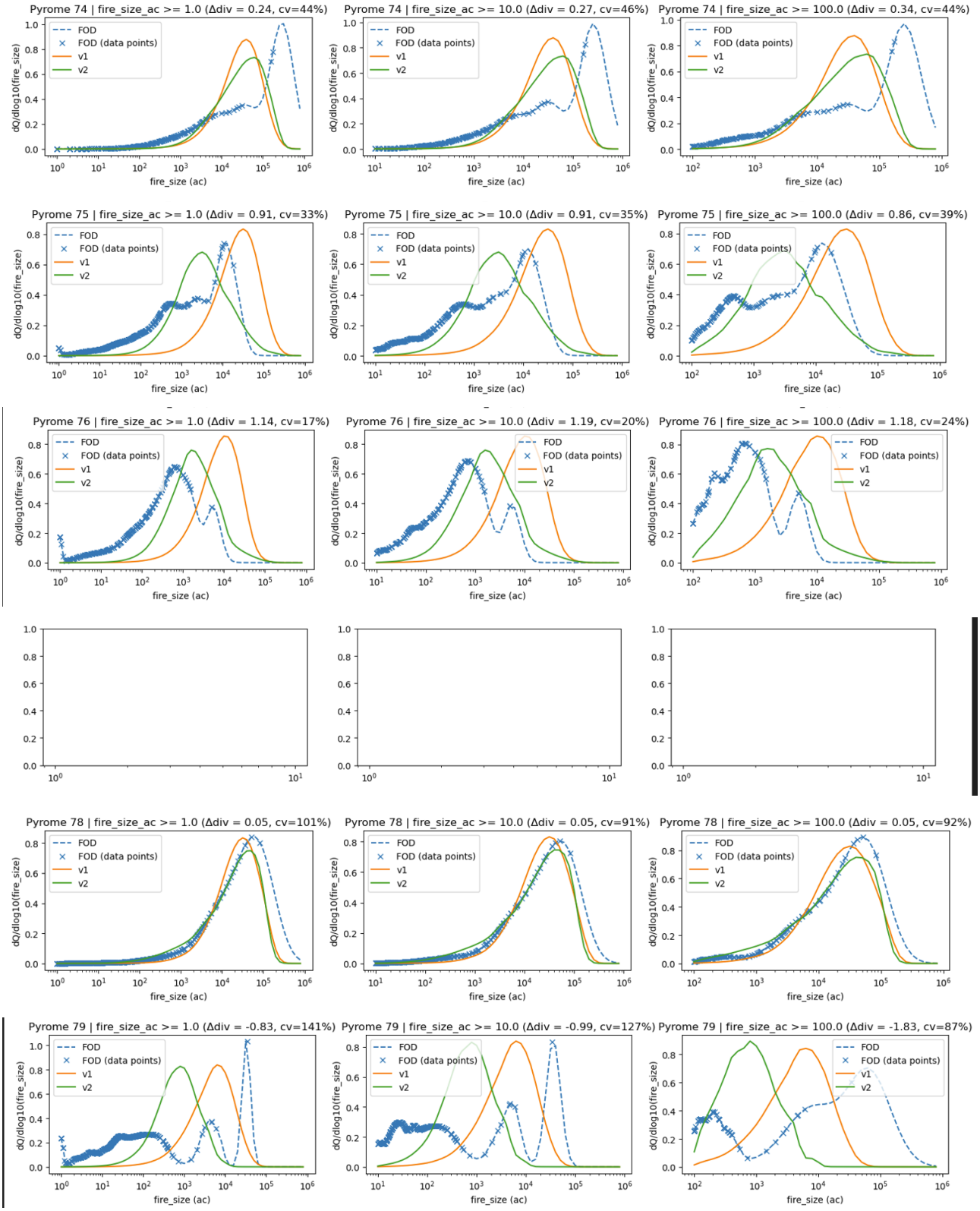
Pyrome 74 | fire_size_ac >= 1.0 (Δdiv = 0.24, cv=44%)
Pyrome 74 | fire_size_ac >= 10.0 (Δdiv = 0.27, cv=46%)
Pyrome 74 | fire_size_ac >= 100.0 (Δdiv = 0.34, cv=44%)
Pyrome 75 | fire_size_ac >= 1.0 (Δdiv = 0.91, cv=33%)
Pyrome 75 | fire_size_ac >= 10.0 (Δdiv = 0.91, cv=35%)
Pyrome 75 | fire_size_ac >= 100.0 (Δdiv = 0.86, cv=39%)
Pyrome 76 | fire_size_ac >= 1.0 (Δdiv = 1.14, cv=17%)
Pyrome 76 | fire_size_ac >= 10.0 (Δdiv = 1.19, cv=20%)
Pyrome 76 | fire_size_ac >= 100.0 (Δdiv = 1.18, cv=24%)
Pyrome 78 | fire_size_ac >= 1.0 (Δdiv = 0.05, cv=101%)
Pyrome 78 | fire_size_ac >= 10.0 (Δdiv = 0.05, cv=91%)
Pyrome 78 | fire_size_ac >= 100.0 (Δdiv = 0.05, cv=92%)
Pyrome 79 | fire_size_ac >= 1.0 (Δdiv = -0.83, cv=141%)
Pyrome 79 | fire_size_ac >= 10.0 (Δdiv = -0.99, cv=127%)
Pyrome 79 | fire_size_ac >= 100.0 (Δdiv = -1.83, cv=87%)
FOD
FOD (data points)
v1
v2
dQ/dlog10(fire_size)
fire_size (ac)

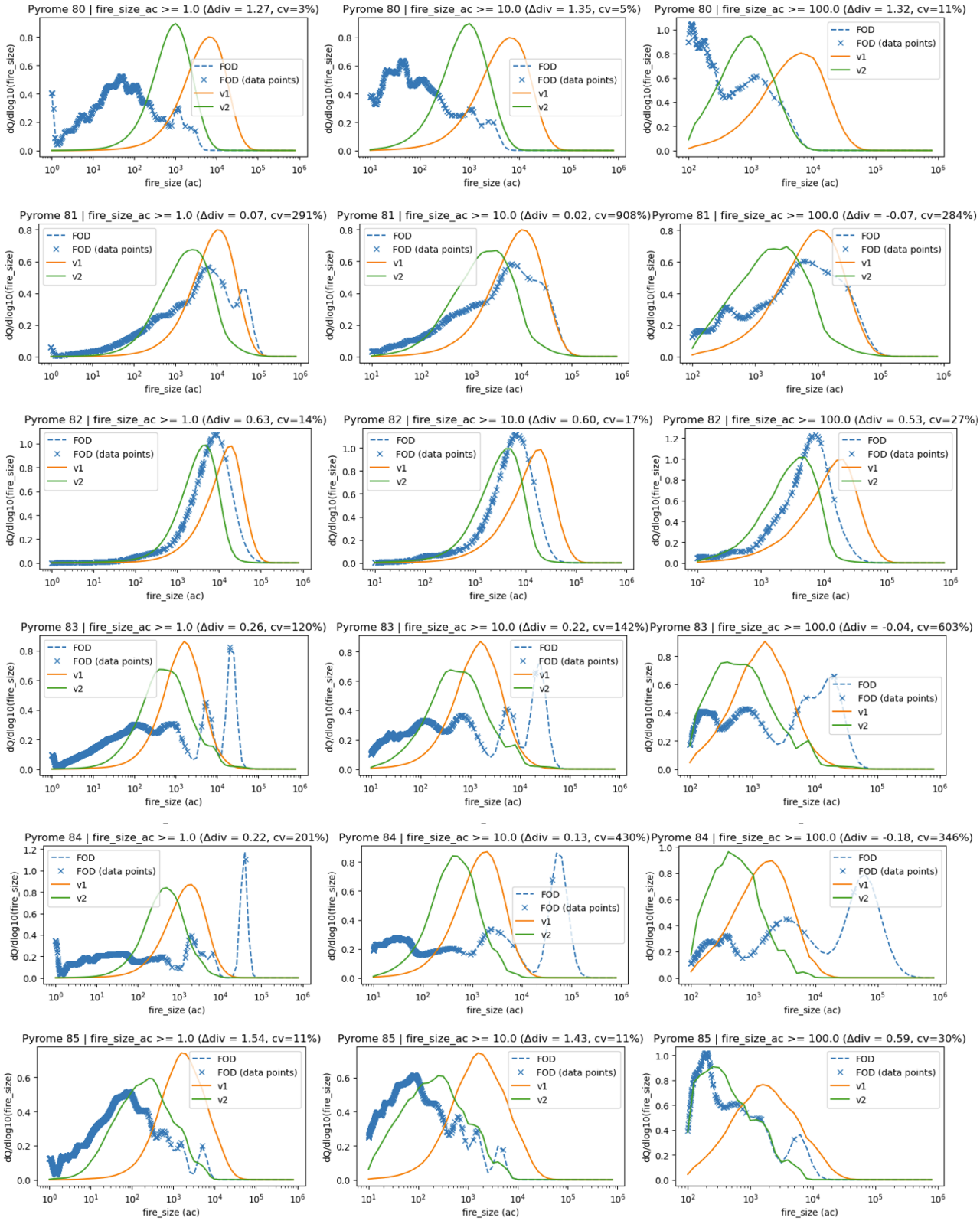
Pyrome 80 | fire_size_ac >= 1.0 (Δdiv = 1.27, cv=3%)
Pyrome 80 | fire_size_ac >= 10.0 (Δdiv = 1.35, cv=5%)
Pyrome 80 | fire_size_ac >= 100.0 (Δdiv = 1.32, cv=11%)
Pyrome 81 | fire_size_ac >= 1.0 (Δdiv = 0.07, cv=291%)
Pyrome 81 | fire_size_ac >= 10.0 (Δdiv = 0.02, cv=908%)
Pyrome 81 | fire_size_ac >= 100.0 (Δdiv = -0.07, cv=284%)
Pyrome 82 | fire_size_ac >= 1.0 (Δdiv = 0.63, cv=14%)
Pyrome 82 | fire_size_ac >= 10.0 (Δdiv = 0.60, cv=17%)
Pyrome 82 | fire_size_ac >= 100.0 (Δdiv = 0.53, cv=27%)
Pyrome 83 | fire_size_ac >= 1.0 (Δdiv = 0.26, cv=120%)
Pyrome 83 | fire_size_ac >= 10.0 (Δdiv = 0.22, cv=142%)
Pyrome 83 | fire_size_ac >= 100.0 (Δdiv = -0.04, cv=603%)
Pyrome 84 | fire_size_ac >= 1.0 (Δdiv = 0.22, cv=201%)
Pyrome 84 | fire_size_ac >= 10.0 (Δdiv = 0.13, cv=430%)
Pyrome 84 | fire_size_ac >= 100.0 (Δdiv = -0.18, cv=346%)
Pyrome 85 | fire_size_ac >= 1.0 (Δdiv = 1.54, cv=11%)
Pyrome 85 | fire_size_ac >= 10.0 (Δdiv = 1.43, cv=11%)
Pyrome 85 | fire_size_ac >= 100.0 (Δdiv = 0.59, cv=30%)
FOD
FOD (data points)
v1
v2
dQ/dlog10(fire_size)
fire_size (ac)

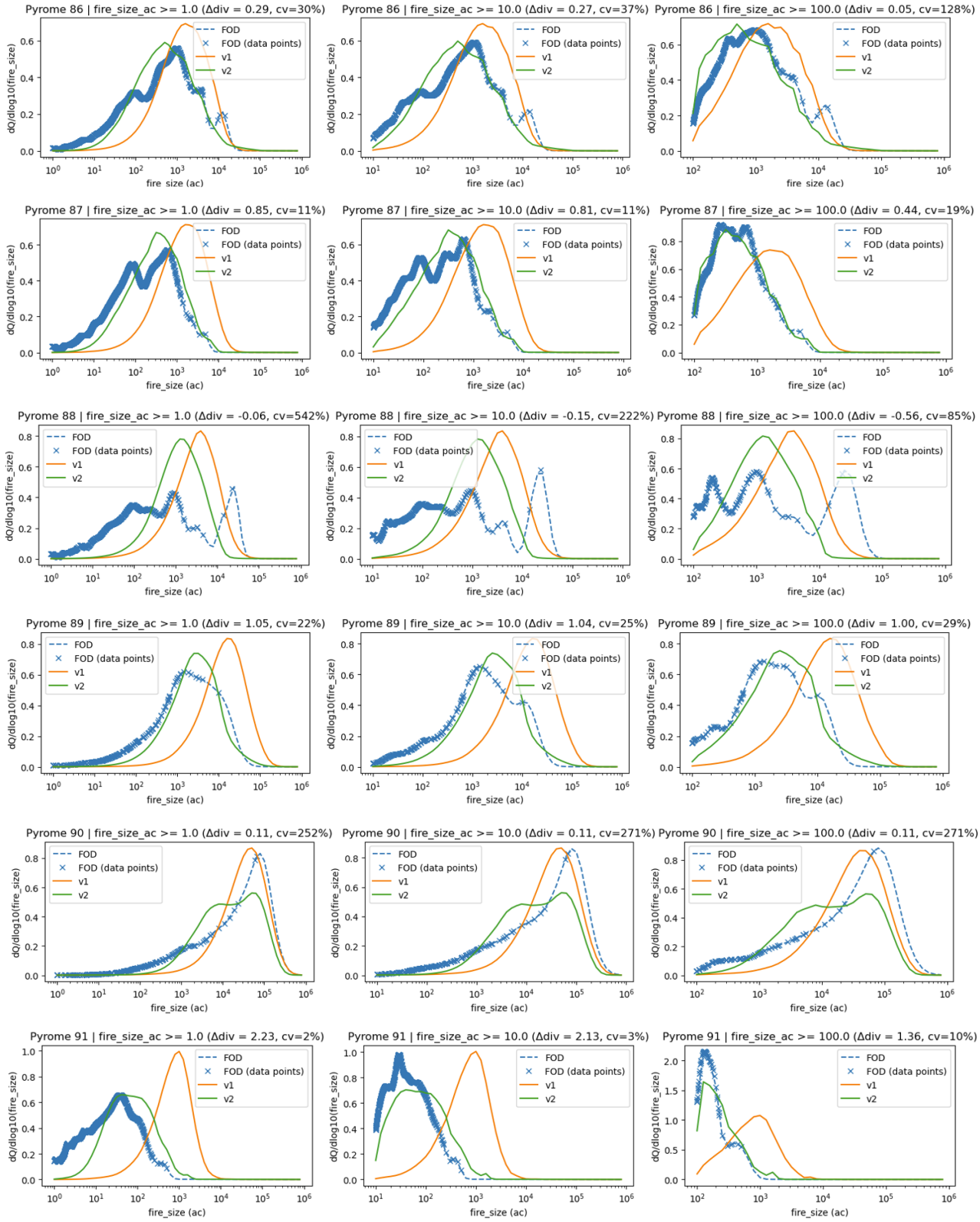
Pyrome 86 | fire_size_ac >= 1.0 (Δdiv = 0.29, cv=30%)
Pyrome 86 | fire_size_ac >= 10.0 (Δdiv = 0.27, cv=37%)
Pyrome 86 | fire_size_ac >= 100.0 (Δdiv = 0.05, cv=128%)
Pyrome 87 | fire_size_ac >= 1.0 (Δdiv = 0.85, cv=11%)
Pyrome 87 | fire_size_ac >= 10.0 (Δdiv = 0.81, cv=11%)
Pyrome 87 | fire_size_ac >= 100.0 (Δdiv = 0.44, cv=19%)
Pyrome 88 | fire_size_ac >= 1.0 (Δdiv = -0.06, cv=542%)
Pyrome 88 | fire_size_ac >= 10.0 (Δdiv = -0.15, cv=222%)
Pyrome 88 | fire_size_ac >= 100.0 (Δdiv = -0.56, cv=85%)
Pyrome 89 | fire_size_ac >= 1.0 (Δdiv = 1.05, cv=22%)
Pyrome 89 | fire_size_ac >= 10.0 (Δdiv = 1.04, cv=25%)
Pyrome 89 | fire_size_ac >= 100.0 (Δdiv = 1.00, cv=29%)
Pyrome 90 | fire_size_ac >= 1.0 (Δdiv = 0.11, cv=252%)
Pyrome 90 | fire_size_ac >= 10.0 (Δdiv = 0.11, cv=271%)
Pyrome 90 | fire_size_ac >= 100.0 (Δdiv = 0.11, cv=271%)
Pyrome 91 | fire_size_ac >= 1.0 (Δdiv = 2.23, cv=2%)
Pyrome 91 | fire_size_ac >= 10.0 (Δdiv = 2.13, cv=3%)
Pyrome 91 | fire_size_ac >= 100.0 (Δdiv = 1.36, cv=10%)
FOD
FOD (data points)
v1
v2
dQ/dlog10(fire_size)
fire_size (ac)

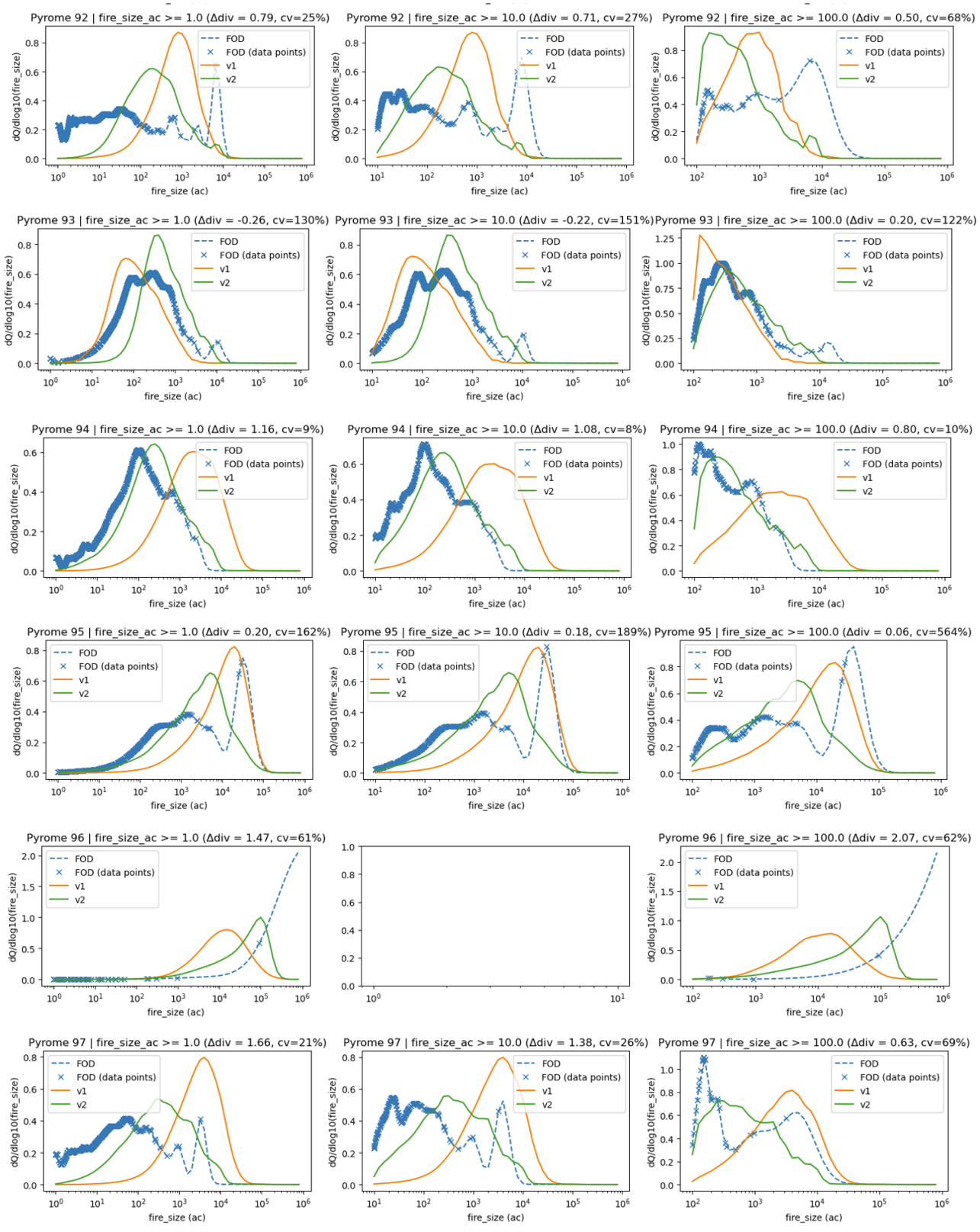
Pyrome 92 | fire_size_ac >= 1.0 (Δdiv = 0.79, cv=25%)
Pyrome 92 | fire_size_ac >= 10.0 (Δdiv = 0.71, cv=27%)
Pyrome 92 | fire_size_ac >= 100.0 (Δdiv = 0.50, cv=68%)
Pyrome 93 | fire_size_ac >= 1.0 (Δdiv = -0.26, cv=130%)
Pyrome 93 | fire_size_ac >= 10.0 (Δdiv = -0.22, cv=151%)
Pyrome 93 | fire_size_ac >= 100.0 (Δdiv = 0.20, cv=122%)
Pyrome 94 | fire_size_ac >= 1.0 (Δdiv = 1.16, cv=9%)
Pyrome 94 | fire_size_ac >= 10.0 (Δdiv = 1.08, cv=8%)
Pyrome 94 | fire_size_ac >= 100.0 (Δdiv = 0.80, cv=10%)
Pyrome 95 | fire_size_ac >= 1.0 (Δdiv = 0.20, cv=162%)
Pyrome 95 | fire_size_ac >= 10.0 (Δdiv = 0.18, cv=189%)
Pyrome 95 | fire_size_ac >= 100.0 (Δdiv = 0.06, cv=564%)
Pyrome 96 | fire_size_ac >= 1.0 (Δdiv = 1.47, cv=61%)
Pyrome 96 | fire_size_ac >= 100.0 (Δdiv = 2.07, cv=62%)
Pyrome 97 | fire_size_ac >= 1.0 (Δdiv = 1.66, cv=21%)
Pyrome 97 | fire_size_ac >= 10.0 (Δdiv = 1.38, cv=26%)
Pyrome 97 | fire_size_ac >= 100.0 (Δdiv = 0.63, cv=69%)
FOD
FOD (data points)
v1
v2
dQ/dlog10(fire_size)
fire_size (ac)

FIRST STREET FOUNDATION

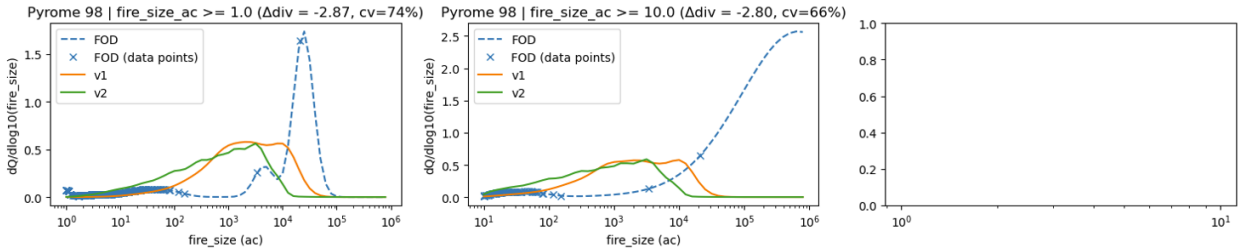

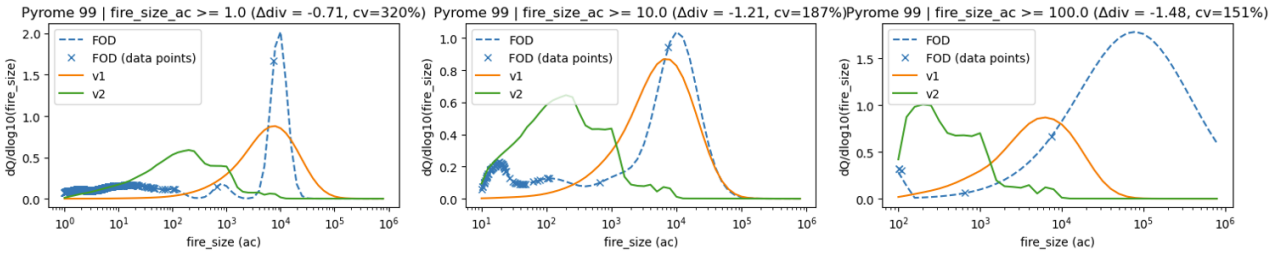

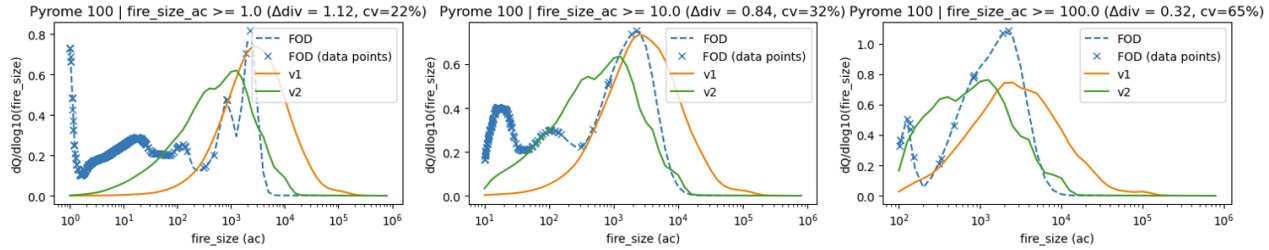

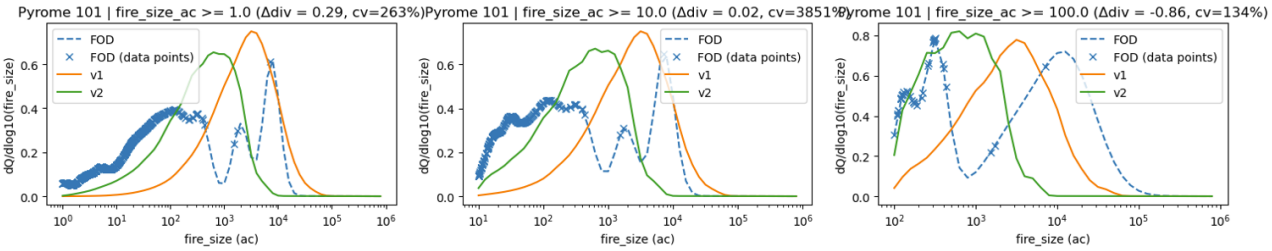

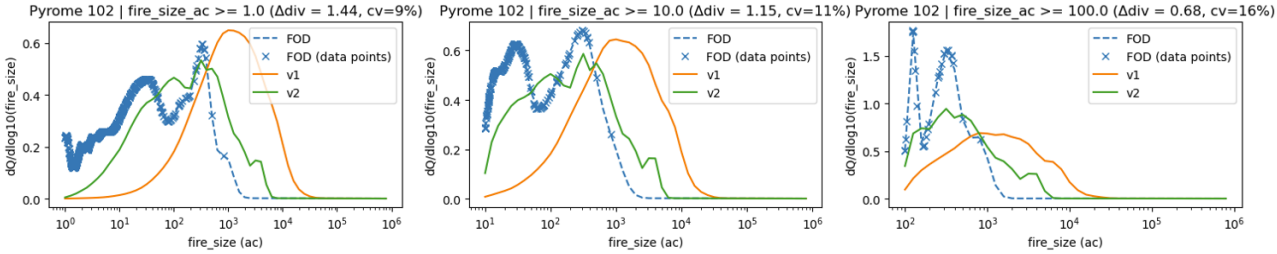

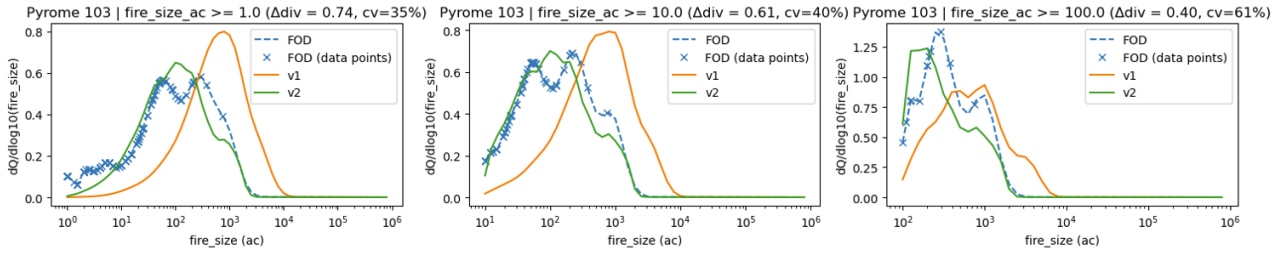

FIRST STREET FOUNDATION

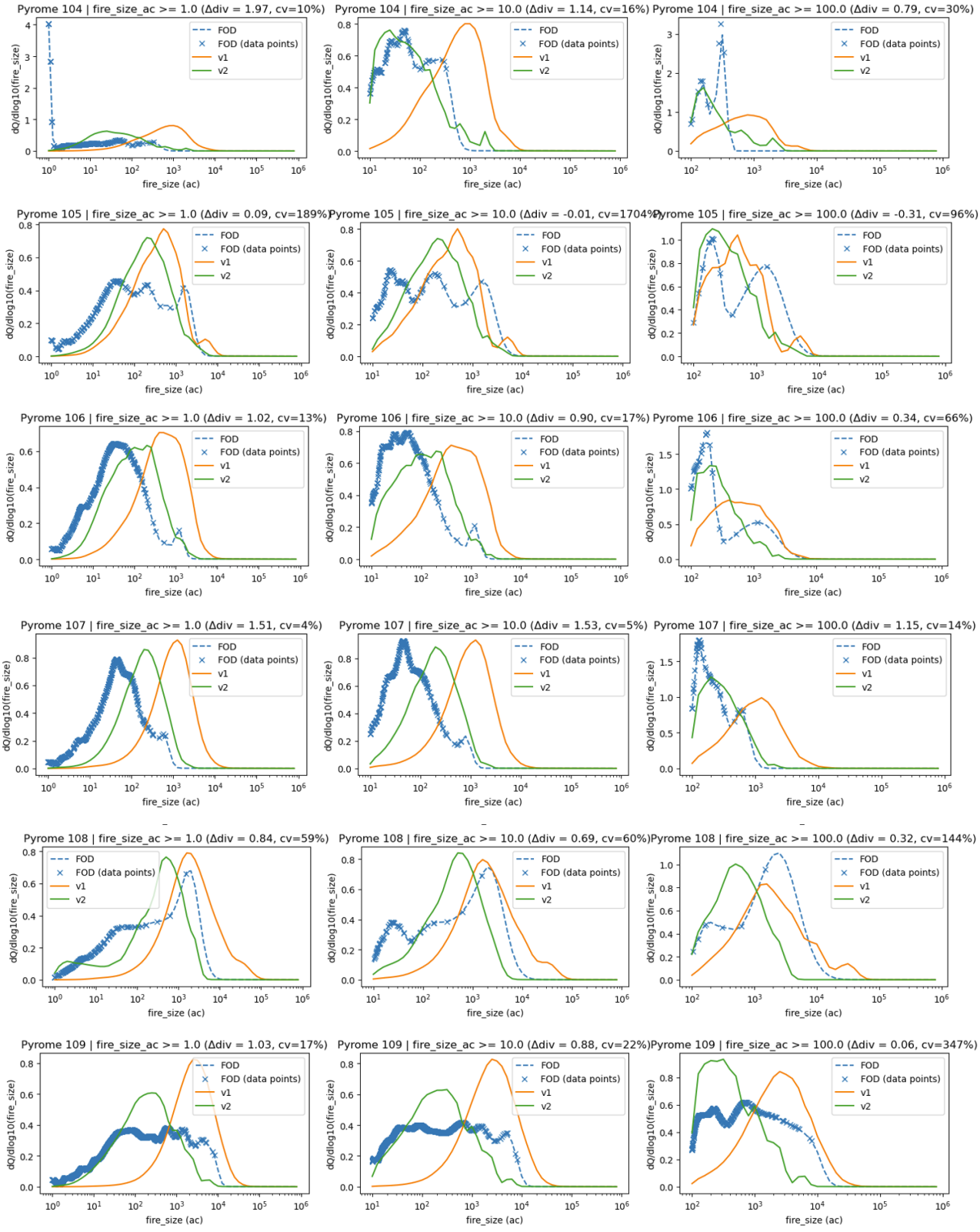

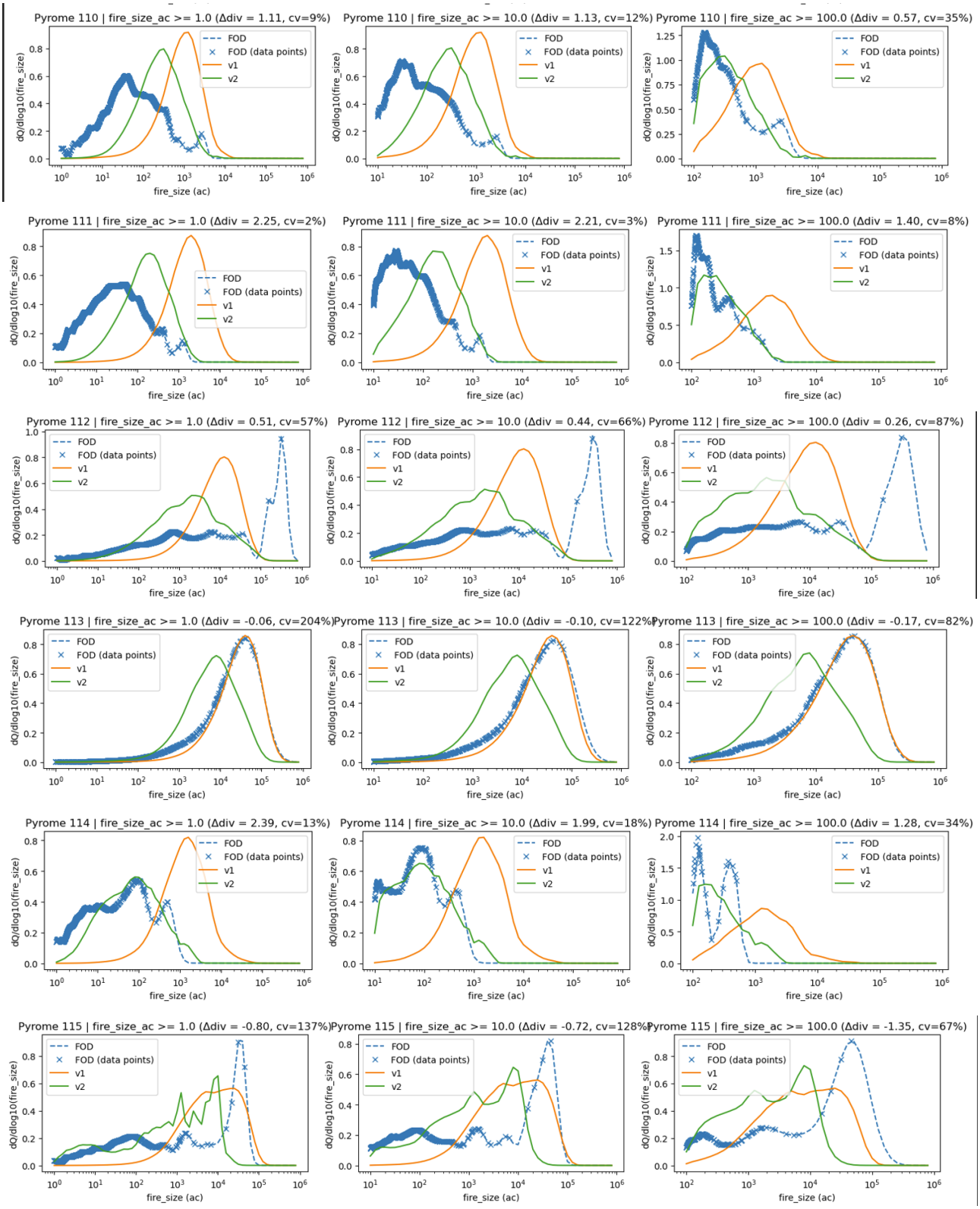
Pyrome 110 | fire_size_ac >= 1.0 (Δdiv = 1.11, cv=9%)
Pyrome 110 | fire_size_ac >= 10.0 (Δdiv = 1.13, cv=12%)
Pyrome 110 | fire_size_ac >= 100.0 (Δdiv = 0.57, cv=35%)
Pyrome 111 | fire_size_ac >= 1.0 (Δdiv = 2.25, cv=2%)
Pyrome 111 | fire_size_ac >= 10.0 (Δdiv = 2.21, cv=3%)
Pyrome 111 | fire_size_ac >= 100.0 (Δdiv = 1.40, cv=8%)
Pyrome 112 | fire_size_ac >= 1.0 (Δdiv = 0.51, cv=57%)
Pyrome 112 | fire_size_ac >= 10.0 (Δdiv = 0.44, cv=66%)
Pyrome 112 | fire_size_ac >= 100.0 (Δdiv = 0.26, cv=87%)
Pyrome 113 | fire_size_ac >= 1.0 (Δdiv = -0.06, cv=204%)
Pyrome 113 | fire_size_ac >= 10.0 (Δdiv = -0.10, cv=122%)
Pyrome 113 | fire_size_ac >= 100.0 (Δdiv = -0.17, cv=82%)
Pyrome 114 | fire_size_ac >= 1.0 (Δdiv = 2.39, cv=13%)
Pyrome 114 | fire_size_ac >= 10.0 (Δdiv = 1.99, cv=18%)
Pyrome 114 | fire_size_ac >= 100.0 (Δdiv = 1.28, cv=34%)
Pyrome 115 | fire_size_ac >= 1.0 (Δdiv = -0.80, cv=137%)
Pyrome 115 | fire_size_ac >= 10.0 (Δdiv = -0.72, cv=128%)
Pyrome 115 | fire_size_ac >= 100.0 (Δdiv = -1.35, cv=67%)
FOD
FOD (data points)
v1
v2
dQ/dlog10(fire_size)
fire_size (ac)

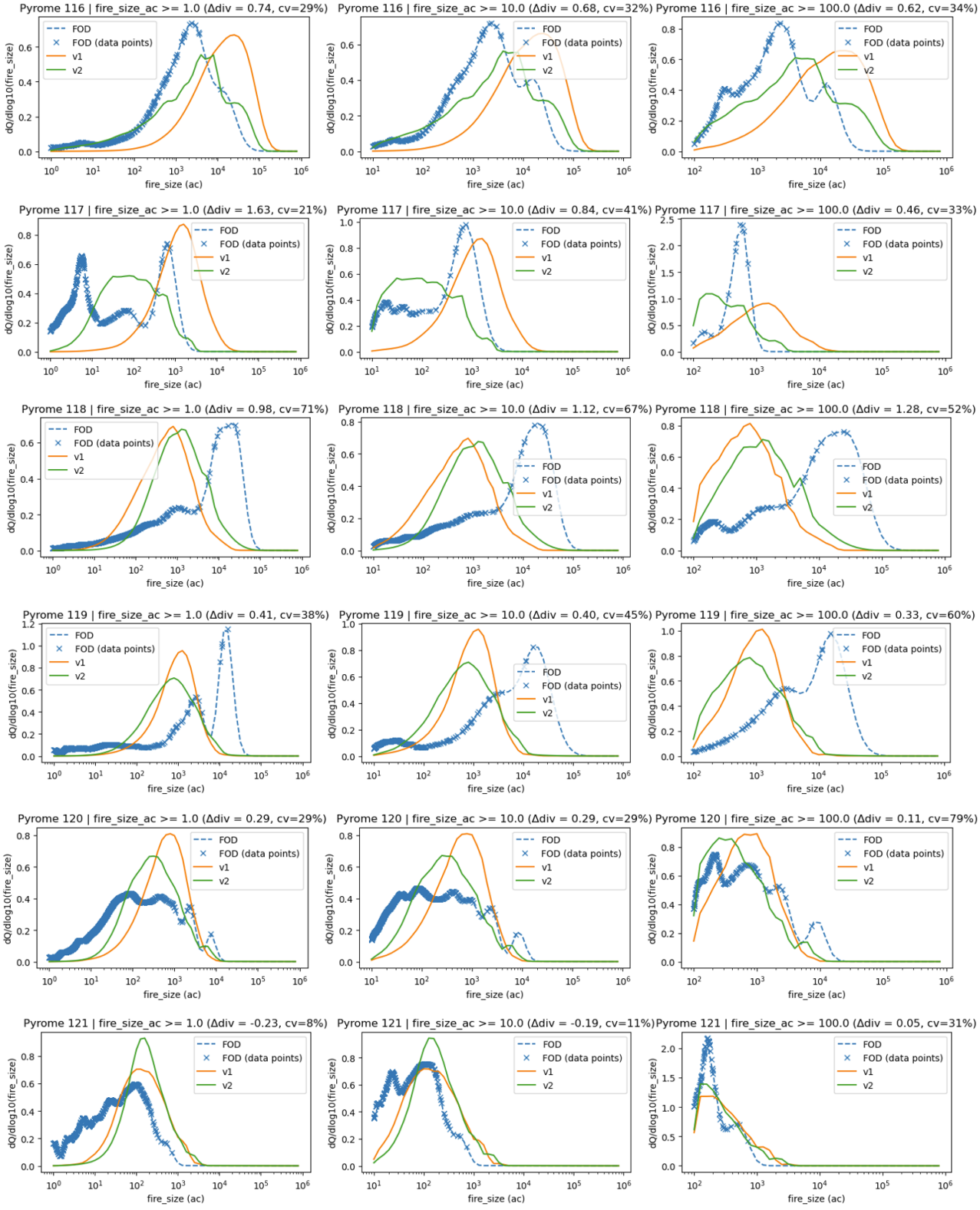
Pyrome 116 | fire_size_ac >= 1.0 (Δdiv = 0.74, cv=29%)
Pyrome 116 | fire_size_ac >= 10.0 (Δdiv = 0.68, cv=32%)
Pyrome 116 | fire_size_ac >= 100.0 (Δdiv = 0.62, cv=34%)
Pyrome 117 | fire_size_ac >= 1.0 (Δdiv = 1.63, cv=21%)
Pyrome 117 | fire_size_ac >= 10.0 (Δdiv = 0.84, cv=41%)
Pyrome 117 | fire_size_ac >= 100.0 (Δdiv = 0.46, cv=33%)
Pyrome 118 | fire_size_ac >= 1.0 (Δdiv = 0.98, cv=71%)
Pyrome 118 | fire_size_ac >= 10.0 (Δdiv = 1.12, cv=67%)
Pyrome 118 | fire_size_ac >= 100.0 (Δdiv = 1.28, cv=52%)
Pyrome 119 | fire_size_ac >= 1.0 (Δdiv = 0.41, cv=38%)
Pyrome 119 | fire_size_ac >= 10.0 (Δdiv = 0.40, cv=45%)
Pyrome 119 | fire_size_ac >= 100.0 (Δdiv = 0.33, cv=60%)
Pyrome 120 | fire_size_ac >= 1.0 (Δdiv = 0.29, cv=29%)
Pyrome 120 | fire_size_ac >= 10.0 (Δdiv = 0.29, cv=29%)
Pyrome 120 | fire_size_ac >= 100.0 (Δdiv = 0.11, cv=79%)
Pyrome 121 | fire_size_ac >= 1.0 (Δdiv = -0.23, cv=8%)
Pyrome 121 | fire_size_ac >= 10.0 (Δdiv = -0.19, cv=11%)
Pyrome 121 | fire_size_ac >= 100.0 (Δdiv = 0.05, cv=31%)
FOD
FOD (data points)
v1
v2
dQ/dlog10(fire_size)
fire_size (ac)

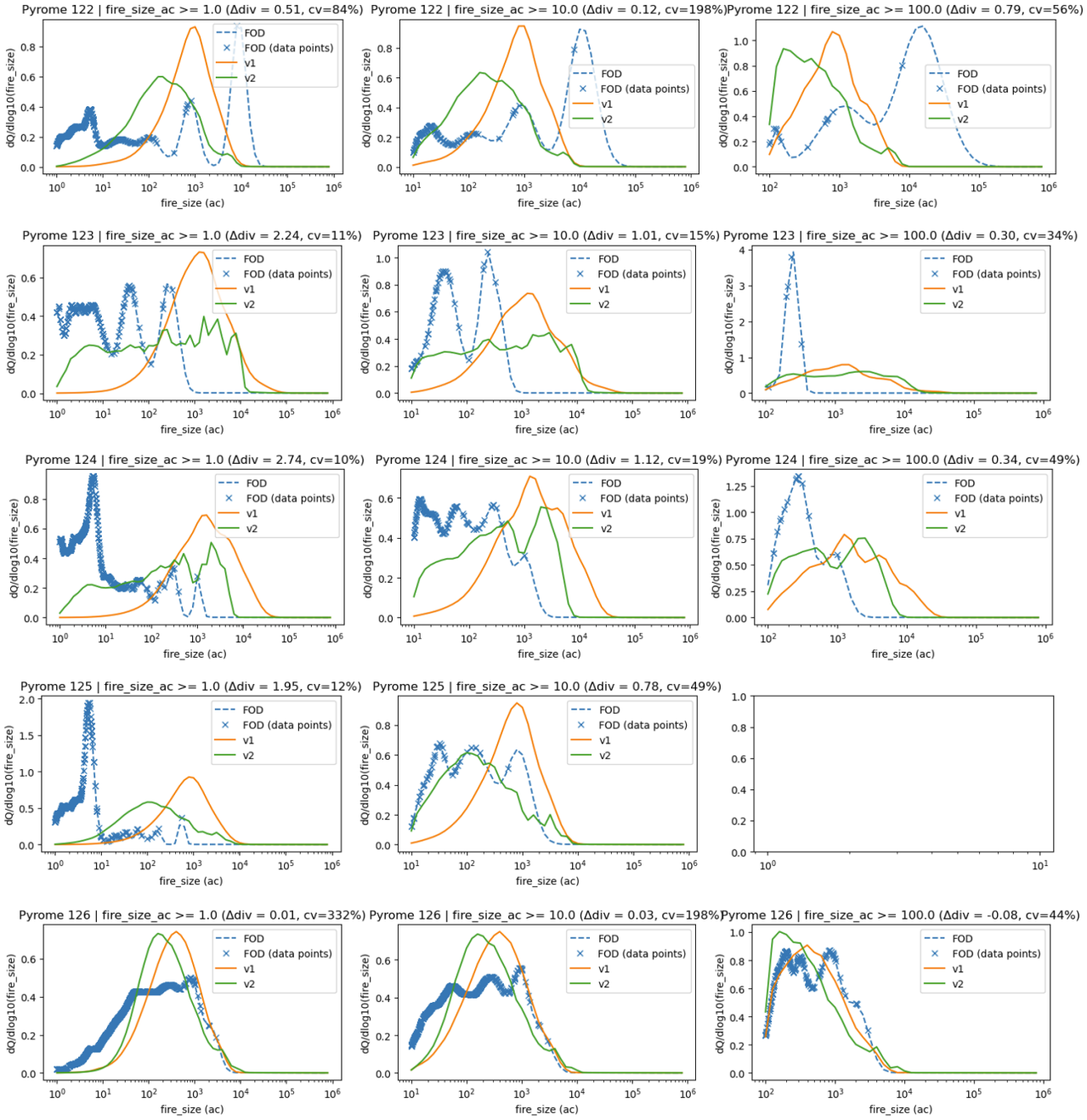
Pyrome 122 | fire_size_ac >= 1.0 (Δdiv = 0.51, cv=84%)
Pyrome 122 | fire_size_ac >= 10.0 (Δdiv = 0.12, cv=198%)
Pyrome 122 | fire_size_ac >= 100.0 (Δdiv = 0.79, cv=56%)
Pyrome 123 | fire_size_ac >= 1.0 (Δdiv = 2.24, cv=11%)
Pyrome 123 | fire_size_ac >= 10.0 (Δdiv = 1.01, cv=15%)
Pyrome 123 | fire_size_ac >= 100.0 (Δdiv = 0.30, cv=34%)
Pyrome 124 | fire_size_ac >= 1.0 (Δdiv = 2.74, cv=10%)
Pyrome 124 | fire_size_ac >= 10.0 (Δdiv = 1.12, cv=19%)
Pyrome 124 | fire_size_ac >= 100.0 (Δdiv = 0.34, cv=49%)
Pyrome 125 | fire_size_ac >= 1.0 (Δdiv = 1.95, cv=12%)
Pyrome 125 | fire_size_ac >= 10.0 (Δdiv = 0.78, cv=49%)
Pyrome 126 | fire_size_ac >= 1.0 (Δdiv = 0.01, cv=332%)
Pyrome 126 | fire_size_ac >= 10.0 (Δdiv = 0.03, cv=198%)
Pyrome 126 | fire_size_ac >= 100.0 (Δdiv = -0.08, cv=44%)
FOD
FOD (data points)
v1
v2
dQ/dlog10(fire_size)
fire_size (ac)

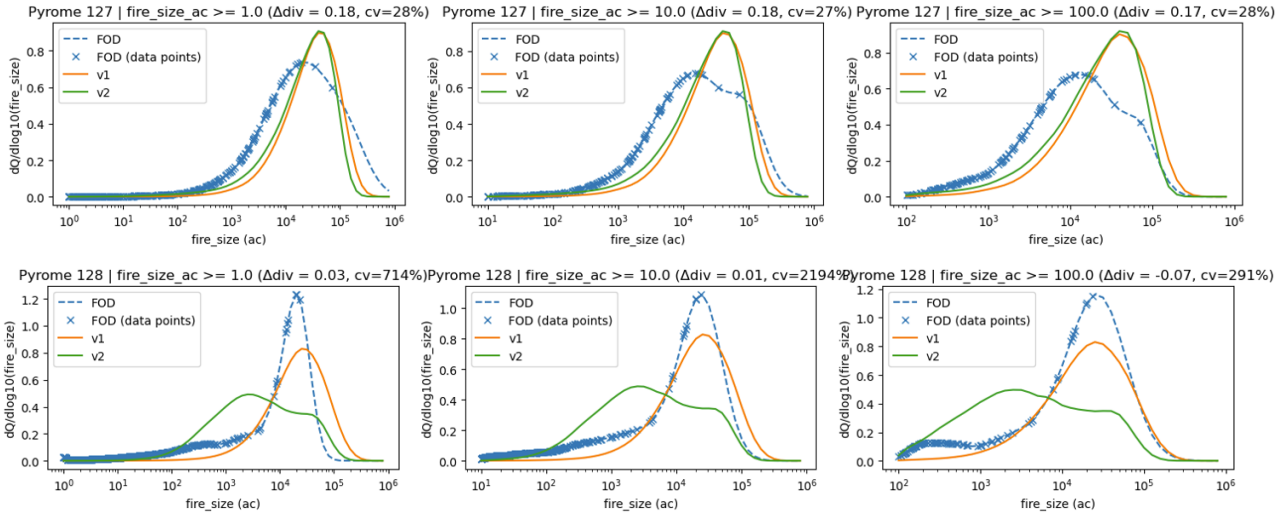

Figure B2: Calibration/validation results for each CONUS pyrome, numbers 1 (top) to 128 (bottom). Results for FSF-WFM V1 (orange) and V2 (green), and their comparisons against FOD records (blue) are presented. Results for all fire sizes (left), fires greater than 10 acres (middle) and fires greater than 100 acres (right) are presented for each pyrome. If a figure is missing it indicates a lack of simulated fires in that pyrome or class.

Figure B3: Pyrome locations as defined by the US Forest Service (Short et al, 2020).